Computational Investigations of Organometallic Catalysis

Thesis by
James J. Lawniczak

In Partial Fulfillment of the Requirements for the
Degree of
Doctor of Philosophy

CALIFORNIA INSTITUTE OF TECHNOLOGY
Pasadena, California

2023
Defended July 8, 2022

James J. Lawniczak
ORCID: 0000-0003-1898-9809

ACKNOWLEDGEMENTS

I would like to begin by thanking my advisor, Professor Tom Miller, for his guidance and encouragement as I entered the field of computational chemistry. He offered unwavering support for interdisciplinary collaborations between computational and experimental chemistry. I deeply appreciate my time in his group.

I also want to thank my former advisor, Professor Gregory Fu, for his support and patience during my time in his group as well as our subsequent research collaboration. I have deep gratitude for the experience at the lab bench. I am grateful for his continued support of my research as I transitioned to the Miller group.

I would like to express my gratitude to my current and former committee members: Professors William Goddard, Gregory Fu, Maxwell Robb, and Bob Grubbs (may he rest in peace) for their guidance and feedback throughout the PhD journey.

I want to thank all the members of the Miller group for their support throughout my time in the group: Priscilla, Xinglong, Feizhi, Leanne, Saleh, Jeongmin, Xuecheng, Emiliano, Ioan, Jorge, Sherry, Dan, Matthew, Sebastian, Philip, Varun, Vignesh, Tomislav, Steve, Tamara, Zhouran, Marta, Roman, Doris, Jiace, Rui, and Bo.

I also would like to express my gratitude for members of the Fu group for their support in my time in the group: Robert, Suzanne, Wendy, Socrates, Bobbi, Haohua, Zhaobin, Zepeng, Caiyou, Yusuke, Arianna, Bradley, Gregg, Joe, Stefan, Jaika, Haolin, Hidehiro, Carson, Zhichao, and Kevin.

I would like to thank our collaborators at Dow for our joint research: Sukrit Mukhopadhyay, Peter Margl, and Jerzy Klosin.

I have deep gratitude for my family and friends for their support. I want to thank Callie and Mo for their close support throughout my PhD. My success is due in part to their unwavering support.

I also would like to express my gratitude to my former advisors from my undergraduate research and the members of their groups: Professors Melanie Sanford, Daniel Nocera, and Brent Martin. My formative experiences in their groups have prepared me well for graduate research.

I also want to thank Caltech for supporting me throughout my time and for fostering a welcoming environment. In addition, I thank the National Science Foundation for granting the Graduate Research Fellowship which provided financial support to my graduate research.

Science is a community and fundamentally based on collaboration. My professional colleagues and mentors as well as my friends and family have been key in my PhD journey and their support continues to inspire me in my scientific journey.

ABSTRACT

Organometallic catalysis facilitates the synthesis of diverse products ranging from polyolefin materials to pharmaceutical compounds, and catalyst performance depends in part on the design of the ligand scaffold. Towards computational ligand design, quantum mechanical methods more fully capture chemical reactivity in comparison to classical methods, but are more computationally demanding. Free energy calculations of key elementary steps of the catalytic cycle permit the computational prediction of catalyst performance and allow modifications of the ligand structure to be explored. In the dissertation, experimental and computational investigations of organometallic catalysis focuses on rational ligand design. Embedding techniques such as embedded mean field theory (EMFT) and quantum mechanics/molecular mechanics (QM/MM) are leveraged in free energy calculations to allow for the reduction of wall-clock times of energy calculations and trajectory sampling. The organometallic systems investigated include Group IV polyolefin catalysts capable of co-polymerization and enantioselective cross-coupling nickel catalysts. Additionally, experimental methodology development is discussed for a nickel-catalyzed cross-coupling of alkynyl nucleophiles to tertiary electrophiles.

PUBLISHED CONTENT AND CONTRIBUTIONS

(1) Lawniczak, J. J.; Zhang, X.; Christianson, M.; Bailey, B.; Bremer, S.; Barcia, S.; Mukhopadhyay, S.; Klosin, J.; Miller, T. F. *J. Phys. Chem. A* **2022**,
The author participated in designing the research, conducting simulations, discussing the results, and preparing a draft. Manuscript under review (DOI not available).

(2) Shoshani, M.; Xiong, S.; Lawniczak, J. J.; Zhang, X.; Miller, T. F.; Agapie, T. *Organometallics* **2022**,
https://doi.org/10.1021/acs.organomet.2c00241.
The author participated in conducting computations, discussing the results, and preparing a portion of the draft.

(3) Chen, L. D.; Lawniczak, J. J.; Ding, F.; Bygrave, P. J.; Riahi, S.; Manby, F. R.; Mukhopadhyay, S.; Miller, T. F. *J. Chem. Theory Comput.* **2020**, *16*, 4226–4237,
https://doi.org/10.1021/acs.jctc.0c00169.
The author participated in designing the research, conducting simulations, discussing the results, and preparing a draft.

TABLE OF CONTENTS

LIST OF ILLUSTRATIONS

LIST OF TABLES

Number *Page*

NOMENCLATURE

Density functional theory (DFT). A quantum mechanical computational method which employs the electron density in the energy functional.

Embedded mean field theory (EMFT). A framework for quantum embedding in which two different mean-field (e.g., DFT) methodologies are employed. Notably, the computationally costly mean field method is applied to only a subset of the molecular system.

Enantioselective reaction. A chemical reaction that preferentially produces one enantiomer of the chiral product.

Quantum mechanics / molecular mechanics (QM/MM). A methodology for molecular dynamics in which a small subset of the molecular system is treated with quantum mechanics (QM), whereas the remaining atoms (e.g., solvent) is treated classically with molecular mechanics (MM).

Chapter 1

INTRODUCTION

Organometallic catalysis is key to the synthesis of products ranging from pharmaceuticals to polyolefin materials, which motivates the design of higher-performing catalyst systems that, among other goals, are longer lasting and consume less reactant. Two avenues are often pursued for catalyst optimization: experimental and computational studies. Experimental studies include methodology investigations which optimize reaction conditions, along with synthetic efforts to isolate key catalytic species for mechanistic insights. Benchmarked by experimental results, computational techniques such as quantum mechanical calculations of molecular properties offer the advantage of reducing time-consuming experimental screens and expensive syntheses. In particular, the computational prediction of the free energy landscape of organometallic catalysis offers mechanistic insights and informs rational catalyst design.

Computational techniques that interrogate organometallic catalysis require the development of accurate models for catalysis that also balance efficiency of the underlying calculation. For example, one problem that emerges in the study of enantioselective cross-coupling and co-polymerization is the presence of nearly isoenergetic pathways (on the kcal/mol scale) that need to be resolved by free energy calculations. In addition, the sampling of molecular dynamics trajectories necessary for computing anharmonic free energies are limited by the wall-clock time of a trajectory run. The large size of ligand scaffolds and the presence of a metal center necessitates faster quantum mechanical techniques. Developing computational techniques that resolve small free energy differences and that minimize wall-clock time are essential for computational investigations of organometallic systems. A common thread that emerged during the course of research is the employment of embedding approaches such as embedded mean-field theory (EMFT) and quantum mechanics/molecular mechanics (QM/MM). The former accelerates the calculation of quantum mechanical properties, while the latter is an efficient framework to simulate solution-phase trajectories. These computational techniques are applied to explore mechanistic questions related to organometallic catalysis.

Chapter 2 presents the experimental discovery and optimization of the enantioselective alkynylation of racemic tertiary electrophiles. The stereoselective construction of quaternary centers is challenging due to steric crowding of the quaternary center, but offers expanded synthetic access to chiral structures relevant to pharmaceutical synthesis. To minimize steric hindrance near the quaternary center, an alkynyl nucleophile is chosen, and the other cross-coupling partner is a tertiary electrophile. The best performing electrophile substrate is α-bromo-α-methyl-γ-butyrolactone, which was chosen as the model substrate for further reaction optimization. Reaction conditions such as ligand, solvent, nucleophile, nickel pre-catalyst, temperature, and reaction time were screened for optimal yield and enantioselectivity. The ligand *(R)*-P-Phos offered the highest enantioselectivity for the model substrate.

Chapter 3 presents the application of embedded mean field theory (EMFT), a form of quantum embedding, to Group IV polyolefin catalyst systems. Quantum embedding techniques such as EMFT accelerates QM calculations, but require benchmarking with experimental systems. In this project, EMFT predictions of monomer binding energies to selected polyolefin catalysts are benchmarked with B3LYP calculations. Binding energies of ethylene and propylene to the catalyst systems are within 1 kcal/mol of the high-level B3LYP result, while the wall-clock time of an SCF cycle is reduced up to 20-fold. EMFT is then applied to accelerate the sampling of the solution-phase catalyst-counterion pair in order to elucidate binding dynamics of strongly and weakly coordinating counterions. Our results indicate that the binding of ethylene to the catalyst is affected by the interaction between the metal complex and the counterion. The dissociation of ethylene from the catalyst is induced by proximity of the counterion to the metal complex.

Chapter 4 presents the application of quantum mechanics/molecular mechanics (QM/MM) to study the effect of conformational sampling and explicit solvation on the free energy differences of incorporation (monomer binding and insertion) of α-olefin co-monomers polymerized with ethene. The prediction of co-monomer incorporation ratios is necessary to control polyolefin physical properties, but requires sub-kcal/mol resolution of free energies among catalyst systems. Typically, static DFT single-point calculations are employed to compute free energies, but neglect the anharmonic contributions from conformational sampling and explicit solvation effects. These contributions are quantified via restrained MD trajectories along the minimum energy path of the insertion barrier. The converged trajectories are used to quantify insertion barrier free energies for three CGC catalyst systems. Signif-

icant corrections to the free energy (~1-2 kcal/mol) are seen due to anharmonic contributions, which are on the same energy scale needed to resolve free energy differences between catalyst systems. The implication is that sub-kcal/mol resolution of free energies relevant to co-incorporation ratios requires the quantification of anharmonic contributions to the solution-phase insertion barrier.

Chapter 5 presents the experimental and computational investigations of nickel phosphine phenoxide complexes employed in the co-polymerization of ethylene and acrylate monomers. Neutral nickel catalysts with bulky ligands stand out for polymerization due to their high activity and thermal stability, but mechanistic insight into the monomer coordination step is lacking. The isolation of auxiliary-donor free systems **1-CCO** and **2-CCO** opens up the possibility for exploring the thermodynamics of monomer coordination and chelate opening. To augment the experimental results, computed free energies for the monomer coordination elementary step is explored for polar monomers (e.g., *t*-butyl acrylate, acrylonitrile), which are benchmarked with the available experimental data. Binding trends among catalysts are rationalized by quantifying electrophilicity of the metal center. Mechanistic understanding of monomer coordination to the neutral nickel catalysts informs the design of novel catalysts.

Chapter 2

METHODOLOGICAL DEVELOPMENT OF NICKEL-CATALYZED ENANTIOSELECTIVE CROSS-COUPLING OF TERTIARY ALKYL ELECTROPHILES

ABSTRACT

The synthesis of enantioenriched quaternary stereocenters is a challenging problem, and stereoconvergent cross-couplings show promise in accessing enantioenriched all-carbon quaternary centers. Alkynes offer a useful handle for functionalization, yet enantioselective alkynylation reactions are underdeveloped. Herein, the discovery and optimization of the enantioselective alkynylation of racemic tertiary electrophiles are reported. The model substrate was α-bromo-α-methyl-γ-butyrolactone, which afforded high enantioenriched product using the bidentate phosphine ligand *(R)*-P-Phos. Screening of nickel precatalyst, ligand, nucleophile, solvent, temperature, and reaction time provided the best enantioselective result of 29% yield and 90% ee with the ligand *(R)*-P-Phos. Methodological development and discussion of reactivity and scope are discussed within.

Introduction

Quaternary Stereocenter Construction

Pharmaceutical synthesis has revolutionized human lifespan and quality of life in part by the availability of a diverse range of methodologies for lead discovery. Chiral organic molecules possess a large chemical space for drug discovery and optimization, and a larger surface area for tunable substrate-biomolecule interaction [1]. The inclusion of chiral centers promotes binding selectivity and mitigates undesirable π-stacking in drug candidates [2]. Given the favorable effects of chiral centers, there is ongoing interest in developing enantioselective cross-coupling reactions [3].

Quaternary centers, which contain four unique carbon substituents bound to a central carbon atom, are challenging targets for enantioselective cross-coupling [4], and immediately relevant for pharmaceutical synthesis. Of the top 200 pharmaceuticals by retail sales in 2013, 21 compounds contain quaternary centers (Figure 2.1) [5]. These centers are derived from terpenoid and morphine natural products, and have not been synthesized by enantioselective catalysis. Methodologies for facile construction of diverse quaternary stereocenters are necessary to fully leverage the three-dimensional geometry of organic molecules.

Classical methods for synthesizing quaternary centers are effective for generating multiple stereocenters simultaneously. The aldol addition reaction and Claisen rearrangement are capable of generating one and two stereocenters, respectively [6, 7], while the Diels-Alder reaction can access up to four quaternary centers simultaneously (Figure 2.2) [8]. However, the product scope of these reactions is not general. Although the Diels-Alder reaction can be used to generate a single quaternary center, the stereocenter is positioned in either the allylic or homoallylic position and is bound to a six-membered ring.

Cross-coupling offers a complementary, modular approach to quaternary center synthesis. Towards this effort, the Oshima group published early examples of employing tertiary electrophiles as cross-coupling partners. Under copper, silver, or cobalt catalysis, the nucleophile scope was limited to allylic [9–12], benzyl [10, 11], and cyclopentadienyl Grignard reagents [13] as well as allylic and benzylic Negishi reagents [14]. Moreover, none of the generated quaternary stereocenters were enantioenriched.

To achieve the enantioselective synthesis of quaternary centers, research in the Fu group leverages transition metal-catalyzed cross-coupling. The racemic, nickel-catalyzed borylation [15] and arylation [16] of tertiary alkyl electrophiles generated

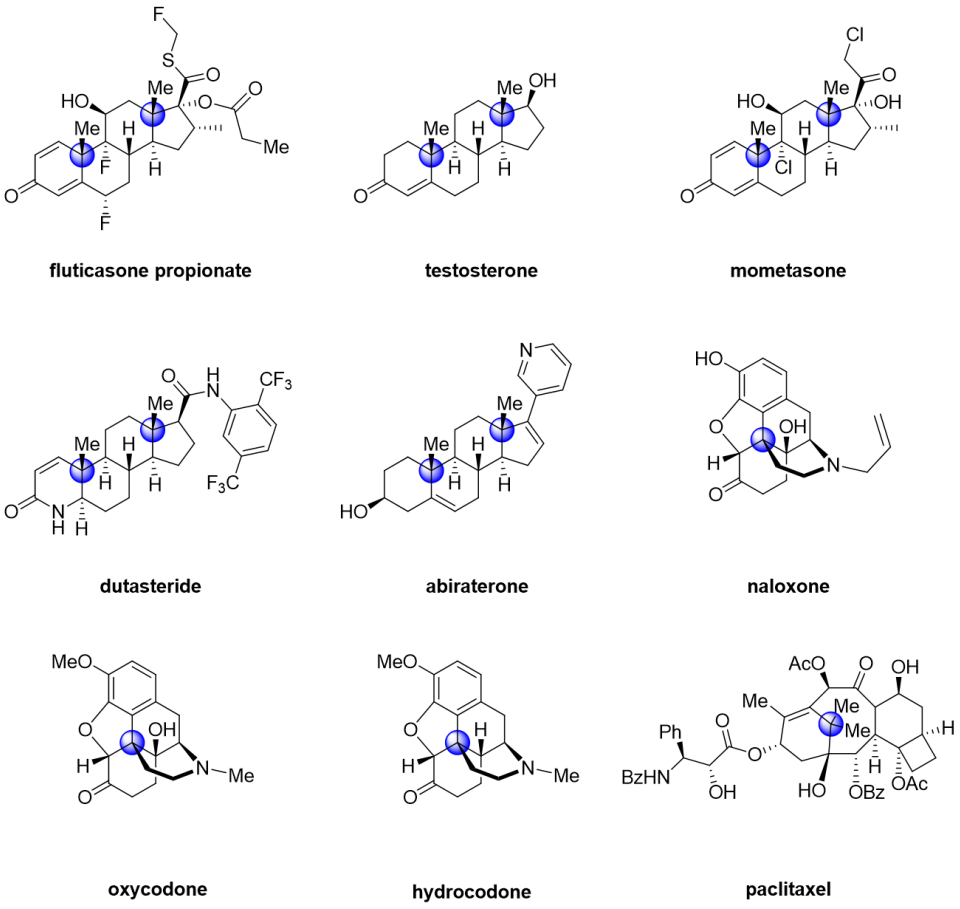

Figure 2.1: Selected pharmaceuticals with quaternary centers (highlighted in blue).

tetrasubstituted and quaternary centers, respectively (Figure 2.3 a,b), and were the first reported examples of employing tertiary electrophiles for nickel-catalyzed cross-coupling.

The use of chiral ligands with either nickel or copper catalyst were able to generate enantioenriched stereocenters. Further methods achieved enantioenriched tetrasubstituted centers via the arylation of α-bromo-α-fluoroketones [17] and the amination of α-bromoketones [18] (Figure 2.3 c,d). In addition, the coupling of tertiary halides with alkenes successfully constructed enantioenriched quaternary stereocenters (Figure 2.3e) [19].

Other groups have also worked towards the construction of quaternary centers through non-asymmetric and asymmetric pathways. The Stoltz group has reported successes in the alkylation of 3-halooxindoles [20], the conjugate addition of arylboronic acids to cyclic enones [21], and the allylic alkylation of cyclic ketoesters

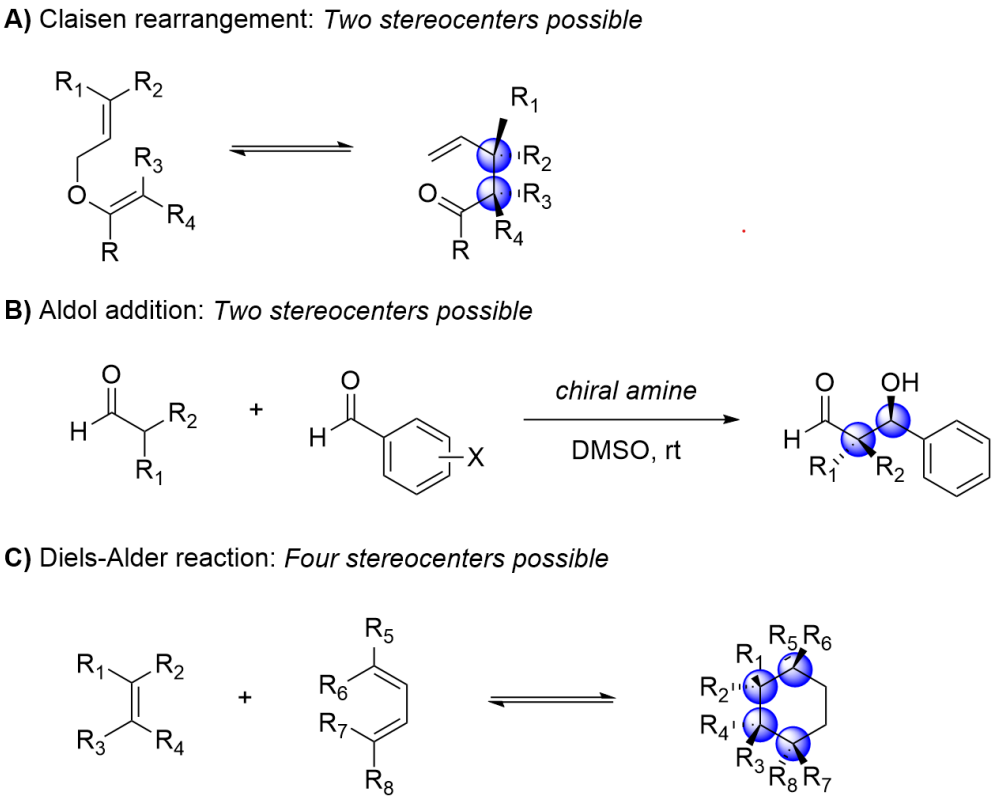

Figure 2.2: Selected classical methods for quaternary center construction.

[22], which generated asymmetric quaternary centers. Other examples include the non-asymmetric nickel-catalyzed reductive arylation of alkyl electrophiles (Figure 2.4a) [23] and the stereoretentive coupling of enantiopure tertiary electrophiles with arylboronic acids (Figure 2.4b) [24]. In addition, the ring opening of aziridines by alkyl Negishi cross-couplings afforded quaternary centers, although only one stereoselective product is reported, with 27% ee (enantiomeric excess) (Figure 2.4c) [25].

Alkynylation Functionalization

Alkynes are a useful functional group due to its versatility for divergent functionalization and applicability to materials and medicine. For example, alkanes and alkenes can be accessed by single- or double-hydrogenation of the alkyne, respectively, and selective catalysts exist to generate the Z-alkene [26] or the E-alkene (Figure 2.5) [27]. Other alkyne derivitiations include hydroformylation [28], hydrofluorination [29], hydrocyanation [30], and hydroamination [31], while alkyne metathesis [32] can exchange the terminal alkyne substitutent. Cycloaddition to

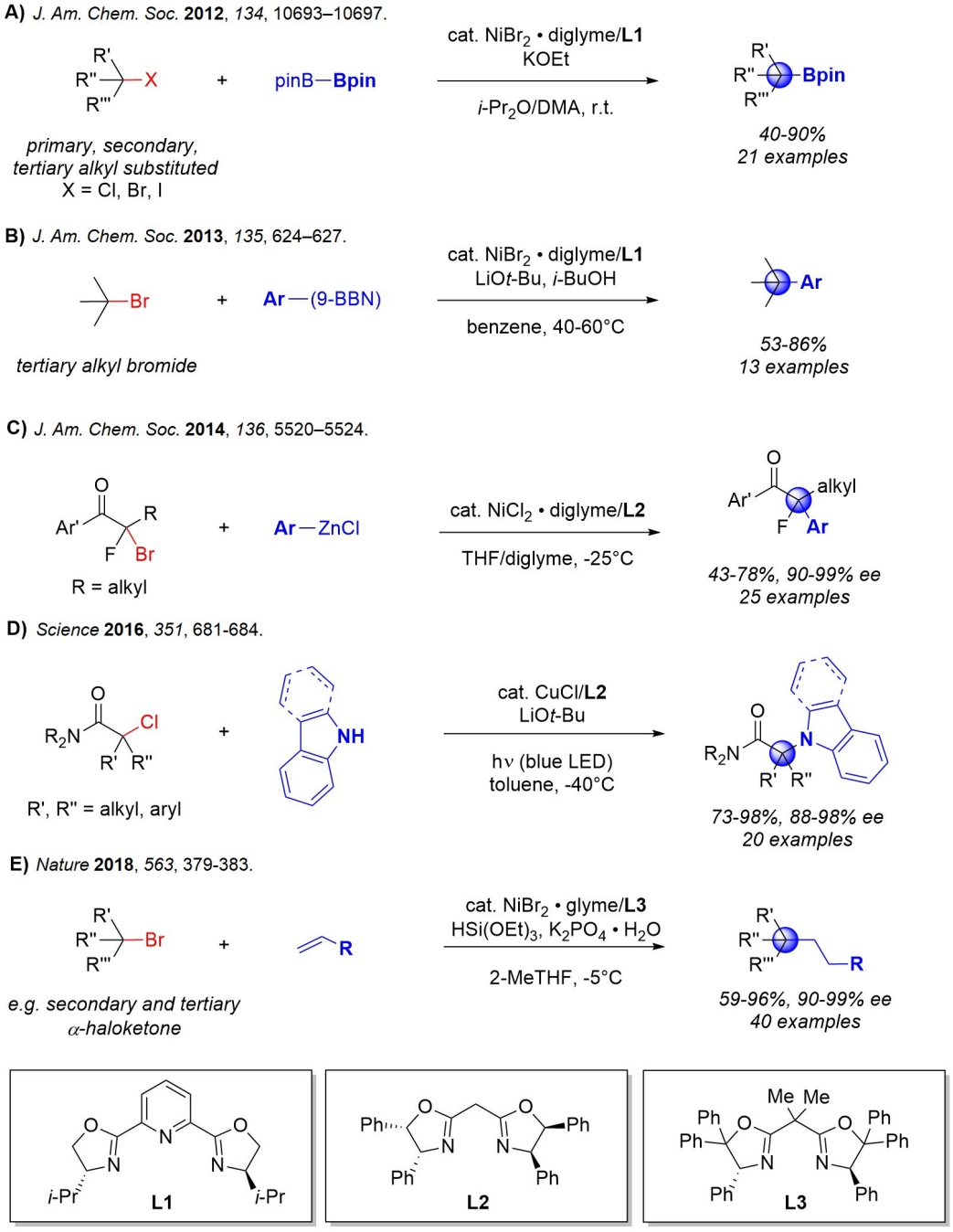

Figure 2.3: Fu group methodologies towards enantioenriched quaternary stereocenters.

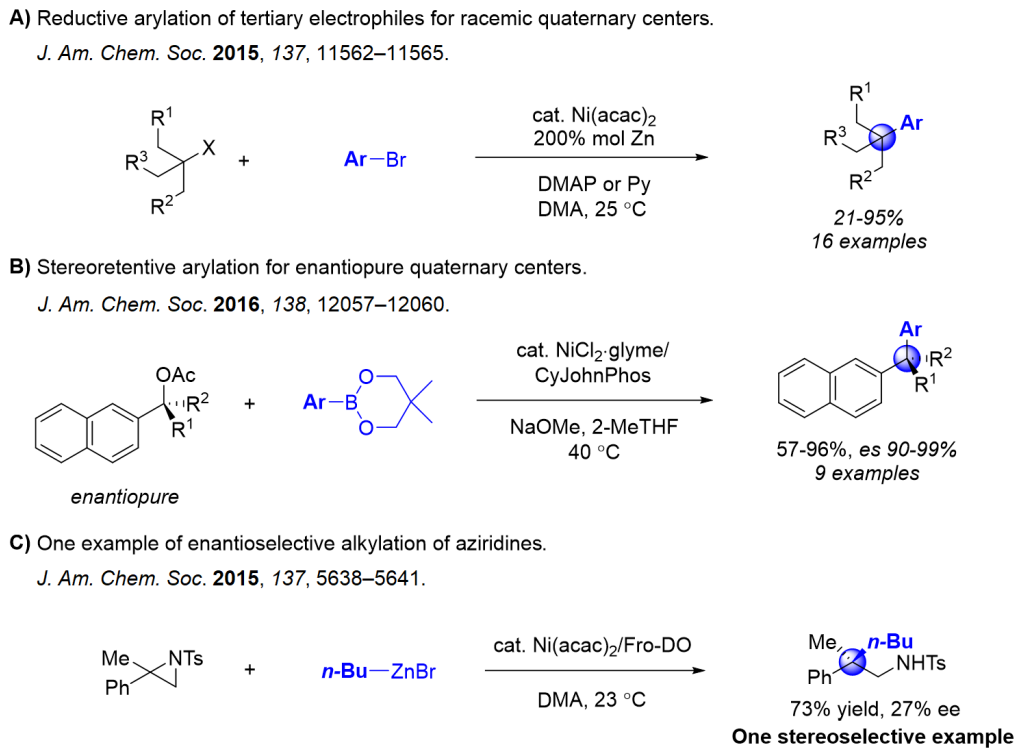

Figure 2.4: Racemic, stereoretentive, and stereoselective quaternary center constructions.

alkynes is well-precedented [33, 34], and a noteworthy example is the alkyne-azide "click" reaction [35], employed in bioconjugation, polymer synthesis, and surface functionalization [36].

The installation of alkynyl groups is well-precedented in the literature, with a progression towards enantioselective pathways. The syntheses of racemic secondary and tertiary alkynylated stereocenters use a variety of catalytic systems including nickel [37], copper [38], iron [39], and non-metal Lewis acids (Figure 2.6a) [40]. Diastereoselective alkynylation can be achieved with a palladium catalyst [41]. Most examples of enantioselective alkynylation utilize a nickel catalyst to functionalize secondary alkyl halide electrophiles, with alkynylindium [42] and alkynylaluminum [43] reagents used as the nucleophilic cross-coupling partner (Figure 2.6b). Additionally, a recent example involving copper catalysis achieved enantioselective Sonogashira coupling with allylic halides [44]. However, these enantioselective examples were limited to secondary electrophiles.

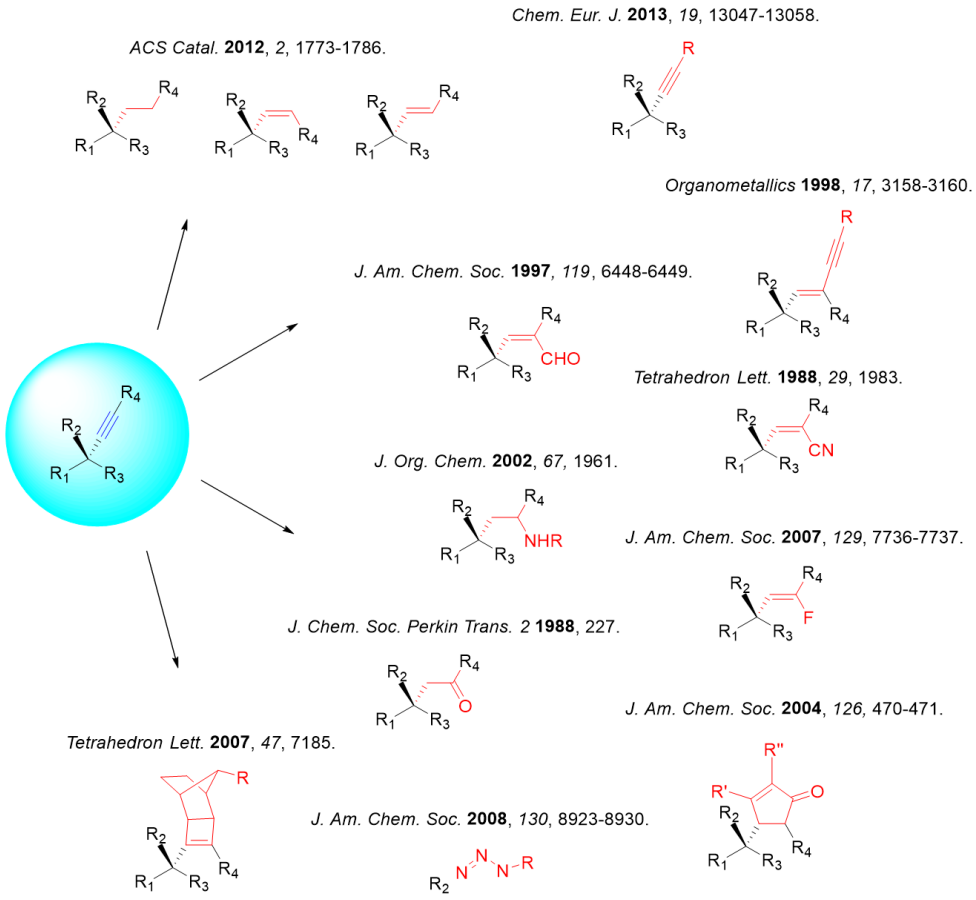

Figure 2.5: Scope of alkyne functionalization.

To achieve the enantioselective alkynylation of racemic tertiary electrophiles, a nickel catalyst is a natural choice given its known reactivity towards tertiary electrophiles and alkynyl nucleophiles. The construction of quaternary centers with an alkynyl group accesses a unique geometry involving a fully-substituted carbon center with an alkynyl group projecting out. The utility of a highly-substituted quaternary center and the functionalized derivatives of the alkyne motivates the development of employing racemic tertiary electrophiles towards enantioselective alkynylation.

Reaction System

This report discusses the development of the nickel-catalyzed alkynylation of racemic tertiary electrophiles to construct enantioenriched quaternary stereocenters. Given the potential of quaternary centers for improved drug candidates and the utility of alkynes in divergent functionalization, the development of this methodology

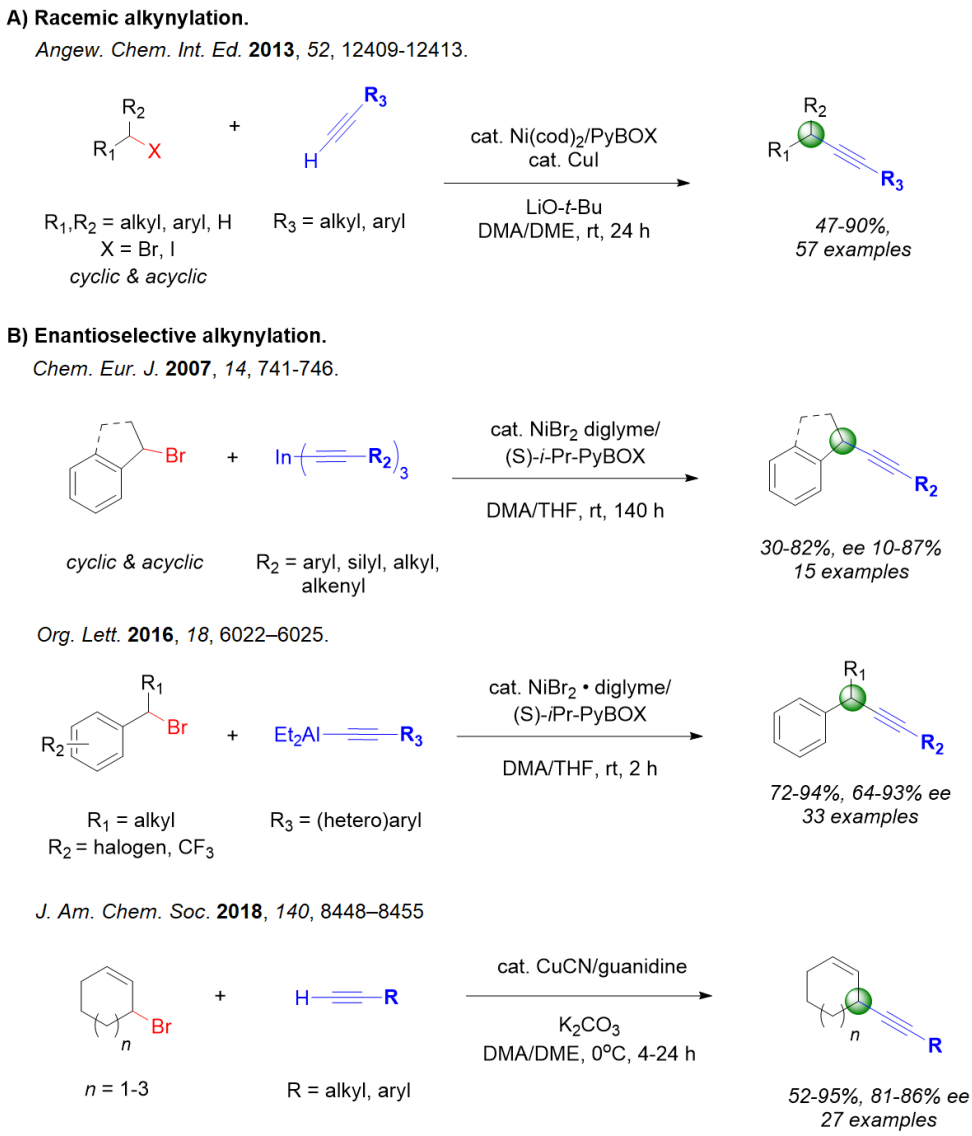

Figure 2.6: Selected racemic and enantioselective alkynylation methodologies.

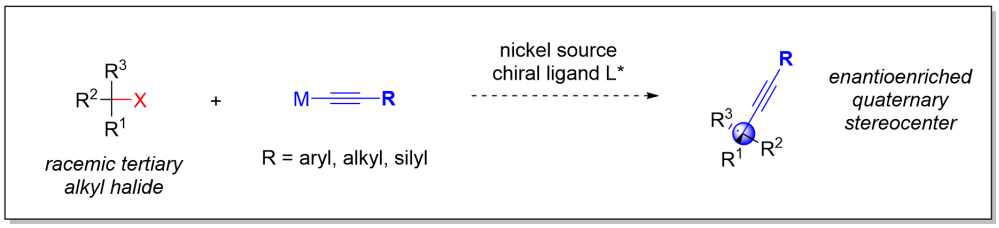

Figure 2.7: Proposed general scheme for enantioselective alkynylation of racemic tertiary alkyl electrophiles.

explores useful new territory in enantioselective cross-coupling. Nickel catalysis has been extensively used in cross-coupling, and the use of chiral ligands has promoted highly enantioselective reactions [45]. The two cross-coupling partners for the proposed system are a racemic tertiary halide and an alkynylmetallic reagent. Substitution of aryl or alkyl groups onto the tetrasubstituted stereocenter in the electrophile is explored, and the substituent and scope of the organometallic alkynyl nucleophile is assessed (Figure 2.7).

Proposed mechanisms of the cross-coupling reaction include a transmetallation-first mechanism and a radical chain mechanism. In the previously described mechanism of the nickel-catalyzed arylation of propargylic halides, the radical chain mechanism was supported [46]. If the radical chain mechanism also holds for alkynylation of tertiary electrophiles, the nickel(I) species is expected to first abstract halide from the electrophile to generate a tertiary radical and nickel(II) dihalide. Then, nickel(II) dihalide would then transmetallate with the alkynyl nucleophile. Capture of the tertiary alkyl radical by the nickel-nucleophile complex would generate a nickel(III) species, which would undergo reductive elimination to afford the desired product (Figure 2.8a). If the transmetallation-first mechanism holds, nickel(I) bromide transmetallates with the nucleophile, followed by halide abstraction to form nickel(II) and tertiary radical. Addition of the tertiary radical to nickel(II) generates a nickel(III) species that undergoes reductive elimination to afford product (Figure 2.8b).

One challenge to the catalysis is controlling the fate of the tertiary electrophile. The steric bulk of the tertiary halide may impede the direct insertion and SN2 oxidative addition of the electrophile, and β-elimination of the alkyl electrophile may occur as well. Moreover, the bulky tertiary radical is relatively stable, due to hyperconjugation of adjacent sigma bonds with the singly-occupied p-orbital

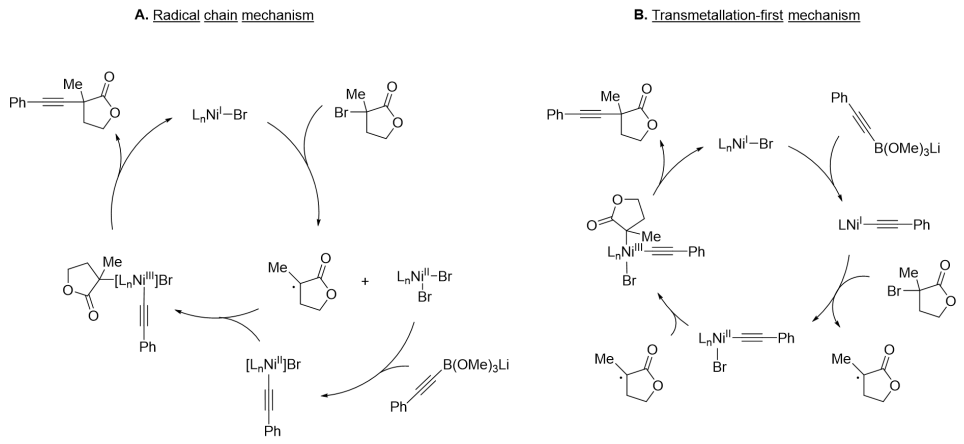

Figure 2.8: The radical chain mechanism and transmetallation-first mechanism for nickel-catalyzed alkynylation of tertiary electrophiles.

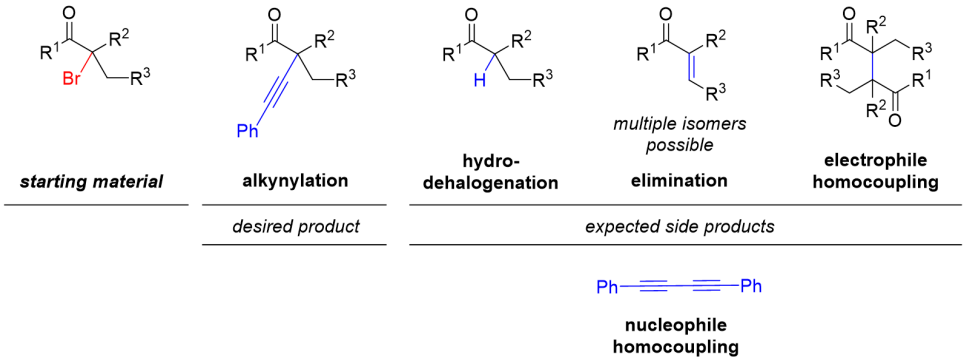

Figure 2.9: Species commonly observed in the reaction mass balance.

on the central carbon. Possible by-products of the reaction include elimination, hydrodehalogenation, electrophile radical homocoupling, and nucleophile oxidative homocoupling (Figure 2.9).

Results and Discussion

To tackle the challenges associated with the enantioselective alkynylation of tertiary electrophiles, initial studies were performed by Dr. Haohua Huo (postdoc fellow in the Fu group) for enantioselective alkynylation of doubly-activated tertiary electrophiles—those possessing two electron-withdrawing groups at the stereogenic carbon. These results were the starting point for developing a methodology employing tertiary electrophiles (Figure 2.10).

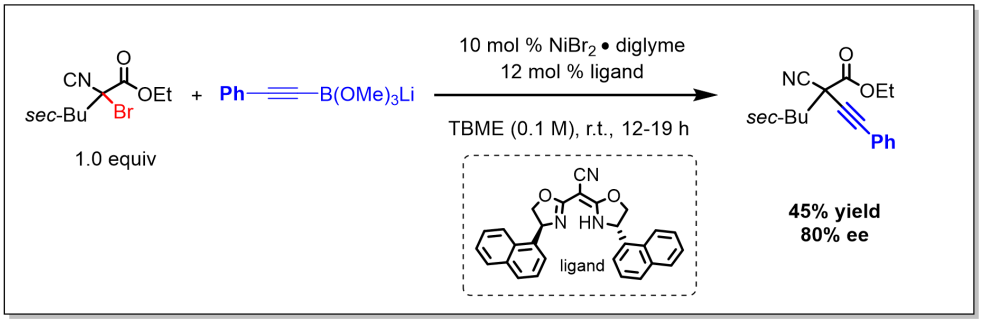

Figure 2.10: Initial results by Dr. Haohua Huo for enantioselective alkynylation of doubly-activated tertiary electrophiles.

Esters appeared to be a promising substrate class for initial screening. Acyclic and cyclic electrophiles were tested with bidentate bis(oxazoline) (BOX) and tridentate pyridine bis(oxazoline) (PyBOX) ligands, which were used in prior nickel-catalyzed cross-coupling (Figure 2.11). Most substrates that were initially tested did not show favorable reactivity; hydrodehalogenation, elimination, electrophile homocoupling, and nucleophile homocoupling were commonly observed. Gratifyingly, the five-membered lactone 11-1 afforded racemic product in modest yields, with the highest yields given by (R,R)-i-Pr-PyBOX, 11-L2. The substituted γ-butyrolactone substrate 11-1 gave a promising result in terms of product formation, and induction of chirality was a focus of further optimization.

Substrate 11-1 was carried over for further optimization, and focus was placed on enantioinduction. Important parameters for reaction optimization included choice of ligand and solvent for the catalysis. The chiral ligand controls the electronic and steric enviornment of the catalyst, which tune catalytic reactivity, and the solvent choice influences solubility, metal-ligand coordination, electron transfer, and radical cage effects. The first priority was optimization of ligand by looking into a broader class of ligands. Then, once a satisfactory ligand was found, the methodology optimization focused on other parameters including solvent choice.

Further variants of PyBOX ligand were explored for enantioinduction by varying the structure of the bis(oxazoline) substituents and the 4-position on the pyridine motif (Figure 2.12). None of the ligands provided enantioenriched product, although full conversions and good yields are observed. (Notably, 11-1 underwent full conversion in subsequent reactions, unless otherwise mentioned.) Ligands with smaller substituents (class A, Figure 5.12) or larger substituents (class B) at the

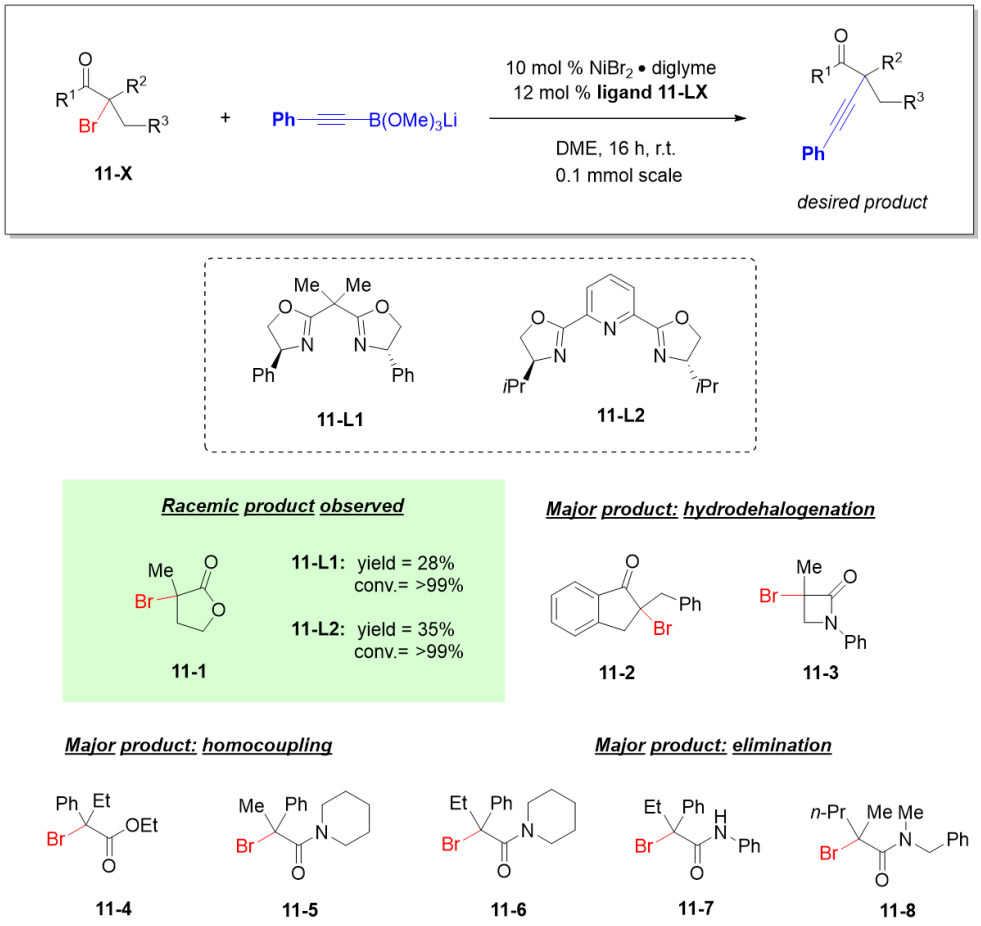

Figure 2.11: Initial screen of ester and amide substrates with BOX and PyBOX ligand.

α-position of the oxazoline fragment gave similar yields. Di-substitution of the oxazoline fragment (class C) also did not have a significant impact on yield. In contrast, the presence of heteroatoms in the oxazoline ring substituents (class D) gave the lowest yields.

Given the lack of enantioinduction with these ligands, a broader scope of bidentate and tridentate ligands was screened (Figure 2.13). Although aminoalcohol 13-L6 gave good yields, the product was racemic; further screenings of aminoalcohols demonstrated no enantioselectivity. However, the bidentate phosphine ligand (R)-BINAP, 13-L3, and the diamine ligand (R,R)-DMPEDA, 13-L4, gave modest enantioinduction of desired product. Other ligands did not generate enantioenriched product, and provided low yields.

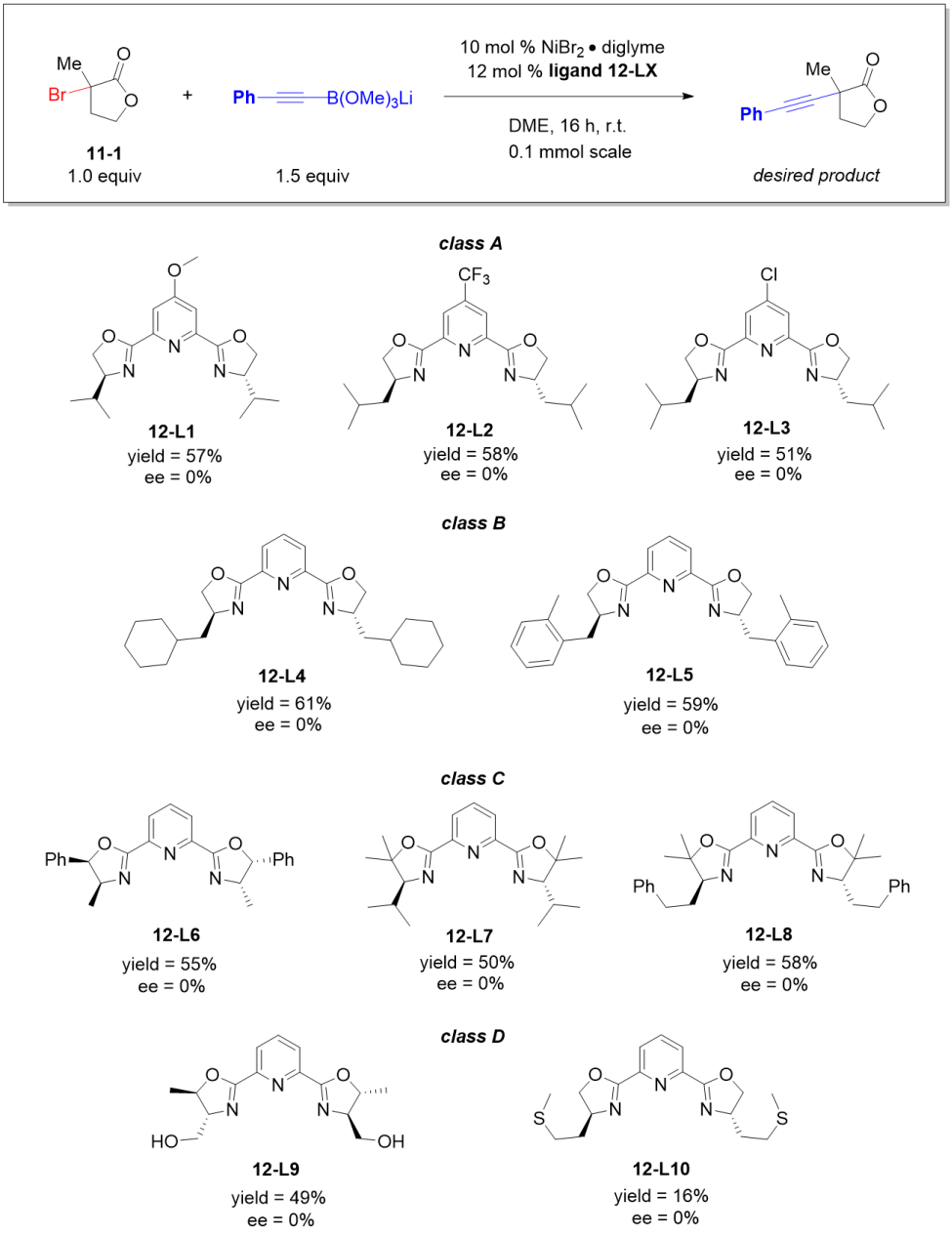

Figure 2.12: Initial screen of ligand classes.

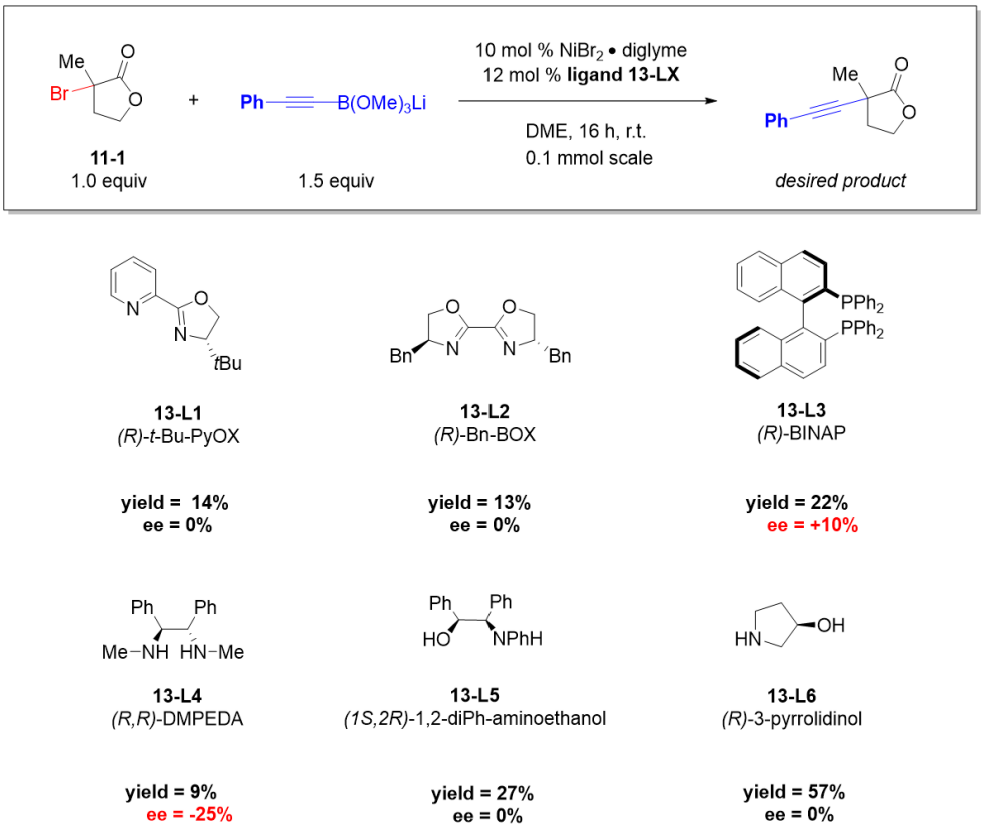

Figure 2.13: Continued broad ligand screen for γ-butyrolactone substrate.

Diamine ligands are a promising ligand class which provided higher enantioselectivities; however, only modest improvements in yield and enantioselectivity has been observed when other diamine ligands were screened (Figure 2.14). The ligand 14-L1 provided the highest enantioselectivity while 14-L8 improved yield but lowered ee. Sterically bulky N-substituents (14-L7, 14-L8, 14-L9, 14-L12, 14-L13, and 14-L14) and bulky arenes on the ligand backbone (14-L11 and 14-L16) gave either no product or racemic product. Although 14-L1 contained bulkier n-propyl N-substituents, higher yields and ee's were observed in comparison to the 1,2-diarylethylenediamine ligand.

Given a lack of progress in diamine ligand screening, another class of promising ligands—bidentate phosphine ligands—were extensively screened for the Ni-catalyzed alkynylation of the model substrate 11-1 (Figure 2.15). In comparison to (R)-BINAP (15-L3), the more substituted ligand (R)-XylBINAP (15-L4) gave higher yields but the same enantioselectivities. This trend does not follow for SEGPHOS ligands,

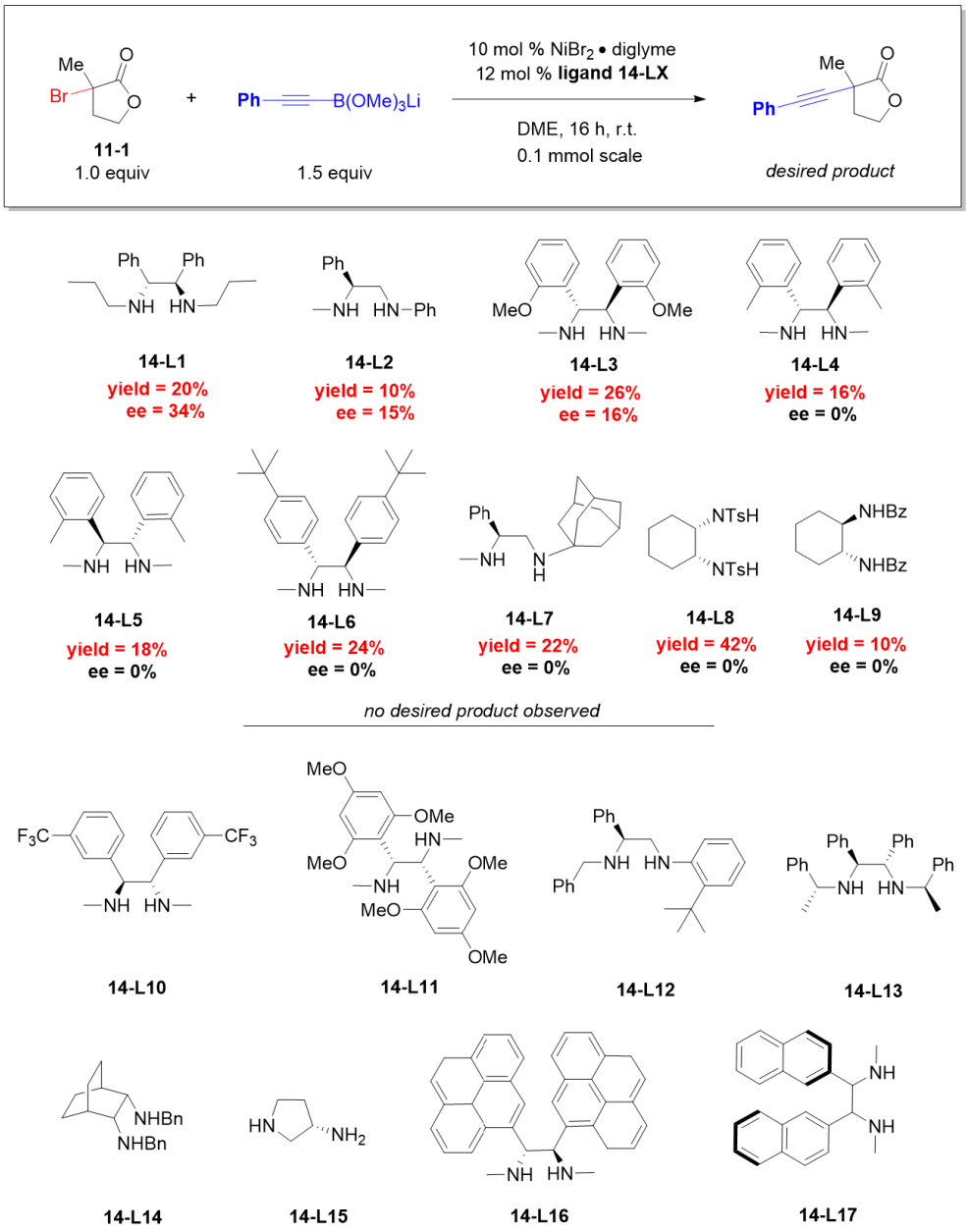

Figure 2.14: Diamine ligands promoting product formation.

however, with the less bulky (R)-SEGPHOS (15-L1) providing better yield and ee. GARPHOS and MeO-BIPHEP ligands did not improve enantioselectivity, although some yields were improved compared to (R)-BINAP (15-L3). Moreover, the monodentate phosphine ligand (R)-MOP (15-L8) gave no desired alkynylation product.

One phosphine ligand stood out, however: *(R)*-P-Phos (15-L7) provided significantly improved yields and enantioselectivities (38% yield and 68% ee). A commercially-available bipyridine bidentate phosphine ligand, *(R)*-P-Phos has unique steric and electronic properties that appear to be favorable for reactivity. Notably, the ligand contains an electron-deficient aromatic backbone. This ligand was a breakthrough in terms of optimizing the enantioselective alkynylation of the γ-butyrolactone model substrate 11-1.

Using conditions specified in Figure 5.15 with ligand *(R)*-P-Phos (15-L7), a solvent screen was performed to improve yields and ee's (Figure 2.16). Three classes of solvents were tested: ethereal solvents; polar, aprotic solvents; and aromatic solvents. Ethereal solvents gave the higher yields, although enantioselectivities remained moderate. Polar, aprotic solvents gave good results approaching 90% ee. Potential reasons for their success include their ability to homogenize the system and to stabilize open coordination sites on the metal center.

After establishing a working model substrate for enantioselective alkynylation, the nucleophilic coupling partner was explored by varying the metallic species undergoing transmetallation with the nickel catalyst (Figure 2.17). Alkynylboron nucleophiles were the most compoenent for enantioselective cross-coupling, providing around 90% ee. Other nucleophiles performed relatively poorly, and all but the alkynylsilicon nucleophiles gave enantioenrichment. The major side-product derived from the electrophile was the hydrodehalogenation side-product 11-1-SP.

Further optimizations and control experiments were performed using *(R)*-P-Phos. Varying the nickel precatalyst, including metal salt additives, increasing reaction time, and adjusting the temperature did not give improved yields or ee's. Additional substrate classes were explored for enantioselective alkynylation, but no desired alkynylated product was obtained (Figure 2.19). Amides, esters, nitriles, and fluorinated substrates gave either hydrodehalogenation, electrophile homocoupling, or the elimination under a broad ligand screen. Interestingly, slightly improved yields and ee's were observed with the ligand (R)-P-XylPhos (Figure 2.18). As an important control for the methodology, the ligand was determined to be necessary for

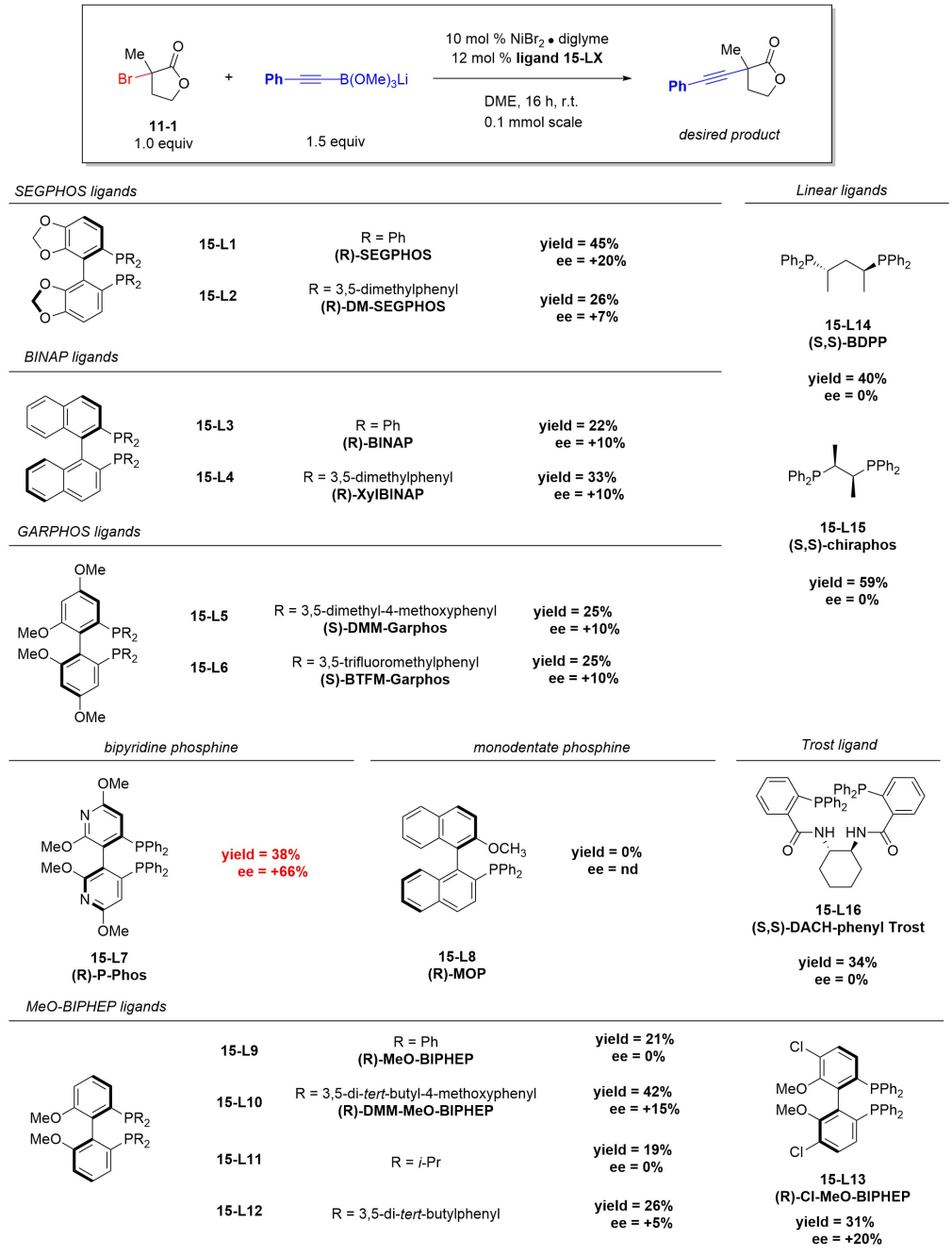

Figure 2.15: Phosphine ligands tested for alkynylation.

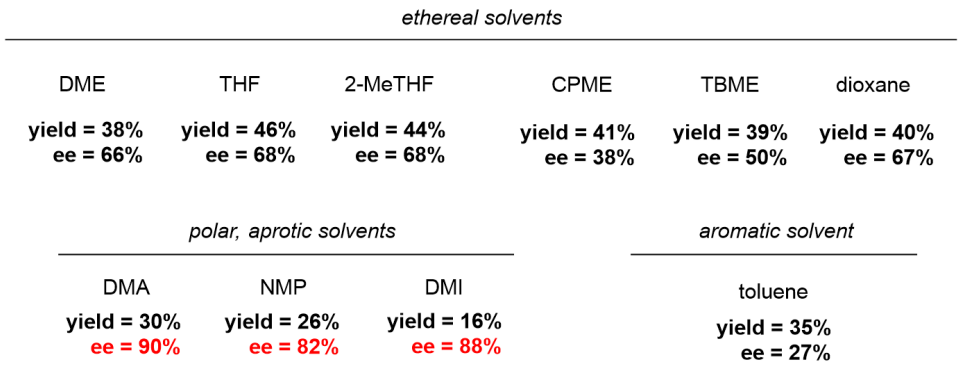

Figure 2.16: Phosphine ligands tested for alkynylation.

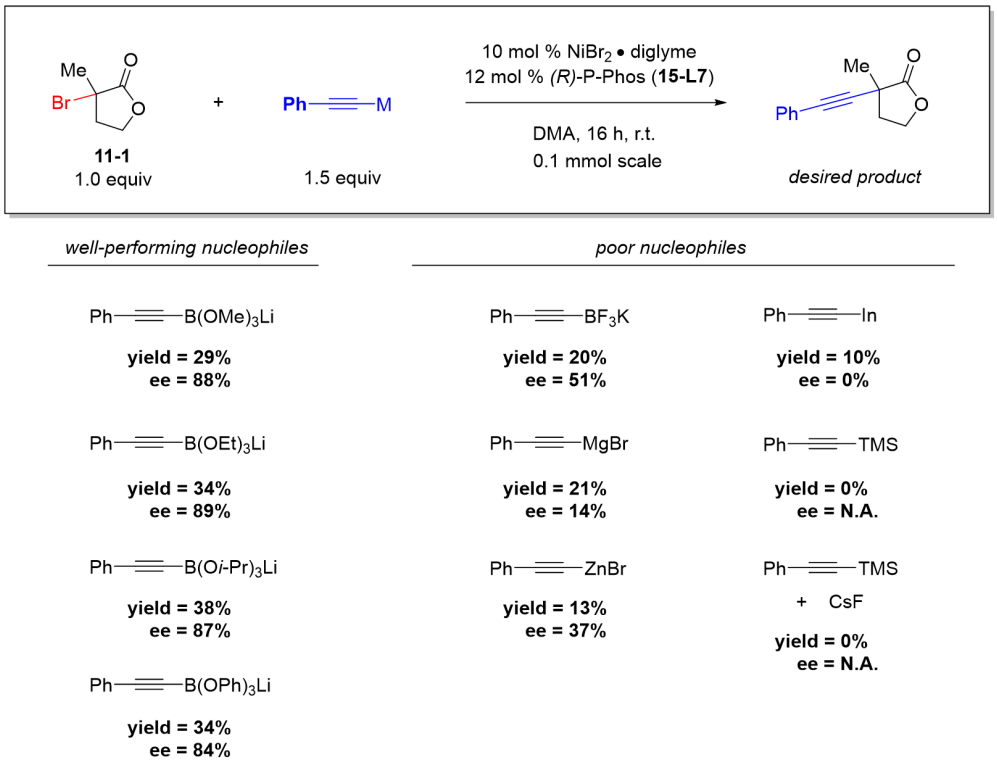

Figure 2.17: Nucleophile metal terminus screening.

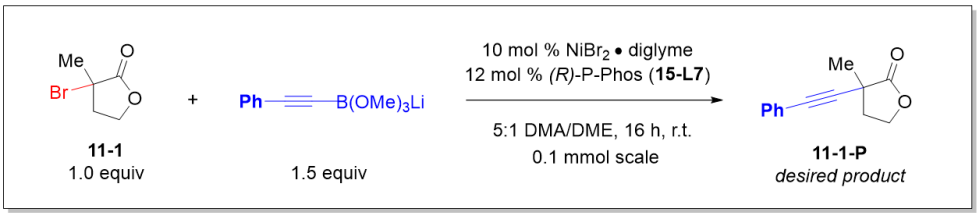

Variation from standard conditions	yield (%)	conversion (%)	ee (%)
none	**29**	**>99**	**+90**
(S)-P-Phos	**29**	**>99**	**-90**
(R)-P-XylPhos	**34**	**>99**	**+94**
no nickel salt	**0**	**0**	**N.A.**
no ligand	**0**	**0**	**N.A.**
no nickel salt and no ligand	**0**	**0**	**N.A.**

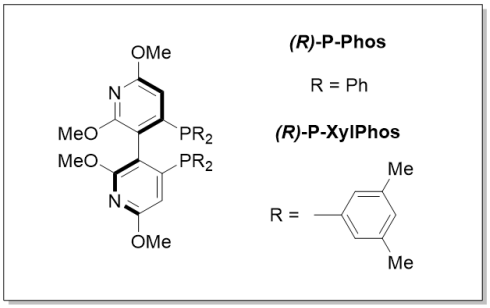

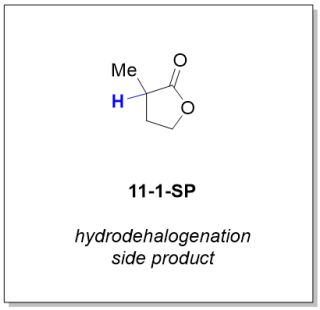

Figure 2.18: Variations on standard conditions for enantioselective alkynylation.

both enantioenrichment and desired product formation. Omitting either the nickel precatalyst or ligand from the reaction shut down reactivity completely. Employing the (S)-enantiomer of the ligand afforded the opposite enantiomer 11-1-P with the same yield.

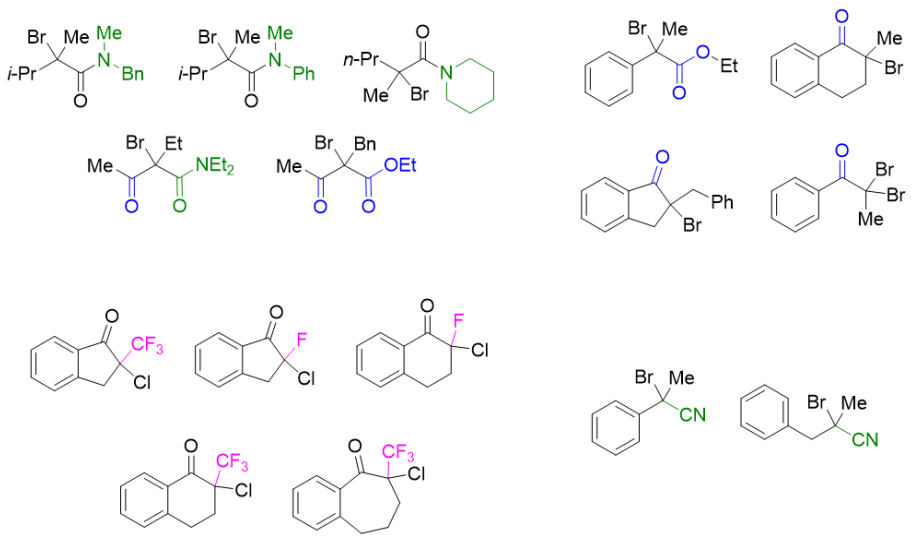

Figure 2.19: Substrates unsuccessful for enantioselective alkynylation.

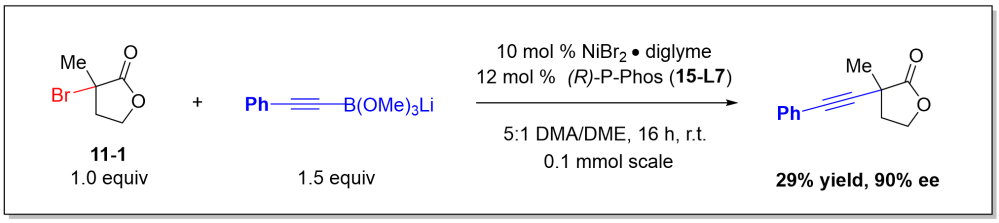

Figure 2.20: Enantioselective alkynylation of tertiary electrophiles by nickel-catalyzed cross-coupling.

Conclusion

A novel methodology is presented for the enantioselective construction of quaternary centers through the nickel-catalyzed alkynylation of racemic tertiary electrophiles (Figure 2.20) The substrate with highest yield and enantioselectivity of alkynylated product was α-bromo-α-methyl-γ-butyrolactone, which afforded high enantioenriched product using the bidentate phosphine ligand *(R)*-P-Phos. Screening of nickel precatalyst, ligand, nucleophile, solvent, temperature, and reaction time provided the best enantioselective result of 29% yield and 90% ee with the ligand *(R)*-P-Phos. The construction of enantioselective quaternary centers with cross-coupling catalysis is a powerful tool to explore chemical space, with relevance to pharmaceutical and materials applications.

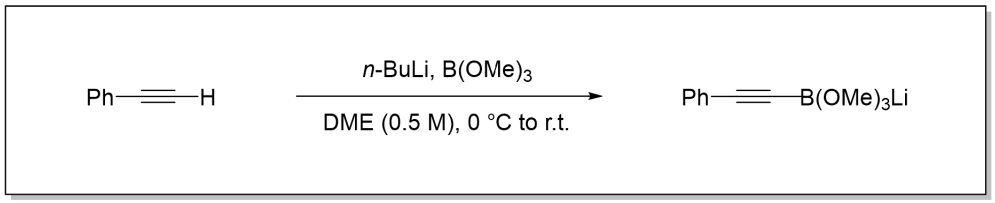

Figure 2.21: Synthesis of an alkynylboron reagent.

Experimental

Standard Procedure for Alkynylation

In a nitrogen-filled glovebox, *(R)*-P-Phos (7.7 mg, 0.012 mmol), NiBr2 · diglyme (3.5 mg, 0.010 mmol), and DMA (1.0 mL) were added in turn to an oven-dried 4-mL vial equipped with a stir bar, then sealed with a PTFE-lined septum cap. After being stirred at r.t. for 45 minutes (black, homogenous solution), the cap was opened, the alkyl bromide electrophile was added as a stock solution in DMA (0.5 M, 0.2 mL, 0.10 mmol), and a solution of trimethoxy(phenylethynyl)borate (0.3 mL, 0.150 mmol) in DME was added dropwise. The vial was sealed again with the septum cap and wrapped with electrical tape to exclude air, and the vial was removed from the glovebox. The reaction mixture was stirred at r.t. for 16 h and quenched by the addition of MeOH (1.0 mL). The internal standard n-dodecane (22 µL, 0.10 mmol) was then added. The mixture was filtered through a small plug of silica gel, which was then flushed with Et2O (15 mL). Afterwards 0.10 mL aliquot of the filtrate was diluted to 1 mL with acetone and was measured by GC (100-210°C, 30 min) to analyze conversion and yield. The remainder of the filtrate was concentrated, and the product was isolated by preparative TLC (1:4 hexanes/EtOAc). The enantiopurity of the product was determined by chiral HPLC (OD column, 2% i-PrOH in hexanes, 30 min).

Preparation of Alkynylboron Reagent

In a nitrogen-filled glovebox, an oven-dried 20 mL vial was equipped with a stir bar, was charged with DME (3.0 mL), and closed with a PTFE-lined septum cap. The vial was removed from the glovebox and was attached to nitrogen flow on a Schlenk line. Phenylacetylene (0.22 mL, 2.0 mmol) was added to the 20-mL vial which had been pre-cooled to 0 °C, followed by addition of n-BuLi (2.5 M in hexane, 0.80 mL, 2.0 mmol) dropwise at 0 °C. The mixture was allowed to stir at 0 °C for another 5 min and then warmed to r.t. The vial was reintroduced into the glovebox. After

stirring at r.t. for 10 min, trimethyl borate (0.25 mL, 2.2 mmol) was added dropwise to the alkynyllithium solution. The mixture was allowed to stir for 20 min at r.t. and was then used directly for the cross-coupling reaction.

References

(1) Quasdorf, K. W.; Overman, L. E. *Nature* **2014**, *516*, 181–191.

(2) Lovering, F.; Bikker, J.; Humblet, C. *J. Med. Chem.* **2009**, *52*, 6752–6756.

(3) Fu, G. C. *ACS Cent. Sci.* **2017**, *3*, 692–700.

(4) Trost, B. M.; Jiang, C. *Synthesis* **2006**, *3*, 369–396.

(5) Vitaku, E.; Smith, B. R.; Smith, D. T.; Njarðarson, J. T. Top US Pharmaceutical Products of 2013, `http://njardarson.lab.arizona.edu/sites/njardarson.lab.arizona.edu/files/TopUSPharmaceuticalProductsof2013.pdf`.

(6) Martín Castro, A. M. *Chem. Rev.* **2004**, *104*, 2939–3002.

(7) Mase, N.; Tanaka, F.; Barbas III, C. F. *Angewandte Chemie International Edition* **2004**, *43*, 2420–2423.

(8) Corey, E. J. *Angewandte Chemie International Edition* **2002**, *41*, 1650–1667.

(9) Tsuji, T.; Yorimitsu, H.; Oshima, K. *Angew. Chem. Int. Ed. Engl.* **2002**, *41*, 4137–4139.

(10) Ohmiya, H.; Tsuji, T.; Yorimitsu, H.; Oshima, K. *Chemistry – A European Journal* **2004**, *10*, 5640–5648.

(11) Someya, H.; Ohmiya, H.; Yorimitsu, H.; Oshima, K. *Org. Lett.* **2008**, *10*, 969–971.

(12) Sai, M.; Yorimitsu, H.; Oshima, K. *BCSJ* **2009**, *82*, 1194–1196.

(13) Sai, M.; Someya, H.; Yorimitsu, H.; Oshima, K. *Org. Lett.* **2008**, *10*, 2545–2547.

(14) Mitamura, Y.; Asada, Y.; Murakami, K.; Someya, H.; Yorimitsu, H.; Oshima, K. *Chemistry – An Asian Journal* **2010**, *5*, 1487–1493.

(15) Dudnik, A. S.; Fu, G. C. *J. Am. Chem. Soc.* **2012**, *134*, 10693–10697.

(16) Zultanski, S. L.; Fu, G. C. *J. Am. Chem. Soc.* **2013**, *135*, 624–627.

(17) Liang, Y.; Fu, G. C. *J. Am. Chem. Soc.* **2014**, *136*, 5520–5524.

(18) Kainz, Q. M.; Matier, C. D.; Bartoszewicz, A.; Zultanski, S. L.; Peters, J. C.; Fu, G. C. *Science* **2016**, *351*, 681–684.

(19) Wang, Z.; Yin, H.; Fu, G. C. *Nature* **2018**, *563*, 379–383.

(20) Ma, S.; Han, X.; Krishnan, S.; Virgil, S. C.; Stoltz, B. M. *Angewandte Chemie International Edition* **2009**, *48*, 8037–8041.

(21) Kikushima, K.; Holder, J. C.; Gatti, M.; Stoltz, B. M. *J. Am. Chem. Soc.* **2011**, *133*, 6902–6905.

(22) Liu, W.-B.; Reeves, C. M.; Stoltz, B. M. *J. Am. Chem. Soc.* **2013**, *135*, 17298–17301.

(23) Wang, J.; Ong, M. T.; Kouznetsova, T. B.; Lenhardt, J. M.; Martínez, T. J.; Craig, S. L. *J. Org. Chem.* **2015**, *80*, 11773–11778.

(24) Zhou, Q.; Cobb, K. M.; Tan, T.; Watson, M. P. *J. Am. Chem. Soc.* **2016**, *138*, 12057–12060.

(25) Huang, C.-Y. (; Doyle, A. G. *J. Am. Chem. Soc.* **2015**, *137*, 5638–5641.

(26) Johnson, C.; Albrecht, M. *Catal. Sci. Technol.* **2018**, *8*, 2779–2783.

(27) Karunananda, M. K.; Mankad, N. P. *J. Am. Chem. Soc.* **2015**, *137*, 14598–14601.

(28) Ishii, Y.; Miyashita, K.; Kamita, K.; Hidai, M. *J. Am. Chem. Soc.* **1997**, *119*, 6448–6449.

(29) Akana, J. A.; Bhattacharyya, K. X.; Müller, P.; Sadighi, J. P. *J. Am. Chem. Soc.* **2007**, *129*, 7736–7737.

(30) Jackson, W. R.; Perlmutter, P.; Smallridge, A. J. *Tetrahedron Letters* **1988**, *29*, 1983–1984.

(31) Rucker, R. P.; Whittaker, A. M.; Dang, H.; Lalic, G. *J. Am. Chem. Soc.* **2012**, *134*, 6571–6574.

(32) Persich, P.; Llaveria, J.; Lhermet, R.; de Haro, T.; Stade, R.; Kondoh, A.; Fürstner, A. *Chemistry – A European Journal* **2013**, *19*, 13047–13058.

(33) Trost, B. M.; Li, C.-J., *Modern Alkyne Chemistry: Catalytic and Atom-Economic Transformations*; Wiley: 2014.

(34) Crespo-Quesada, M.; Cárdenas-Lizana, F.; Dessimoz, A.-L.; Kiwi-Minsker, L. *ACS Catal.* **2012**, *2*, 1773–1786.

(35) Meldal, M.; Tornøe, C. W. *Chem. Rev.* **2008**, *108*, 2952–3015.

(36) Pickens, C. J.; Johnson, S. N.; Pressnall, M. M.; Leon, M. A.; Berkland, C. J. *Bioconjug Chem* **2018**, *29*, 686–701.

(37) Tang, S.; Liu, Y.; Gao, X.; Wang, P.; Huang, P.; Lei, A. *J. Am. Chem. Soc.* **2018**, *140*, 6006–6013.

(38) Ye, F.; Ma, X.; Xiao, Q.; Li, H.; Zhang, Y.; Wang, J. *J. Am. Chem. Soc.* **2012**, *134*, 5742–5745.

(39) Cheung, C. W.; Ren, P.; Hu, X. *Org. Lett.* **2014**, *16*, 2566–2569.

(40) Gil-Negrete, J. M.; Pérez Sestelo, J.; Sarandeses, L. A. *Org. Lett.* **2016**, *18*, 4316–4319.

(41) Negishi, E.-i.; Qian, M.; Zeng, F.; Anastasia, L.; Babinski, D. *Org. Lett.* **2003**, *5*, 1597–1600.

(42) Caeiro, J.; Pérez Sestelo, J.; Sarandeses, L. A. *Chemistry* **2008**, *14*, 741–746.

(43) Fang, H.; Yang, Z.; Zhang, L.; Wang, W.; Li, Y.; Xu, X.; Zhou, S. *Org. Lett.* **2016**, *18*, 6022–6025.

(44) Cui, X.-Y.; Ge, Y.; Tan, S. M.; Jiang, H.; Tan, D.; Lu, Y.; Lee, R.; Tan, C.-H. *J. Am. Chem. Soc.* **2018**, *140*, 8448–8455.

(45) Choi, J.; Fu, G. C. *Science* **2017**, *356*, eaaf7230.

(46) Schley, N. D.; Fu, G. C. *J. Am. Chem. Soc.* **2014**, *136*, 16588–16593.

Chapter 3

EMBEDDED MEAN-FIELD THEORY FOR SOLUTION-PHASE TRANSITION-METAL POLYOLEFIN CATALYSIS

ABSTRACT

Decreasing the wall-clock time of quantum mechanics/molecular mechanics (QM/MM) calculations without sacrificing accuracy is a crucial prerequisite for widespread simulation of solution-phase dynamical processes. In this work, we demonstrate the use of embedded mean-field theory (EMFT) as the QM engine in QM/MM molecular dynamics (MD) simulations to examine polyolefin catalysts in solution. We show that employing EMFT in this mode preserves the accuracy of hybrid-functional DFT in the QM region, while providing up to 20-fold reductions in the cost per SCF cycle, thereby increasing the accessible simulation time-scales. We find that EMFT reproduces DFT-computed binding energies and optimized bond lengths to within chemical accuracy, as well as consistently ranking conformer stability. Furthermore, solution-phase EMFT/MM simulations provide insight into the interaction strength of strongly coordinating and bulky counterions.

Introduction

Catalyst design in transition-metal catalysis typically requires extensive experimental optimization to achieve desired product characteristics [1]. Efficient catalysts—many of which have complex ligand structures—are often difficult and expensive to synthesize. To circumvent the bottleneck this presents in research and development efforts, advances in computational methods can help accelerate the identification of promising ligands [2]. *De novo* catalyst design is challenging due to the subtle interplay of electronic and steric effects on the performance of the catalyst under specific reaction conditions. Further complicating catalyst design are the important effects of solvent, conformational flexibility, and counterions at finite temperature and concentration [3]. New methods are needed to provide reliable computational insight into the effective design of catalysts in their solvation environment.

The combined quantum mechanics/molecular mechanics (QM/MM) method [4, 5] has proven effective in a variety of applications including biological reactions [6–11] and solution-phase chemistry [12–16], due to its ability to address both dynamical effects in multi-scale systems along with local bond-making and bond-breaking events. The cost of a single QM/MM MD step is usually dominated by that of the force evaluation for the QM region, since the MM interactions have a simple analytic form. Therefore, managing the cost of the QM calculation is an important objective for the development of computationally efficient solution-phase QM/MM simulations.

Quantum embedding offers an appealing strategy for reducing the computational costs associated with the QM regions while preserving its accuracy. For example, wavefunction-in-(density functional theory) quantum embedding methods [17–20] provide high (i.e., coupled-cluster theory) accuracy in the QM region at a significant reduction in cost versus a full wavefunction-method description [21, 22], although this approach remains too costly for widespread use in QM/MM MD simulations.

In the current work, we employ an alternative quantum embedding approach in the QM region, specifically embedded mean-field theory (EMFT) [23, 24], which provides a high-quality mean-field description (such as DFT with a hybrid functional using a large atomic-orbital basis set) for a subsystem of the QM region, while the remainder of the QM region is described using a less costly mean-field method (such as DFT with a GGA functional using a small atomic-orbital basis set). A key advantage of the method is that it does not require specification of link atoms that connect the subsystems, nor does it require specification of the number of subsystem

spin states or the number of electrons per subsystem. Previous work has shown that EMFT can be much more accurate than both the point-charge [25] and ONIOM [26, 27] schemes for subsystem embedding, particularly for systems that involve partitioning across delocalized covalent bonds [23, 28]. EMFT has additionally been benchmarked for open-shell systems [23], for deprotonation reactions [29], and for the linear-response description of excited states [30]. As we will show, this leads to tangible advances in terms of the information we can glean in the application area we study.

Polyolefins are the most widely used class of polymers [31] whose industrial importance is in part due to the tunability of their mechanical and physical properties, such as elasticity and opacity. Precise control of these macroscopic properties requires an atomic-scale mapping of the barriers of the elementary steps in the polymerization mechanism (Figure 3.1) [32], where the goal is to design molecular catalysts that offer superior control of product selectivity over their heterogeneous analogues [33]. Nuclear magnetic resonance (NMR) studies have suggested that configurational sampling of the solvent and counterion degrees of freedom near the catalyst play a crucial role in its functionality [34], which necessitates the application of dynamic rather than static modeling techniques. A chemically accurate description of the electronic structure near the active site is necessary to reliably describe reactivity at the active site. For these reasons, QM/MM studies have typically been used to study transition-metal catalysts in solution [35–40]. In this work, we show that replacing DFT with EMFT for the QM subsystem in these solution-phase QM/MM simulations of organometallic compounds largely preserves the accuracy of the description for these organometallic compounds while substantially improving computational efficiency.

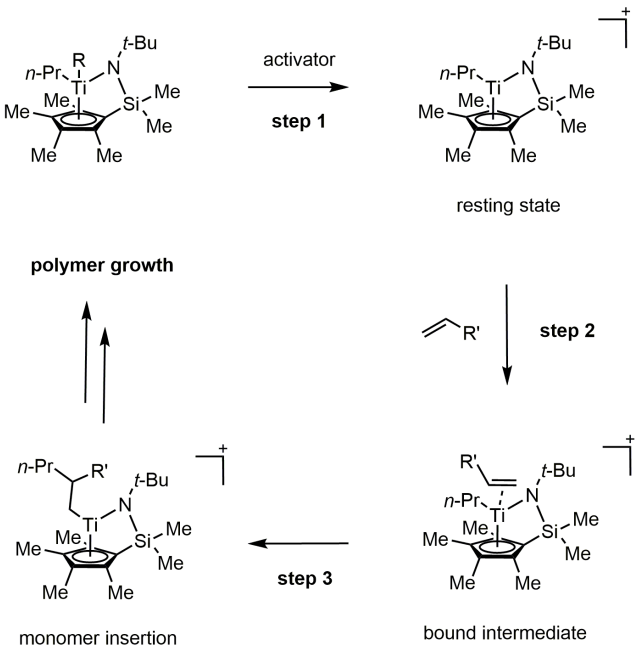

Figure 3.1: Initial steps leading up to the catalytic cycle of a Group (IV) metal-catalyzed olefin polymerization, including abstraction of an alkyl group (represented as R) by an oxidizing activator reagent to form the catalytically-active resting state (Step 1), binding of the first monomer to the resting state species (Step 2), and insertion of bound monomer into the initial alkyl (here, *n*-propyl) ligand (Step 3). Afterwards, monomer binding and insertion into the growing polymer chain repeat until termination.

The current work focuses on four archetypal Group (IV) molecular catalysts for olefin polymerization (Figure 3.2), which include both metallocene and post-metallocene structures. Catalyst 1 is a constrained geometry complex (CGC) of the metallocene class of polyolefin catalysts [41, 42]. Catalyst 2 is a post-metallocene structure, where the reaction of interest in this case is the binding of propylene to the Hf^{4+} active site [43]. The competition between the binding of ethylene and propylene in the polymerization process influences the branching ratio in the final product, which influences its bulk material properties. Catalyst 3 and Catalyst 4 are also post-metallocene structures, which have been previously reported to produce olefin block copolymers with favorable elastomeric properties [44]. (The full chemical names of the catalysts are provided in the Supporting Information.)

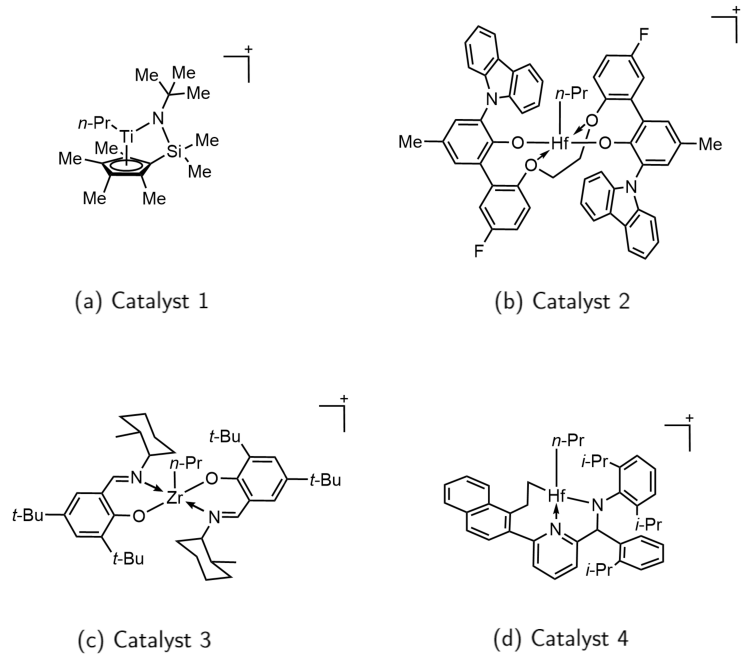

(a) Catalyst 1 (b) Catalyst 2

(c) Catalyst 3 (d) Catalyst 4

Figure 3.2: Transition-metal polyolefin catalysts considered here (resting state depicted). (a) Catalyst 1 is a metallocene complex belonging to the constrained geometry complex (CGC) class. (b) Catalyst 2 is a post-metallocene catalyst containing bisphenol ligands. (c) Catalyst 3 is a post-metallocene FI-type catalyst containing Schiff base amines. (d) Catalyst 4 is a post-metallocene catalyst with a pyridyl-amido motif.

Computational Methods

Density functional theory (DFT) is widely used for *ab initio* simulations because of its balance between accuracy and computational cost. For organometallic compounds in particular [45–48], various DFT studies have demonstrated the importance of using hybrid exchange correlation functionals [49–52] which include some fraction of exact Hartree-Fock exchange, although such hybrid functionals are typically more computationally expensive than those that employ the generalized gradient approximation (GGA) alone [53]. Embedded mean-field theory (EMFT) [23, 24] seeks the best of these two worlds—hybrid functional-like predictions at a computational cost similar to that of the GGA, yielding experimentally relevant quantities with chemical accuracy [28]. EMFT is a simple, self-consistent method that provides a high-level DFT (or other mean-field) description on a subset of the system and a lower-level DFT (or other mean-field) description on the remainder [23].

All DFT and EMFT calculations reported here are performed using the *entos* package [54]. For the B3LYP functional used in the paper, the VWN3 local correlation energy[55] is employed. We employ the density-corrected implementation of the method (DC-EMFT) to prevent unphysical collapse of the electronic density [24]. The exact-exchange contributions to the coupling between the high- and low-level subsystems are treated using the EX0 scheme [23]. For the predictions of catalyst conformer stability, configurational sampling was performed using thermostatted molecular dynamics on the GFN1-xTB[56] potential using the *entos* package [54]. A linear cooling schedule from 800 K to 100 K was used, with a total sampling time of 70 ps and time step of 1 fs. Sampled configurations were subsequently optimized using (B3LYP/Def2-SVP).

QM/MM simulations are carried out by interfacing *entos*[54] with the GROMACS 2018.1 molecular dynamics software [57]. The toluene solvent is described using the modification of the OPLS-AA[58] force-field by Caleman and coworkers [59][60], and σ and ϵ values for the titanium atom are taken from Cu^{2+} in the OPLS-AA database. Partial charges of the metal complex are obtained from Mulliken population analysis[61] performed on the complex using (B3LYP/Def2-SVP). The force-field parameters for borate counterions, including methyl [tris(pentafluorophenyl)]borate, tetrakis(pentafluorophenyl)borate, and BF_4^-, are obtained from a previous study [62]. GROMACS parameter and topology files employed in this study are provided in the Supporting Information.

QM/MM simulations are carried out with electrostatic interactions calculated using the reaction-field-zero method [63]. The charge-group cutoff scheme is used, with the solvent molecules comprised of neutral charge groups and with the catalyst and counterion comprised of charge groups with net charges. Electrostatic coupling between the QM and MM particles is evaluated through the electrostatic embedding scheme. Other non-bonded interactions between the QM and MM particles are calculated using the Lennard-Jones potential with parameters provided in the Supporting Information.

All covalent bonds in the solvent and counteranion structures are constrained using the LINCS algorithm [64]. The leap-frog integrator is used with a 1 fs time step. Periodic boundary conditions (PBCs) are used, with a 1.2 nm cutoff for electrostatic and vdW interactions. The electrostatic cutoff is applied with respect to the distance between the geometrical (i.e., un-mass weighted) centers of the charge groups. When employed, the Nosé-Hoover thermostat [65] and the Parrinello-Rahman barostat [66]

are utilized with a temperature of 298 K, a pressure of 1 bar, and a damping time constant of 1 ps.

The initial configurations for the QM/MM simulations are prepared as follows: The solvated catalyst and counterion were initialized from a pre-equilibrated simulation cell, obtained using the `solvate` utility within the GROMACS package [67], and performing a 1 ns isothermal-isobaric (NpT) equilibration using fully classical MD. For the Cl^-, BF_4^-, $CH_3B(C_6F_5)^{3-}$ and $B(C_6F_5)^{4-}$ simulations, the number of solvent molecules is respectively 196, 196, 193, and 195. During this initial equilibration, the cubic simulation cell adopts a sidelength of approximately 3.3 nm centered around the catalyst. The system was then equilibrated for 5 ps in the NpT ensemble using the GFN1-xTB/MM potential, then for at least 5 ps in the NVT ensemble using the EMFT/MM potential, before performing production runs in the NVE ensemble using the EMFT/MM potential. Each QM/MM production run has a simulation time of at least 30 ps.

Results and Discussion

Benchmarking EMFT Accuracy and Cost

We begin by benchmarking the accuracy and efficiency of EMFT for the prediction of structure and reactivity of the archetypal Group (IV) olefin polymerization catalysts shown in Figure 3.2. In particular, we focus on monomer binding energies, resting-state bond lengths, and relative-energy rankings of a resting-state conformer using EMFT.

For DFT calculations, we specify the exchange correlation functional and basis set with the standard nomenclature (functional/basis set). For EMFT, we specify the level of theory via ((high-level)-in-(low-level)); for example, ((B3LYP/Def2-SVP)-in-(PBE/6-31G)) denotes the use of EMFT with the B3LYP functional and Def2-SVP basis for the high-level subsystem and the PBE functional and 6-31G basis for the low-level subsystem.

Substrate Binding Energies

The binding of a monomer substrate is an important elementary step in the overall polymerization mechanism (Figure 3.1). We compare the binding energy values obtained by EMFT ((B3LYP/Def2-SVP)-in-(PBE/6-31G)) to those calculated using high-level DFT (B3LYP/Def2-SVP) and low-level DFT (PBE/6-31G). Additionally, we investigate the convergence of EMFT binding energy values to the high-level DFT

result, as a function of high-level subsystem size. To calculate the binding energy using DFT or EMFT, we take the difference between the single-point energies of the bound intermediate product and the resting state and unbound ethylene reactants (Step 2, Figure 3.1). The unbound ethylene monomer is treated with (B3LYP/Def2-SVP) for EMFT and high-level DFT, and with (PBE/6-31G) for low-level DFT. All calculations are performed at geometries that are optimized at the B3LYP level of theory; these structures for both the resting-state and substrate-bound intermediates for all four catalysts are provided in the Supporting Information.

For EMFT energy evaluations of the resting state and bound intermediate catalyst structures, the partitioning of the system is illustrated in Figure 3.3 and Figure 3.4. For each catalyst, four subsystem sizes are explored using EMFT. To compactly label the high-level regions for each subsystem size, we assign each atom a label from 1–4 in the resting state structure of the catalyst (Figure 3.3), with hydrogen atoms atoms sharing the index of the heavy atom to which they are bonded. Hence, a partitioning scheme $X \in \{1, 2, 3, 4\}$ defines the high-level subsystem as all atoms which have an index value less than or equal to X. For example, partitioning scheme 2 places both the blue (label 1) and green (label 2) atoms in the high-level subsystem. The atomic labelling for the resting states as shown in Figure 3.3 extend to the bound intermediate; as shown in Figure 3.4, the monomer substrate in the unbound and bound intermediate structure is always included in the high-level subsystem.

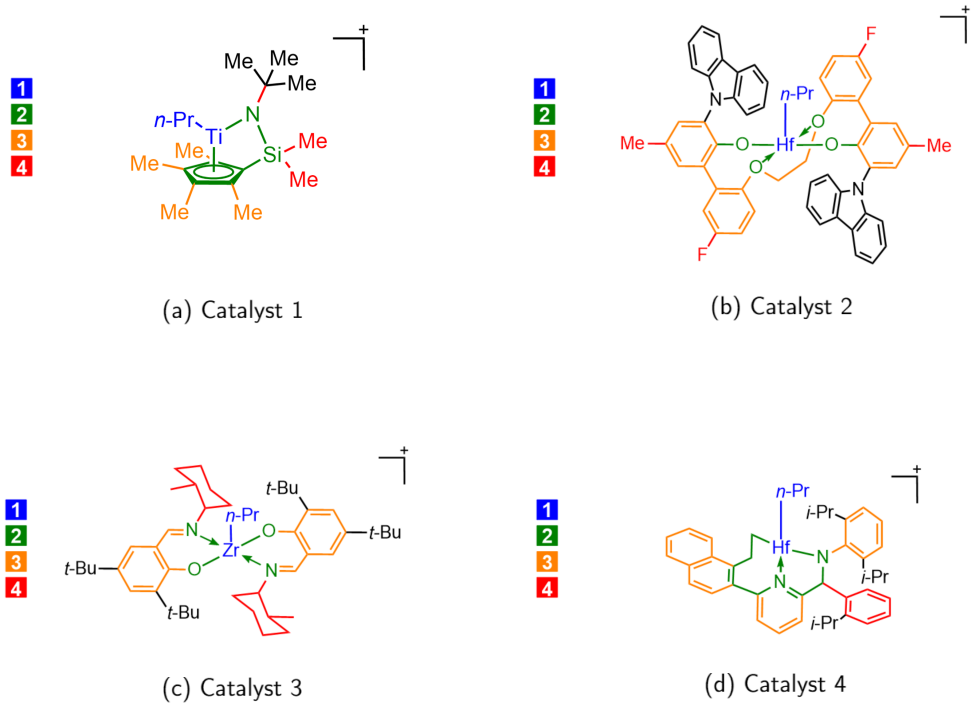

Figure 3.3: Definition of the high-level subsystem by atomic labeling (shown for resting state structures) for EMFT partitioning. For a partitioning scheme X indexed as 1, 2, 3, 4, the atoms with indices of less than or equal to X are in the high-level region, and the remaining atoms are in the low-level region; moieties indicated in black are in all cases treated at the low level. For each atom that is joined by bonds containing different colors, the label corresponding to the lower index is used. All implicit hydrogen atoms share the index of the atom to which they are bonded. For example, partitioning scheme 2 places the blue- and green-labeled atoms in the high-level subsystem, and the remaining atoms in the low-level subsystem.

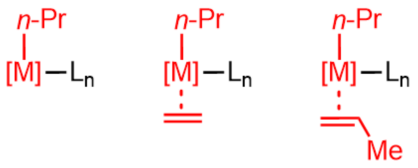

Figure 3.4: Illustration of the partitioning for the minimal high-level subsystem (Figure 3.3, $X = 1$) for the resting state, ethylene-bound intermediate, and propylene-bound intermediate, respectively. The high-level subsystem (represented in red) always contains at least the metal, *n*-propyl group, and if present in the structure, the bound monomer.

Binding energies for ethylene (black dots) and propylene (gray dots) are plotted as a function of the number of atoms in the high-level subsystem (Figure 3.5). All binding energies are reported relative to the ethylene binding energy calculated by low-level DFT (PBE/6-31G). On each plot, the first point corresponding to zero atoms in the high-level subsystem is obtained from the low-level DFT (PBE/6-31G) energy, and the last point corresponding to the inclusion of all atoms in the high-level subsystem is obtained from the high-level (B3LYP/Def2-SVP) energy. The four intermediate points indicate the EMFT energy calculated using increasing sizes of the high-level subsystem. To indicate the target range of chemical accuracy, the light and dark green bar indicates ±1 kcal/mol deviation from the high-level DFT (B3LYP/Def2-SVP) propylene and ethylene binding energy, respectively.

EMFT-calculated ethylene and propylene energies converge to the high-level DFT result for all four catalysts (Figure 3.5). For all four of the catalyst systems, the minimal subsystem – including the growing polymer chain, the metal center, and the unbound or bound monomer – is sufficient to obtain the energy of ethylene and propylene binding to within ∼1 kcal mol^{-1} of the high-level calculation on the full system. For some intermediate subsystem sizes, the error is slightly larger than 1 kcal mol^{-1}, but in general the deviations are modest. Notably, this effect holds for large catalysts, including the largest catalyst studied (Catalyst 3, with 127 atoms in the resting state form), for which the computational speed-ups will be greatest using EMFT. It is particularly encouraging that EMFT consistently provides good accuracy across all four catalyst systems, which vary with respect to the transition metal and ligand scaffold.

Figure 3.6 addresses the accuracy with which EMFT predicts the relative binding energy of ethylene versus propylene in the four catalyst systems, a quantity that is of central interest in determining selectivity with respect to unwanted side-products during polyolefin catalysis. In all four cases, EMFT is performed using the smallest and least computationally expensive high-level subsystem considered (partitioning scheme 1). Comparing these EMFT results with respect to high-level DFT, it is clear that the lower-cost EMFT method accurately predicts ethylene and propylene binding energies across all four catalysts.

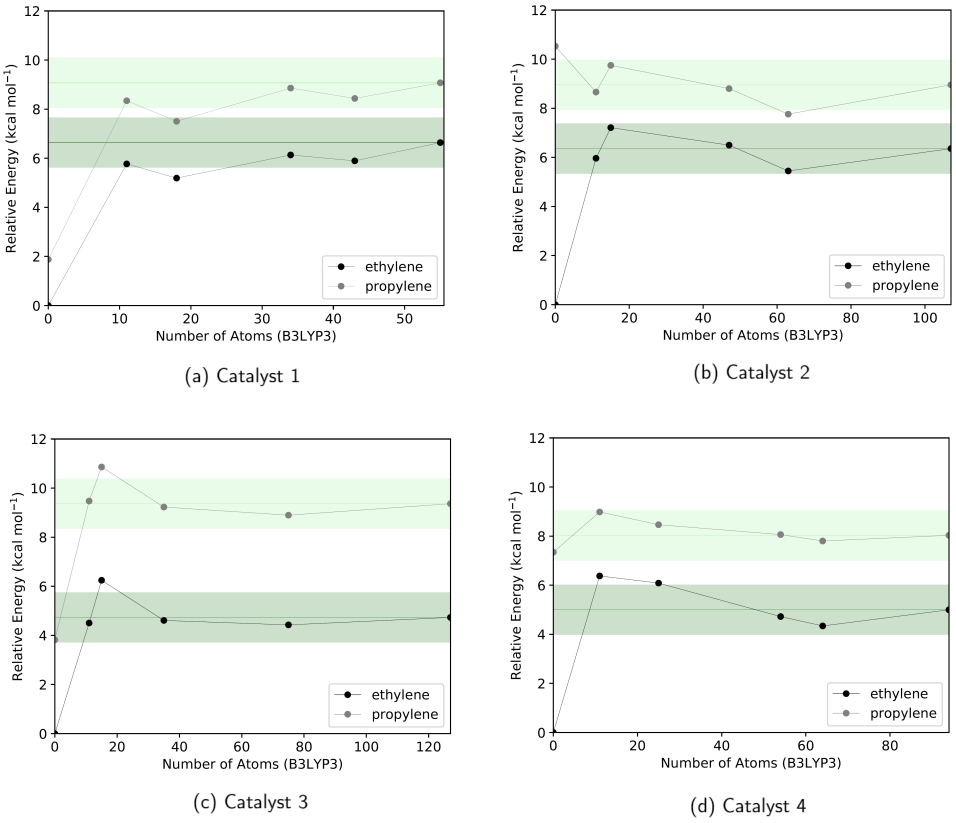

Figure 3.5: Ethylene and propylene binding energies relative to the low-level calculated ethylene binding energy (PBE/6-31G), as a function of the number of atoms in the high-level subsystem of the resting state structure. On each plot, from left to right is shown the full low-level DFT (PBE/6-31G), EMFT ((B3LYP/Def2-SVP)-in-(PBE/6-31G)) using partitioning schemes in Figure 3.3, and full high-level DFT (B3LYP/Def2-SVP). The number of atoms in each case coincide with the subsystem partitionings indicated in Figure 3.3.

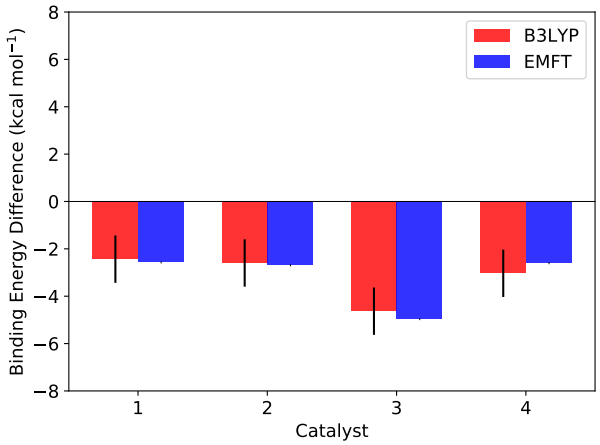

Figure 3.6: Difference in ethylene vs. propylene binding energy (ethylene – propylene) for Catalyst 1 (Ti^{4+}), Catalyst 2 (Hf^{4+}), Catalyst 3 (Zr^{4+}), and Catalyst 4 (Hf^{4+}). The differences in binding energies is evaluated with both DFT (B3LYP/Def2-SVP) and EMFT ((B3LYP/Def2-SVP)-in-(PBE/6-31G)) using the minimal subsystem partitioning (Figure 3.3, $X = 1$). A 1 kcal mol^{-1} error bar is included for comparing the DFT and EMFT binding energy differences.

Predicting Conformer Stability

An important capability in computational screening is the ability to predict the structure and relative energy of the most stable conformers. We investigate the distribution of conformers for resting state of Catalyst 3, which consists of a trigonal bipyramidal geometry with 2 oxygen ligands, 2 nitrogen ligands, and an *n*-propyl ligand. Three unique isomers are considered (Isomers 1–3, Figure 3.7), based on the orientation of the bonding connectivity at the metal site. We consider four low-energy conformers associated with each isomer, obtained via simulated annealing (see Computational Methods). Specifically, an independent simulated annealing trajectory was performed for each of the three isomers of Catalyst 3, and from each trajectory, the four lowest-energy distinct structures that were obtained after local minimization using high-level DFT (B3LYP/Def2-SVP) were included in this analysis. All structures are provided in the Supporting Information. For all calculations reported in this section, ((B3LYP/Def2-SVP)-in-(PBE/6-31G)) EMFT is performed using the smallest and least computationally expensive high-level subsystem considered (partitioning scheme 1).

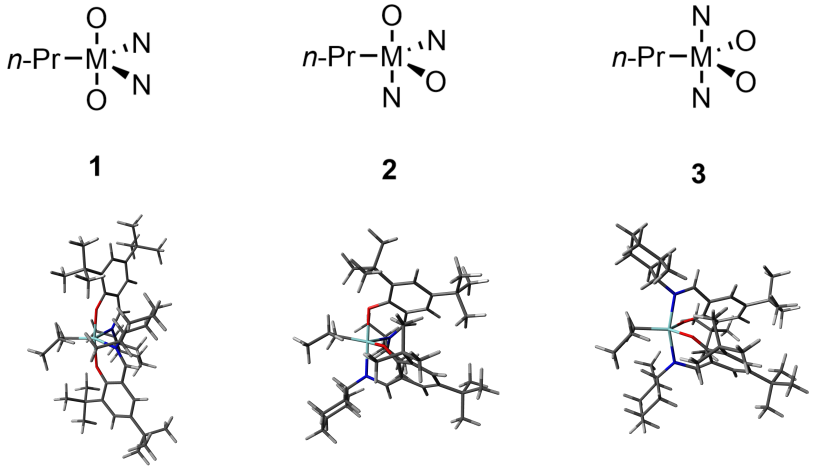

Figure 3.7: Three isomers of the Catalyst 3 resting state. Isomers 1–3 are displayed above, with different arrangements of the nitrogen- and oxygen-based ligands at the axial and equatorial sites. The *n*-propyl ligand is held at the equatorial position in all cases.

Figure 3.8a presents the correlation between the relative conformer energies computed using high-level DFT versus EMFT, for structures optimized using high-level DFT. As is clear from the plot, the prediction of conformer energy rankings from EMFT is excellent, with the rank-ordering of the 12 conformers–including those across isomers and with a given isomer–being correctly predicted using EMFT. We further note that the overall R^2 value of the correlation is 0.994, and that for every structure except the highest energy one, the EMFT relative energy predictions coincide with the high-level DFT prediction to within 1 kcal/mol (indicated by the shaded region).

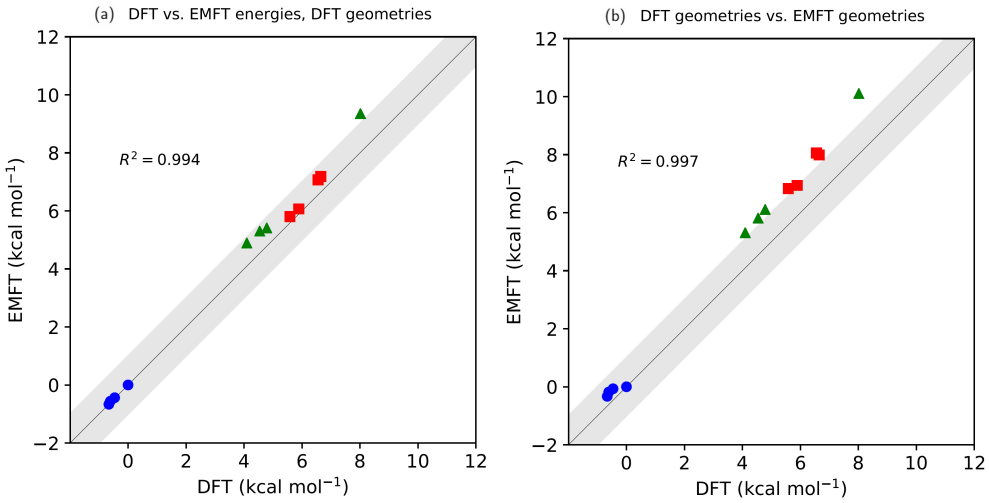

Figure 3.8: Comparison of DFT and EMFT energy rankings of the 12 conformers obtained by simulated annealing. The blue circles correspond to conformers of Isomer 1, the red squares to those of Isomer 2, and the green triangles to those of Isomer 3. The gray bar represents a 1 kcal mol^{-1} error bar at the diagonal. (a) DFT vs. EMFT energy for DFT-optimized conformer geometries. (b) DFT energy of DFT-optimized conformer geometries vs. the EMFT energy of the EMFT-optimized conformer geometries.

Figure 3.8b then tests the degree to which the optimization of the geometries using EMFT (versus high-level DFT) effects the quality of the conformer energy ranking. Each of the twelve conformer structures that were initially optimized using high-level DFT were subsequently optimized using EMFT, and the energy of high-level DFT energy (at the high-level DFT optimized geometry) is correlated against the EMFT energy (at the EMFT optimized geometry). For all cases the error between the DFT and EMFT energy is less than 2 kcal/mol. The correlation remains excellent (R^2 = 0.997), and the relative ranking of the conformer remains perfect (with the exception of two nearly iso-energetic conformers of isomer 2). These results suggest that EMFT provides a powerful tool for screening catalyst conformers, without the need for high-level DFT geometries or even single-point energies.

Predicted Geometries

From an energy perspective, Figure 3.8b indicates that EMFT provides a satisfactory description of the optimized geometry for the catalyst resting state, which tends to be the most abundant species in catalytic mechanism [68]. We now further investigate the quality of the EMFT-optimized structures for the catalyst resting state across all

Catalysts 1-4. For each resting state structure of the catalysts, geometry optimization was performed with high-level DFT (B3LYP/Def2-SVP), EMFT ((B3LYP/Def2-SVP)-in-(PBE/6-31G)), using the minimal partitioning scheme 1, and low-level DFT (PBE/6-31G).

For Catalyst 1, Table 3.1 presents representative bond lengths obtained via geometry optimization using EMFT, in comparison to the corresponding values obtained using both the low-level and high-level DFT methods. The rows of the table are grouped into distances between atoms that are within the high-level region of the EMFT description (top unshaded block), distances between atoms that span the high- and low-level regions (shaded block), and distances between atoms that are within the low-level region of the EMFT description (bottom unshaded block). Corresponding tables for Catalysts 2–4 are provided in the Supporting Information.

The general expectation of EMFT is for bonds within the high-level subsystem to be described at the quality of the high-level DFT; this is largely borne out in Table 3.1 by the fact that the difference between the EMFT and high-level DFT bond lengths (EMFT – B3LYP) for atoms within the high-level region are smaller than the corresponding difference between EMFT and the low-level DFT bond lengths (EMFT – PBE). Similarly, the there is an expectation for bonds within the low-level subsystem to be described by EMFT at the quality of the low-level DFT; this is again supported by the data in Table 3.1 by the fact that the difference between the EMFT and low-level DFT bond lengths (EMFT – PBE) for atoms within the low-level region are smaller than the corresponding difference between EMFT and the high-level DFT bond lengths (EMFT – B3LYP). For bonds that span the high- and low-level subsystems, it is seen in the table that these distances are generally more consistent with the description of the low-level DFT theory, as is expected; nonetheless, we find some cases, like the Ti–N bond length, where the description of the atoms spanning the high- and low system deviates substantially from both the high- and low-level DFT methods.

Figure 3.9 summarizes the results in Table 3.1 and generalizes them to Catalysts 2–4. In Figure 3.9a, we plot the root-mean-square-error (RMSE) for the difference between EMFT-optimized bond lengths and either high-level or low-level DFT-optimized bond lengths for atoms contained within the high-level region of the minimal EMFT partitioning. In Figure 3.9b, we present the corresponding results for bond lengths involving atoms that lie within the low-level region of the EMFT partitioning. For Catalyst 1, these results are obtained from the data reported in

Table 3.1: For Catalyst 1, bond lengths are compared between EMFT ((B3LYP/Def2-SVP)-in-(PBE/6-31G)), high-level DFT (B3LYP/Def2-SVP), and low-level DFT (PBE/6-31G). The minimal subsystem partitioning is used for EMFT (Figure 3.3, $X = 1$). Columns are grouped according to bonds located within the high-level subsystem (top unshaded block), across the high- and low-level subsystems (shaded block), or within the low-level subsystem (bottom unshaded block). Duplicate names for atoms are given superscript indexing for differentiation. The bond length computed by EMFT, the difference between the EMFT and PBE-calculated bond lengths (EMFT – PBE), and the difference between the EMFT and B3LYP-calculated bond lengths (EMFT – B3LYP) are presented.

First Atom	Second Atom	EMFT (Å)	EMFT – PBE (Å)	EMFT – B3LYP (Å)
Ti	C(n-Pr)^1	2.071	-0.010	-0.005
C(n-Pr)^1	C(n-Pr)^2	1.513	-0.012	-0.001
Ti	C(ring)^1	2.229	-0.013	-0.002
Ti	C(ring)^2	2.362	0.005	0.010
Ti	C(ring)^3	2.557	0.023	0.065
Ti	C(ring)^4	2.515	0.021	0.068
Ti	C(ring)^5	2.281	-0.009	0.018
Ti	N	1.790	-0.102	-0.104
N	Si	1.899	0.012	0.085
N	C(t-Bu)	1.510	0.001	0.015
Si	C(ring)^1	1.927	-0.004	0.018

Table 3.1, and for Catalysts 2–4, the data are obtained from the corresponding tables in the Supporting Information. It is clear that for all four catalysts, the EMFT-optimized geometries yield a description of atoms within the high-level region that is more consistent with the high-level DFT description (panel a), whereas the atoms with low-level region are more closely described at the level of the low-level DFT (panel b). These results clearly illustrate that EMFT provides improved accuracy in the high-level region while describing the remainder of the system at the quality of the low-level DFT theory.

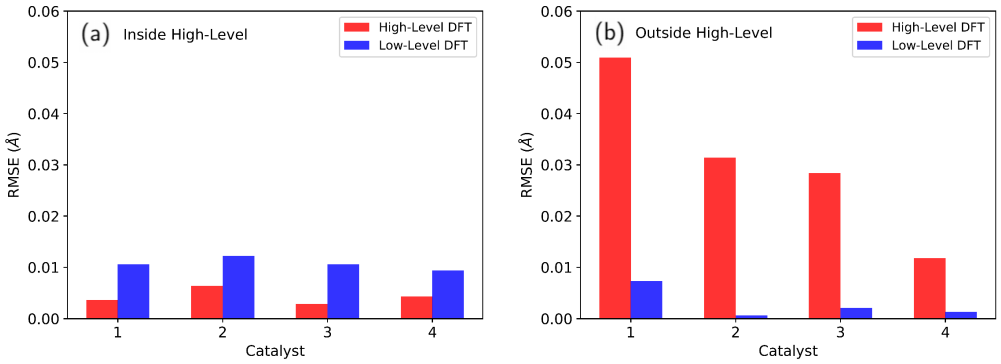

Figure 3.9: Root-mean-square error (RMSE) of bond lengths between EMFT and full-DFT geometry optimized structures for representative bonds that are (a) inside the high-level subsystem or (b) outside the high-level subsystem. The minimal subsystem partitioning is used for EMFT (Figure 3.3, $X = 1$).

Cost Analysis

The preceding results have shown that even with the minimal number of atoms in the high-level region (partitioning 1), EMFT provides a description across all four catalysts considered here that is within chemical accuracy for substrate binding, reliable for resting-state conformer stability ranking, and yields optimized geometries that are consistent with the high-level DFT method around the catalyst active site. Furthermore, as has been emphasized in previous work [23, 28], the use of EMFT brings substantial reductions in computational cost in comparison to using the high-level DFT method for the full system. The reduced cost of EMFT comes from both the reduced size of the basis set in the low-level region, as well as the lower cost of evaluating the low-level DFT exchange correlation function for the atoms in the low-level region. Specifically, in the current applications, the use of EMFT reduced the need for evaluating exact exchange contributions to only the atoms within the high-level subsystem.

Table 3.2 compares timings for EMFT ((B3LYP/Def2-SVP)-in-(PBE/6-31G)) in comparison to high-level DFT (B3LYP/Def2-SVP) and low-level DFT (PBE/6-31G) applied to the full system. In all cases, EMFT is performed using the minimal partitioning (partitioning 1). For each of the catalysts, timings are reported for the energy calculation such that 11 atoms are described in the high-level region (e.g. metal, propyl side-chain). All calculations were done on 16-core Intel Skylake dual-CPUs with a clock speed of 2.1 GHz.

Table 3.2: For the resting state structures of Catalysts 1–4, energy calculation timings for EMFT ((B3LYP/Def2-SVP)-in-(PBE/6-31G)) in comparison to high-level DFT (B3LYP/Def2-SVP) and low-level DFT (PBE/6-31G) applied to the full system. EMFT calculations employ the minimal high-level subsystem partitioning. Timings reported using 16-core Intel Skylake dual-CPUs with a clock speed of 2.1 GHz.

Catalyst	Settings	SCF Time (s)	Cycles	Total SCF Time (s)
	High-Level DFT	1.0	18	18.6
1	**EMFT**	**0.4**	**21**	**8.4**
	Low-Level DFT	0.3	22	5.7
	High-Level DFT	33.1	20	662.8
2	**EMFT**	**1.4**	**20**	**27.9**
	Low-Level DFT	1.1	20	22.6
	High-Level DFT	25.1	19	477.8
3	**EMFT**	**1.3**	**22**	**28.3**
	Low-Level DFT	1.1	25	26.5
	High-Level DFT	13.3	19	251.9
4	**EMFT**	**0.9**	**19**	**18.0**
	Low-Level DFT	0.8	20	14.8

As is seen from Table 3.2, EMFT yields a cost reduction that ranges from a factor of 4 for the smallest catalyst (Catalyst 1) to a factor of ~20 for the largest catalysts (Catalysts 2 and 3). In general, the EMFT cost is only slightly increased relative to that for the low-level DFT method. Furthermore, the number of self-consistent field iterations needed for EMFT is similar to the standard DFT methods. These results, in combination with the previously shown benchmarks of EMFT accuracy, illustrate that the method preserves accuracy of the high-level DFT method while providing vast reductions in computational cost.

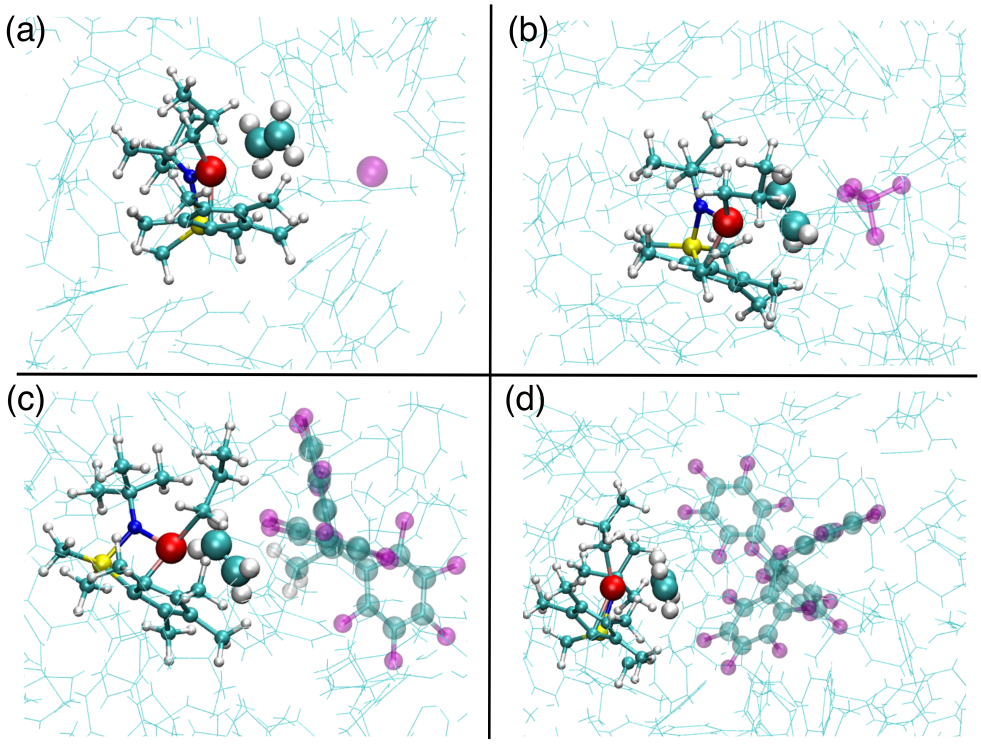

Figure 3.10: Snapshots of the QM and MM subsystems used in the EMFT/MM simulations. Catalyst 1 complex is presented as a balls-and-stick model, with Ti, Si, N, C, and H atoms colored in red, yellow, blue, cyan, and white, respectively. Toluene molecules (solvent) are shown using blue lines. From a–d respectively, the counteranions of interest, Cl^-, BF_4^-, $CH_3B(C_6F_4)^{3-}$, and $B(C_6F_5)^{4-}$, are depicted with a transparent ball-and-stick structure. Each simulation is solvated in toluene with 193 to 196 molecules in a periodic simulation cell.

Application of EMFT for QM/MM Simulations

To illustrate the applicability of EMFT for the simulation of condensed phase reactions associated with these homogeneous catalysts, we present EMFT/MM simulations (i.e., QM/MM simulations with EMFT used for the QM region) of ethylene binding to Catalyst 1. We model the ion-pairing of this cationic catalyst with four different counterions ranging from small, strongly-coordinating anions Cl^- and BF_4 to sterically-bulky, weakly-coordinating anions $CH_3B(C_6F_5)^{3-}$ and $B(C_6F_5)^{4-}$. Particular focus is given to the way in which the cationic catalyst interacts with counterions of varying size, given the crucial role that the counterion plays in catalyst efficiency [69].

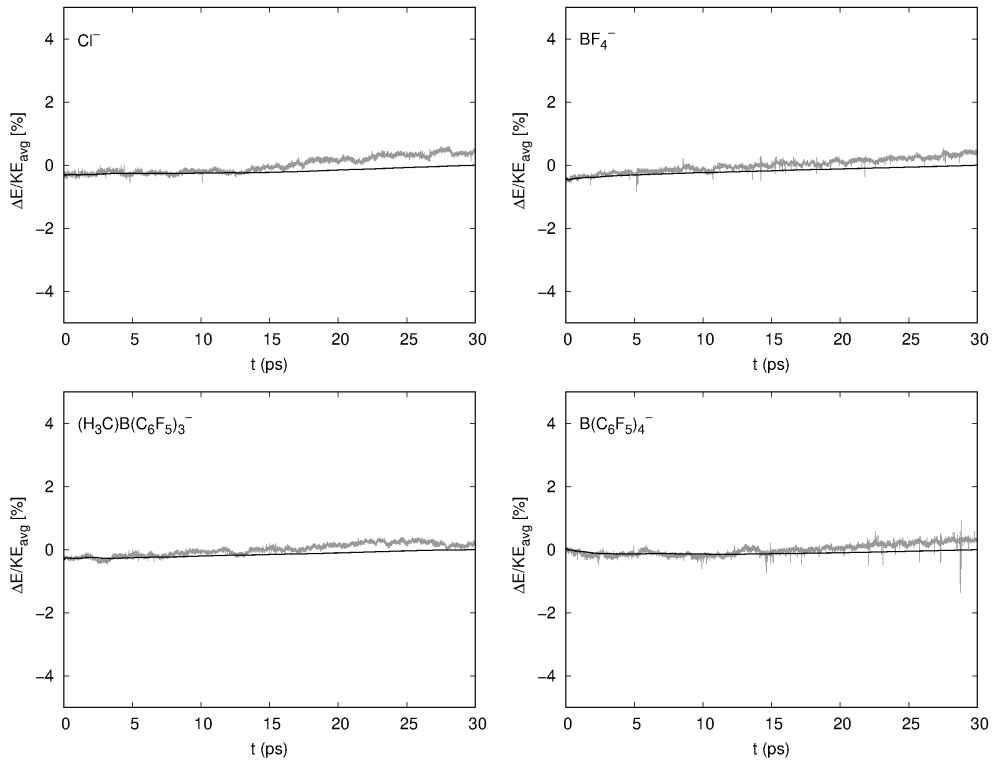

Figure 3.11: Energy conservation plots for EMFT/MM trajectories for Catalyst 1 with solvent and various counterions (indicated in each panel) in the NVE ensemble. The gray line indicates $(E(t) - E_{\text{avg}})/(\text{KE}_{\text{avg}})$, while the black line indicates the cumulative average of the same quantity.

EMFT/MM simulations are performed using EMFT ((B3LYP-D3/Def2-SVP)-in-(PBE-D3/6-31G)) with the minimal high-level subsystem partitioning and using the D3 dispersion correction in both the high- and low-level regions [70]. The ethylene-bound Catalyst 1, with 61 atoms, is included in the EMFT region while the counterions and solvent (193–196 toluene molecules) are treated within the MM region, as illustrated in Figure 3.10. Full calculation details are provided in the Computational Methods section.

As a demonstration of robustness, Figure 3.11 illustrates the energy conservation of microcanonical EMFT/MM trajectories for each of the four considered counterions. In each case, we show that there is minimal drift in the total energy, which is plotted relative to the average kinetic energy for the system of the entire trajectory. The small fluctuations and drift of the total energy in these plots over 30 ps indicates the good energy conservation of the EMFT/MM trajectories.

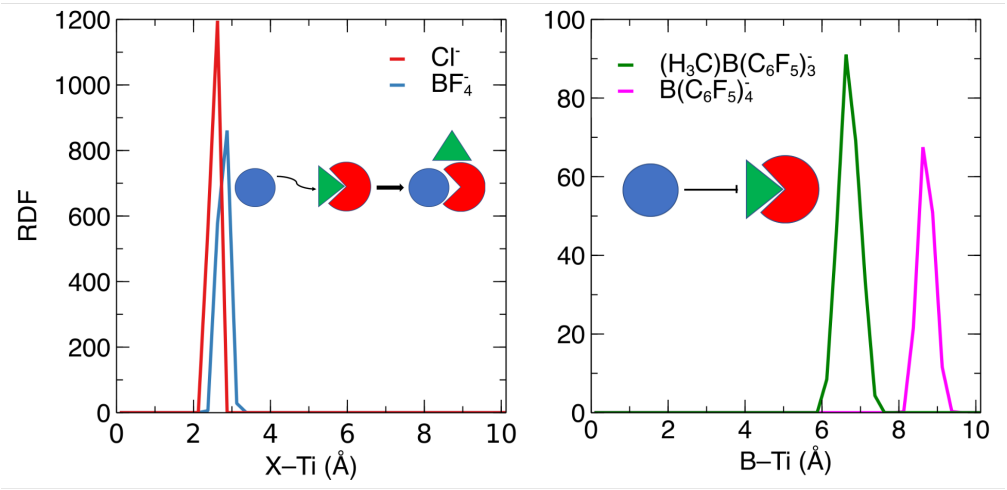

Figure 3.12: RDF for the distance between Catalyst 1 and its counterion in the four EMFT/MM simulations computed between 15–30 ps.(a) Close contact between the small counterions (blue circle) and the metal binding site leads to dissociation of ethylene (green triangle) from the catalyst (red semicircle). (b) Ethylene remains bound to the metal binding site in the presence of bulky counterions.

We qualitatively assess the strength of the interaction between the cationic catalyst and the anionic counterion using the radial distribution function (RDF) for the two species. Specifically, Figure 3.12 plots the RDF with respect to the distance between the Ti atom of Catalyst 1 and the center-of-mass of each of the four considered counterions from separate EMFT/MM simulations.

It is clear that the EMFT/MM simulations lead to qualitatively different RDF profiles for the smaller (Figure 3.12a) versus bulkier (Figure 3.12b) counteranions. The small, strongly coordinating counterions chloride (Cl^-) and tetrafluoroborate (BF_4^-) are on average more closely associated with Catalyst 1 than the bulkier counterions. Specifically Cl^- and BF_4^- counteranions are located at $\sim$ 2.5 Å from the Ti atom, which is 4 Å closer than that of $CH_3B(C_6F_5)^{3-}$ and $B(C_6F_5)^{4-}$.

The close binding of the chloride and tetrafluoroborate ions to the catalyst has direct consequences for the reactivity of the catalyst in solution. In the EMFT/MM simulations performed with these smaller counterions, the ethylene substrate that is originally bound to the catalyst is displaced from the binding site within 10 ps, driven by the formation of the close contact of these counterions with the Ti atom. Schematically, this is shown in Figure 3.12a cartoon with the counterion (blue circle) displacing the substrate (green triangle) from the catalyst (red semicircle) binding site. Conversely, in the EMFT/MM simulations involving the larger counterions

$CH_3B(C_6F_5)^{3-}$ and $B(C_6F_5)^{4-}$, the ethylene substrate remains coordinated to the Ti atom of Catalyst 1. Experimentally, it is also known that the toluene solvent will compete with the ethylene substrate for binding, although this not seen on the timescales of these simulations [71]. The simulations indicate that olefin binding (Step 2, Figure 3.1) is strongly influenced by the strength of the interaction between the counterion and metal complex. The results presented here are consistent with previous literature demonstrating that bulkier counteranions increase the efficiency of the catalyst by binding more weakly to the catalyst, thus promoting monomer binding and polymerization at the cationic active site [62, 69, 72, 73].

Conclusion

We have developed a framework for combined EMFT and QM/MM MD simulations. Our benchmarks indicate that for the wide range Group (IV) transition-metal polyolefin catalysts, using a minimal high-level region for EMFT reproduces the energetic and structural properties obtained by high-level DFT on the entire system. According to the timing data provided in Table 3.2, EMFT is able to reduce the cost of DFT calculations from a factor of 4 up to a factor of 20 per SCF iteration while maintaining the accuracy of the high-level DFT (hybrid functional). EMFT/MM simulations of counteranion binding to the cationic catalyst demonstrate energy conservation within the range expected given the truncated treatment of electrostatics, and provide insights into the nature of counteranion binding as a function of counteranion size. Our results indicate that ethylene binding to the activated catalyst is significantly influenced by the interaction between the counterion and metal complex. Close contact between the counterion and metal complex (i.e. Cl^- and BF_4^-) leads to dissociation of ethylene from the catalyst binding site.

Understanding the detailed role of the solvent and counterion environment is critical for reliable prediction of catalytic activity, and hence for the design of new catalysts. While conventional QM/MM simulations using hybrid DFT in the QM region are often unaffordable, the EMFT embedding scheme provides the desired level of accuracy at greatly reduced computational cost, by tuning in the exact exchange treatment to just a small number of atoms in the immediate vicinity of the active transition-metal center. This is a key step on the path towards widespread use of QM/MM simulation for discovery of new transition-metal catalysts, both for polyolefin catalysis, and more widely.

BIBLIOGRAPHY

(1) Poree, C.; Schoenebeck, F. *Acc. Chem. Res.* **2017**, *50*, 605–608.

(2) Busico, C. *MRS Bull.* **2013**, *38*, 224–228.

(3) Chen, C. *Nat. Rev. Chem.* **2018**, *2*, 6–14.

(4) Warshel, A.; Levitt, M. *J. Mol. Biol.* **1976**, *103*, 227–249.

(5) Warshel, A.; Karplus, M. *J. Am. Chem. Soc.* **1972**, *94*, 5612–5625.

(6) Woods, C. J.; Shaw, K. E.; Mulholland, A. J. *J. Phys. Chem. B* **2014**, *119*, 997–1001.

(7) Gong, W.; Wu, R.; Zhang, Y. *J. Comput. Chem.* **2015**, *36*, 2228–2235.

(8) Ugur, I.; Marion, A.; Aviyente, V.; Monard, G. *Biochemistry* **2015**, *54*, 1429–1439.

(9) David, R.; Jamet, H.; Nivière, V.; Moreau, Y.; Milet, A. *J. Chem. Theory Comput.* **2017**, *13*, 2987–3004.

(10) Ranaghan, K. E.; Morris, W. G.; Masgrau, L.; Senthilkumar, K.; Johannissen, L. O.; Scrutton, N. S.; Harvey, J. N.; Manby, F. R.; Mulholland, A. J. *J. Phys. Chem. B* **2017**, *121*, 9785–9798.

(11) Steinmann, C.; Olsson, M. A.; Ryde, U. *J. Chem. Theory Comput.* **2018**, *14*, 3228–3237.

(12) Ortuño, M. A.; Vidossich, P.; Ujaque, G.; Conejero, S.; Lledós, A. *Dalton Trans.* **2013**, *42*, 12165–12172.

(13) Shen, L.; Yang, W. *J. Chem. Theory Comput.* **2016**, *12*, 2017–2027.

(14) Wood, G. P. F.; Sreedhara, A.; Moore, J. M.; Wang, J.; Trout, B. L. *J. Phys. Chem. A* **2016**, *120*, 2926–2939.

(15) Zvereva, E. E.; Katsyuba, S. A.; Dyson, P. J.; Aleksandrov, A. V. *J. Phys. Chem. C* **2016**, *120*, 4596–4604.

(16) Hofer, T. S.; Hünenberger, P. H. *J. Chem. Phys.* **2018**, *148*, 222814.

(17) Manby, F.; Stella, M.; Goodpaster, J.; Miller III, T. F. *J. Chem. Theory Comput.* **2012**, *8*, 2564–2568.

(18) Lee, S. J. R.; Welborn, M.; Manby, F. R.; Miller III, T. F. *Acc. Chem. Res.* **2019**, *52*, 1359–1368.

(19) Chulhai, D.; Goodpaster, J. *J. Chem. Theory Comput.* **2018**, *14*, 1928–1942.

(20) Bennie, S.; van der Kamp, M.; Pennifold, R.; Stella, M.; Manby, F.; Mulholland, A. *J. Chem. Theory Comput.* **2016**, *12*, 2689–2697.

(21) Zhang, X.; Bennie, S.; van der Kamp, M.; Glowacki, D.; Manby, F. R.; Mulholland, A. J. *R. Soc. Open Sci.* **2018**, *5*, 171390.

(22) Barnes, A.; Kaminski, J.; Borodin, O.; Miller III, T. F. *J. Phys. Chem. C* **2015**, *119*, 3865–3880.

(23) Fornace, M. E.; Lee, J.; Miyamoto, K.; Manby, F. R.; Miller III, T. F. *J. Chem. Theory Comput.* **2015**, *11*, 568–580.

(24) Ding, F.; Manby, F. R.; Miller III, T. F. *J. Chem. Theory Comput.* **2017**, *13*, 1605–1615.

(25) Bakowies, D.; Thiel, W. *J. Phys. Chem.* **1996**, *100*, 10580–10594.

(26) Dapprich, S.; Komáromi, I.; Byun, K.; Morokuma, K.; Frisch, M. J. *J. Mol. Struct.:Theochem* **1999**, *461-462*, 1–21.

(27) Vreven, T.; Byun, K. S.; Komáromi, I.; Dapprich, S.; Montgomery, J. A.; Morokuma, K.; Frisch, M. J. *J. Chem. Theory Comput.* **2006**, *2*, 815–826.

(28) Jiang, H.; Kammler, M.; Ding, F.; Dorenkamp, Y.; Manby, F. R.; Wodtke, A. M.; Miller III, T. F.; Kandratsenka, A.; Bünermann, O. *Science* **2019**, *364*, 379–382.

(29) Lee, S. J.; Miyamoto, K.; Ding, F.; Manby, F. R.; Miller, T. F. *Chem. Phys. Lett.* **2017**, *683*, 375–382.

(30) Ding, F.; Tsuchiya, T.; Manby, F. R.; Miller, T. F. *J. Chem. Theory Comput.* **2017**, *13*, 4216–4227.

(31) Kaminsky, W. *Macromol. Chem. Phys.* **2008**, *209*, 459–466.

(32) Rappé, A. K.; Skiff, W. M.; Casewit, C. J. *Chem. Rev.* **2000**, *100*, 1435–1456.

(33) Coates, G. W. *Chem. Rev.* **2000**, *100*, 1223–1252.

(34) Landis, C. R.; Sillars, D. R.; Batterton, J. M. *J. Am. Chem. Soc.* **2004**, *126*, 8890–8891.

(35) Woo, T. K.; Margl, P. M.; Ziegler, T.; Blöchl, P. E. *Organometallics* **1997**, *16*, 3454–3468.

(36) Margl, P. M.; Deng, L.; Ziegler, T. *Organometallics* **1999**, *18*, 5701–5708.

(37) Lanza, G.; Fragalà, I. L.; Marks, T. J. *J. Am. Chem. Soc.* **2000**, *122*, 12764–12777.

(38) Lanza, G.; Fragalà, I. L.; Marks, T. J. *Organometallics* **2002**, *21*, 5594–5612.

(39) Solans-Monfort, X.; Clot, E.; Copéret, C.; Eisenstein, O. *Organometallics* **2005**, *24*, 1586–1597.

(40) Yang, S.-Y.; Ziegler, T. *Organometallics* **2006**, *25*, 887–900.

(41) Devore, D. D.; Timmers, F. J.; Hasha, D. L.; Rosen, R. K.; Marks, T. J.; Deck, P. A.; Stern, C. L. *Organometallics* **1995**, *14*, 3132–3134.

(42) Woo, T. K.; Margl, P. M.; Lohrenz, J. C. W.; Blöchl, P. E.; Ziegler, T. *J. Am. Chem. Soc.* **1996**, *118*, 13021–13030.

(43) Zhou, Z.; Stevens, J. C.; Klosin, J.; Kümmerle, R.; Qiu, X.; Redwine, D.; Cong, R.; Taha, A.; Mason, J.; Winniford, B.; Chauvel, P.; Montañez, N. *Macromolecules* **2009**, *42*, 2291–2294.

(44) Arriola, D. J.; Carnahan, E. M.; Hustad, P. D.; Kuhlman, R. L.; Wenzel, T. T. *Science* **2006**, *312*, 714–719.

(45) Becke, A. D. *J. Chem. Phys.* **1998**, *98*, 5648–5652.

(46) Lee, C.; Yang, W.; Parr, R. G. *Phys. Rev. B* **1988**, *37*, 785–789.

(47) Vosko, S. H.; Wilk, L.; Nusair, M. *Can. J. Phys.* **2011**, *58*, 1200–1211.

(48) Stephens, P. J.; Devlin, F. J.; Chabalowski, C. F.; Frisch, M. J. *J. Phys. Chem.* **1994**, *98*, 11623–11627.

(49) Ricca, A.; Bauschlicher, C. W. J. *J. Phys. Chem.* **1994**, *98*, 12899–12903.

(50) Musaev, D. G.; Morokuma, K. *J. Phys. Chem.* **1996**, *100*, 6509–6517.

(51) Froese, R. D. J.; Musaev, D. G.; Morokuma, K. *J. Am. Chem. Soc.* **1998**, *120*, 1581–1587.

(52) Froese, R. D. J.; Musaev, D. G.; Morokuma, K. *Organometallics* **1999**, *18*, 373–379.

(53) Perdew, J. P.; Burke, K.; Ernzerhof, M. *Phys. Rev. Lett.* **1996**, *77*, 3865–3868.

(54) Manby, F.; Miller, T.; Bygrave, P.; Ding, F.; Dresselhaus, T.; Batista-Romero, F.; Buccheri, A.; Bungey, C.; Lee, S.; Meli, R.; Miyamoto, K.; Steinmann, C.; Tsuchiya, T.; Welborn, M.; Wiles, T. **2019**, DOI: 10.26434/chemrxiv.7762646.v2.

(55) Vosko, S. H.; Wilk, L.; Nusair, M. *Can. J. Phys.* **1980**, *58*, 1200–1211.

(56) Grimme, S.; Bannwarth, C.; Shushkov, P. *J. Chem. Theory Comput.* **2017**, *13*, 1989–2009.

(57) Berendsen, H. J. C.; van der Spoel, D.; van Drunen, R. *Comput. Phys. Commun.* **1995**, *91*, 43–56.

(58) Jorgensen, W. L.; Tirado-Rives, J. *J. Proc. Natl. Acad. Sci.* **2005**, *102*, 6665–6670.

(59) Caleman, C.; van Maaren, P. J.; Hong, M.; Hub, J. S.; Costa, L. T.; van der Spoel, D. *J. Chem. Theory Comput.* **2012**, *8*, 61–74.

(60) Virtualchemistry, http://virtualchemistry.org/.

(61) Mulliken, R. S. *J. Chem. Phys.* **1955**, *23*, 1833–1840.

(62) Rowley, C. N.; Woo, T. K. *Organometallics* **2011**, *30*, 2071–2074.

(63) Van Gunsteren, W. F.; Berendsen, H. J. C.; Rullmann, J. A. C. *Faraday Discuss Chem Soc.* **1978**, *66*, 58–70.

(64) Hess, B.; Bekker, H.; Berendsen, H. J. C.; Fraaije, J. G. E. M. *J. Comput. Chem.* **1997**, *18*, 1463–1472.

(65) Evans, D. J.; Holian, B. L. *J. Chem. Phys.* **1985**, *83*, 4069–4074.

(66) Parrinello, M.; Rahman, A. *J. Appl. Phys.* **1981**, *52*, 7182–7190.

(67) Lindahl, E.; Hess, B.; van der Spoel, D. *J. Mol. Model.* **2001**, *7*, 306–317.

(68) Malinoski, J.; White, P.; Brookhart, M. *Organometallics* **2003**, *22*, 621–623.

(69) Chen, Y.-X.; Stern, C. L.; Yang, S.; Marks, T. J. *J. Am. Chem. Soc.* **1996**, *118*, 12451–12452.

(70) Grimme, S.; Antony, J.; Ehrlich, S.; Krieg, H. *The Journal of Chemical Physics* **2010**, *132*, 154104.

(71) Collins, R. A.; Russell, A. F.; Mountford, P. *Appl. Petrochem. Res.* **2015**, *5*, 153–171.

(72) Roberts, J. A. S.; Chen, M.-C.; Seyam, A. M.; Li, L.; Zuccaccia, C.; Stahl, N. G.; Marks, T. J. *J. Am. Chem. Soc.* **2007**, *129*, 12713–12733.

(73) Riddlestone, I. M.; Kraft, A.; Schaefer, J.; Krossing, I. *Angew. Chem.* **2018**, *57*, 13982–14024.

Chapter 4

SOLUTION-PHASE CONFORMATIONAL/VIBRATIONAL ANHARMONICITY IN CO-MONOMER INCORPORATION POLYOLEFIN CATALYSIS

ABSTRACT

The prediction of co-monomer incorporation statistics in polyolefin catalysis necessitates an accurate calculation of free energies corresponding to monomer binding and insertion, often requiring sub–kcal/mol resolution to resolve experimental free energies. Batch reactor experiments are used to probe incorporation statistics of ethene and larger α-olefins for three constrained geometry complexes (CGC) which are employed as model systems. Herein, over 6 ns of quantum mechanics / molecular mechanics (QM/MM) molecular dynamics is performed in combination with the zero-temperature string method to characterize the solution-phase insertion barrier and to analyze the contributions from conformational and vibrational anharmonicity arising both in vacuum and in solution. Conformational sampling in the gas–phase results in 0-2 kcal/mol corrections to the insertion barrier which are on the same scale necessary to resolve experimental free energies, and this correction is further magnified by the inclusion of explicit solvation. Anharmonic conformational sampling in the solution-phase is a crucial energy contribution missing from static DFT calculations and implicit solvation models, and its accurate calculation is a key step towards the quantitative prediction of co-monomer incorporation statistics.

Introduction

Polyolefin manufacturing is a major chemical enterprise, and the resulting polymer products are ubiquitous as materials [1, 2]. The inclusion of co-monomers to the polymerization process leads to useful polyolefin materials [3]. Predicting experimental polymerization parameters such as co-monomer incorporation ratios from *ab initio* calculations would accelerate catalyst development and promote rational ligand design [4]. Hence, the comprehensive treatment of contributions to reaction free energies is essential for simulating molecular phenomena accurately. Leveraging the Curtin-Hammett principle, the approach discussed here computes the free energy contributions of conformational sampling and the perturbation of the catalyst active site by colliding solvent molecules, which are necessary for more accurate energetics [5–7]. Although the quantification of conformational and anharmonic vibrational contributions to free energies has precedence [8–13], to our knowledge no attempt has been made to quantify these contributions by directly sampling restrained solution-phase trajectories of organometallic catalysts. In addition, the QM/MM MD calculations employed do not assume an approximate anharmonic form for molecular vibrations and instead directly sample anharmonic vibrational motion in the solution-phase. Such an approach entails the need for sufficient simulation time; for the results presented here, we have obtained > 6 ns of fully solvated MD trajectory data along with a similar length of isolated catalyst MD trajectory sampling.

Polymerization by Group IV catalysts has three regimes: initiation, propagation, and termination. The initiation step forms the active catalyst, followed by sequential binding and insertion of monomers during the propagation sequence leading to a growing polymer chain, and finally termination ends the polymerization by side reactions such as β-hydride elimination and chain transfer [14]. During propagation, the binding of the monomers with early transition metal polyolefin catalysts is often reversible, a key requirement necessary for application of the Curtin-Hammett principle to the study of co-monomer incorporation. The monomer binding step is followed by the rate-limiting insertion barrier [15–17]. Tuning the relative energies of the binding and propagation steps is achievable by electronic and steric tuning of the catalyst [18–20] and is a proxy for controlling incorporation kinetics, with the caveat that this principle does not necessarily apply to catalyst systems with a suspected change in rate-limiting step [21]. Understanding conformational and solvation free energy contributions to both insertion and binding across multiple catalyst families is critical for predicting co-monomer incorporation statistics.

Previous computational studies of the polyolefin mechanism have largely focused on a single-step process such as catalyst–counterion binding and activation [22–24] or the insertion step [25–27]. The free energy calculations typically rely on harmonic approximations, where the effect of solvation is employed by using implicit models. Studies that have used explicit solvation to interrogate elementary steps in polyolefin catalysis are limited to the counterion binding process [28]. Anharmonic conformational sampling involving explicit solvation models (e.g., QM/MM[29, 30]) improve upon the harmonic approximation and are more often applied to enzymatic systems [31, 32] than to organometallic systems, even though anharmonic corrections to the harmonic treatment of free energies are necessary for quantitative predictions of reaction rates [33, 34].

Ideal homogeneous catalysts for olefin polymerization have the following features: stability at high temperatures ($T > 120^{\circ}$C), high catalyst activity, narrow molecular weight distribution of polymer, and competence at co-polymerization at high temperatures [35]. Possessing these features, the constrained geometry complex (CGC) catalysts [36] are industrially used as polyolefin catalysts and are the focus of this study (Figure 4.1). CGC catalysts typically contain Group IV metals, and the Ti–metallated catalyst is the subject of this study. Compared to traditional Ziegler-Natta catalysts, CGC systems offer higher reactivity towards co-monomers and narrower PDI [37].

All of the CGC structures discussed herein include a Ti metal center, an *n*-propyl group growing chain, and a ligand scaffold which differs only by the substitution at the cyclopentadienyl moiety (Figure 4.1). CGC-A is the prototypical CGC catalyst [38], with methyl groups substituting the cyclopentadienyl ligand. CGC-B contains an extended aromatic system, with fewer steric constraints near the monomer binding site. The catalyst is known to be highly effective at styrene incorporation [39]. Lastly, CGC-C contains a modified aromatic system and a conformationally flexible electron-donating pyrrolidine side chain. The additional 3-amino substitution on CGC-C offers higher catalytic activity and co-polymer molecular weights compared to CGC-A [40].

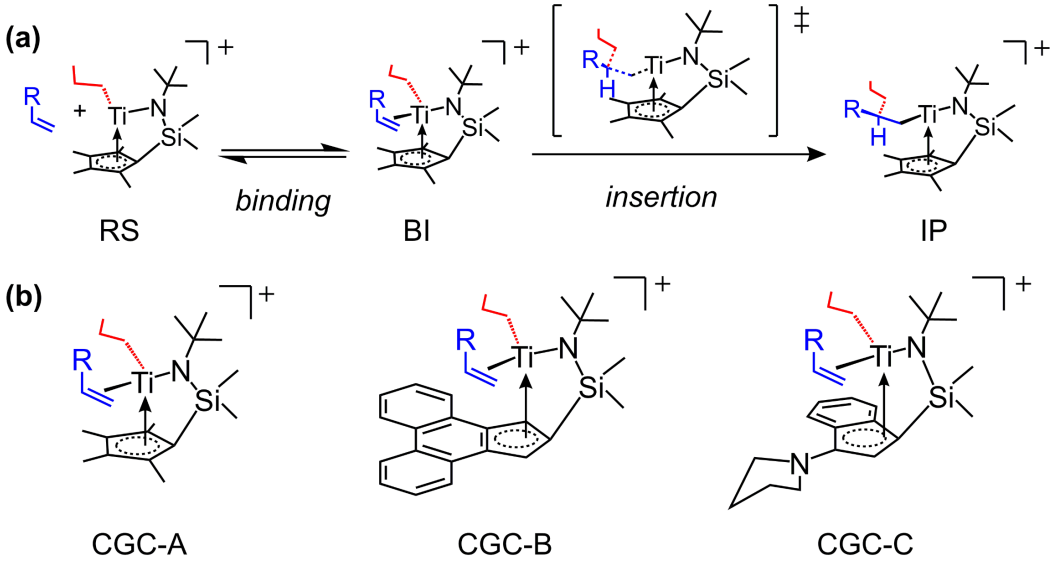

Figure 4.1: Propagation mechanism and polyolefin catalysts. (a) Propagation steps for olefin polymerization, consisting of a monomer (highlighted blue) binding to the resting state (RS) to form the bound intermediate (BI). Subsequent migratory insertion of the olefin into the growing chain (*n*-propyl group highlighted in red) results in the insertion product (IP). (b) Three constrained geometry complex (CGC) catalysts are employed, which can react with one of four α–olefins of increasing chain length: ethene (R = H), propene (R = Me), butene (R = Et), hexene (R = *n*-Bu).

Experimental-Computational Connection

The main quantity of interest is the co-monomer incorporation ratio $r = p_c/(1-p_c)$, which is defined by the molar proportion of co-monomer incorporated into the polymer chain (p_c) by the proportion of incorporated ethene molecules ($p_e = 1-p_c$). To connect this quantity to calculations, we will discuss the kinetic model and approximations necessary to predict r.

The polymerization mechanism involving incorporation of α–olefin co-monomers is shown in Figure 4.2. In the center are the bound intermediates of the ethene monomer and longer chain co-monomer, which can interconvert via the monomer binding equilibrium. The monomer interconversion equilibrium has an associated free energy ΔG_{ce}, which corresponds to the difference in binding energies ($\Delta G_{ce} = \Delta G_e - \Delta G_c$). From the bound intermediate, the monomer inserts into the growing chain (in this study, *n*-propyl group) subject to the ethene insertion barrier height $\Delta G_e^{\ddagger}$ or a co-monomer insertion barrier height $\Delta G_c^{\ddagger}$.

The first approximation applied to predicting r is limiting the free energy calculation to a single incorporation step and extrapolating the result to incorporation throughout polymerization. Next, the Curtin-Hammett principle [41] is applied to the mechanism, given that insertion is the typical rate-determining step for the Group IV catalysts [15, 16]. The relative reaction rate between co-monomer and ethene incorporation is directly predicted by the free energy difference in insertion transition states $\Delta\Delta G^{\ddagger}$ (Eqn. 1). The quantity can be decomposed into two quantities, the monomer interconversion energy ΔG_{ce} and the difference in insertion barriers $(\Delta G_c^{\ddagger} - \Delta G_e^{\ddagger})$.

$$\Delta\Delta G^{\ddagger} = \Delta G_c^{\ddagger} - \Delta G_e^{\ddagger} - \Delta G_{ce} \tag{4.1}$$

Batch reactor experiments offer experimental data on the incorporation of octene with ethene. The incorporation ratios r are converted to free energy differences $\Delta\Delta G^{\ddagger}$ (see Computational Protocol) taking into account the non-equal concentrations of ethene and octene used in experiment (octene/ethene ratio is 2.32). The study involves shorter chain co-monomers (propene, butene, hexene) for computational tractability and to elucidate the effect of monomer chain length. We will present this experimental data to compare the magnitude of the energy differences between catalysts and the energy corrections seen from solution-phase conformational sampling. We emphasize that consistency between the experimental and computational $\Delta\Delta G^{\ddagger}$ is yet to be achieved, but instead will demonstrate that the contributions to $\Delta\Delta G^{\ddagger}$ from solution-phase conformational sampling are significant relative to the small energy differences seen between catalysts and thus can affect catalyst rank ordering.

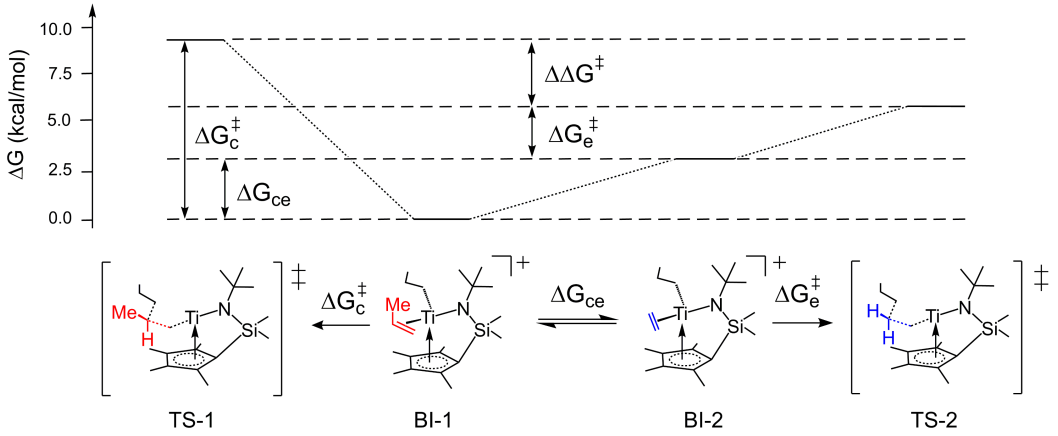

Figure 4.2: Free energy profile displaying two competing incorporation pathways of ethene (highlighted blue) and α-olefin co-monomer propene (highlighted red) incorporation (unbound monomers not shown). The reversible monomer interconversion equilibrium between the co-monomer and ethene bound intermediates BI-1 and BI-2, respectively, are mediated by the resting state species (not shown). Insertion of the co-monomer or ethene into the *n*-propyl group passes through the transition states TS-1 or TS-2, respectively. Combining the energy difference between insertion barrier heights and the free energy of monomer interconversion yields the key quantity for incorporation selectivity $\Delta\Delta G^{\ddagger} = \Delta G_c^{\ddagger} - \Delta G_e^{\ddagger} - \Delta G_{ce}$.

Methods

Computational Protocol

DFT energy and force calculations are carried out with the Entos *qcore* software [42]. The functional B97-3c was chosen for its favorable compromise of speed and accuracy [43]. All optimized structures are determined to be stationary points by harmonic frequency analysis. The ideal gas approximation was used for the calculation of harmonic Gibbs free energies on the stationary point structures. Implicit solvation corrections were obtained with the ORCA software package [44] using the SMD model for *n*-hexane. Harmonic frequency analysis of optimized structures is used to assess the energy associated from a harmonic treatment of the free energy surface, while molecular dynamics is used to quantify the additional contributions of anharmonic conformational sampling and the effect of explicit solvation. In this study, MD is applied to the calculation of insertion barrier free energies in CGC-catalyzed olefin incorporation.

The following protocol details how to obtain the structures and restraint values necessary for the free energy calculation. Note that the structures employed in

this study are the cationic species, excluding the counterion. First, the bound intermediate and insertion transition state structure were optimized for the isolated catalyst, and the orientation of the monomer to the catalyst was verified to be consistent with the other systems. Interpolation was applied to the bound and TS structures to obtain a total of 8 structures (including endpoints) as a string smoothly varying from bound to TS. This discretization of the insertion barrier as a sequence of 8 images is then optimized by the zero–temperature string method to a minimum energy pathway (i.e., zero-temperature string, ZTS) [45–47]. Literature protocol [48] was followed for an in-house implementation of the algorithms. Convergence of the ZTS is defined as the point in which the largest energy change per string image falls below the threshold of 10^{-4} hartree.

The free energy calculation requires the definition of a collective variable that is involved in the spatial dimensions of the reaction. Here, the coordination number (CN) was chosen as collective variable for interrogating the insertion barrier, due to its precedence in prior free energy studies of monomer insertion [49] and free energy calculations in general [50, 51]. The coordination number for a two-atom pair ranges monotonically from 0 to 1 (unbound to bound), and is additive with respect to the number of atoms ($k = 5$ atoms coordinated closely to a central atom implies $CN \sim 5$). A CN to some central atom is defined by measuring the coordination of k atoms to some central atom, with defined parameters n, m, r (see Equation 2) that define the spatial dimensions of CN, and free variable d_k which is the distance between in the k^{th} atom and the central atom.

$$CN = \sum_k \frac{1 - \left(\frac{d_k}{r}\right)^n}{1 - \left(\frac{d_k}{r}\right)^m} \tag{4.2}$$

For this study, two coordination numbers are employed: $CN1$ quantifies the binding of the olefin to the catalyst, and the $CN2$ tracks insertion of the monomer into the growing chain. The quantity $CN1$ is defined by the coordination of the two alkene carbons to the central atom Ti, and $CN2$ by the coordination of the two alkene carbons to the carbon on the n-propyl group that is adjacent to the metal. (See Supporting Information for specific parameterization.) Each structure from the optimized string is assigned a corresponding collective variable ($CN1$, $CN2$), and these values are used as the equilibrium value for coordinate number restraints.

To perform the free energy calculation for a given catalyst/monomer system, MD trajectories are run subject to restraining the collective variables ($CN1$, $CN2$) at val-

ues along the minimum energy pathways (calculated by ZTS) in collective variable space. Eight images along the minimum energy pathway in collective variable space are used for each catalyst/monomer system, equivalent to eight MD trajectories per system (with varying CN-restraints along the minimum energy pathway) (12 systems total). (For CGC-C, an additional trajectory was necessary for a smoother free energy gradient curve.) The values ($CN1$, $CN2$) are recorded from the trajectory and then used to compute the free energy gradient at ($CN1$, $CN2$), by scaling the average displacement of the system in collective variable space by the restraint spring constant [48]. Integration of the gradients along the string in ($CN1$, $CN2$) space yields the insertion barrier free energy (explained in more detail in the Results section).

For fully solvated MD trajectories, QM/MM (quantum mechanics/molecular mechanics) simulations are carried out with the additive, electrostatic coupling scheme, in which MM point charges polarize the QM region [52]. Other non-bonding interactions between the MM and QM regions are computed using the Lennard-Jones potential with parameterization provided in the Supporting Information. The QM region is defined to be the catalyst/monomer complex and the MM region is the hexane solvent environment.

Each QM/MM production run has a simulation time of at least 65 ps. The velocity verlet integrator [53] is used with a 1.5 fs time step. The Andersen thermostat [54] is utilized with a coupling time of 1.5 fs and temperature of 393 K, corresponding to the temperature from the obtained experimental data. The NVT ensemble is employed, with a cubic simulation cell sidelength of 3.522 nm. Coordination number restraints are applied with force constants of 1.5 a.u. A cutoff of 1.5 nm is used for electrostatic and vdW interactions. The Coulomb energy for the point charges are calculated with Ewald summation with self-interaction correction. There are about 155 solvent molecules present in each simulation, and the C–H bonds in the hexane solvent are constrained. We emphasize that with 8 trajectories per catalyst/monomer system (12 systems total) (excluding the interpolated images), we obtain 96 solution-phase DFT trajectories which add up to over 6 ns of solution-phase MD sampling data.

Experimental free energy differences are computed from experimentally observed ratios of ethene and octene monomers in the polymer produced by the batch reactor experiments under the assumption that ethene and octene insertions into the polymer are statistically independent. Ethene and octene concentrations in the reaction medium are computed using the methodology by Chao and Seader [55]. The free

energy differences $\Delta\Delta G^{\ddagger}$ in Table 4.1 are derived from the experimental parameters, which are described in the Supporting Information, Details of Polymerization Reactor Runs section.

Experimental

Batch Reactor Polymerization Procedure

The batch reactor polymerizations were conducted in a 2-L Parr™ batch reactor. The reactor is heated by an electrical heating mantle, and is cooled by an internal serpentine cooling coil containing cooling water. Both the reactor and the heating/cooling system are controlled and monitored by a Camile™ TG process computer. The bottom of the reactor is fitted with a dump valve, which empties the reactor contents into a stainless-steel dump pot, which is prefilled with a catalyst kill solution (typically 5 mL of an Irgafos / Irganox / toluene mixture) (refer to the Supporting Information for reagent details). The dump pot is vented to a 114-L blow-down tank, with both the pot and the tank purged with nitrogen. All solvents used for polymerization or catalyst makeup are run through solvent purification columns to remove any impurities that may affect polymerization. The 1-octene and Isopar E were passed through two columns, the first containing activated A2 alumina, the second containing activated Q5 reactant. The ethene was passed through two columns, the first containing A204 alumina and 4Å molecular sieves, the second containing Q5 reactant. The N_2, used for transfers, was passed through a single column containing A204 alumna, 4Å molecular sieves and Q5. The reactor is loaded first from the shot tank that contains Isopar E solvent and/or 1-octene, depending on desired reactor loading. The shot tank is filled to the load set points by use of a lab scale to which the shot tank is mounted. After liquid feed addition, the reactor is heated up to the polymerization temperature set point. If ethene is used, it is added to the reactor when at reaction temperature to maintain reaction pressure set point. Ethene addition amounts are monitored by a micro-motion flow meter. The catalyst and activators were mixed with the appropriate amount of purified toluene to achieve a solution of the desired molarity. The catalyst and activators were handled in an inert glove box, drawn into a syringe and pressure transferred into the catalyst shot tank. This was followed by three rinses of toluene, 5-mL each. Immediately after catalyst addition the run timer began. If ethene was used, it was then added by the Camile to maintain the reaction pressure set point in the reactor. These polymerizations were run for 10 min., then the agitator was stopped and the bottom dump valve was opened to empty reactor contents into the dump pot. The dump pot contents were poured into trays placed

in a lab hood where the solvent was evaporated off overnight. The trays containing the remaining polymer were then transferred to a vacuum oven, where they were heated up to 140 °C under vacuum to remove any remaining solvent. After the trays cooled to ambient temperature, the polymers were weighed for yield/efficiencies, and submitted for polymer testing.

HT-GPC Analysis with IR Detection of Octene Incorporation

High-temperature GPC analysis was performed using a Dow Robot Assisted Delivery (RAD) system equipped with a PolymerChar infrared detector (IR5) and Agilent PLgel Mixed A columns. Decane (10 µL) was added to each sample for use as an internal flow marker. Samples were first diluted in 1,2,4-trichlorobenzene (TCB) stabilized with 300 ppm of butylated hydroxytoluene (BHT) to a concentration of 10 mg/mL and dissolved by stirring at 160 °C for 120 minutes. Prior to injection samples were further diluted with TCB stabilized with BHT to a concentration of 2 mg/mL. Samples (250 µL) were eluted through one PL-gel 20 µm (50 x 7.5 mm) guard column followed by two PL-gel 20 µm (300 x 7.5 mm) Mixed-A columns maintained at 160 °C with TCB stabilized with BHT at a flowrate of 1.0 mL/min. The total run time was 24 minutes. To calibrate for molecular weight Agilent EasiCal polystyrene standards (PS-1 and PS-2) were diluted with 1.5 mL of TCB stabilized with BHT and dissolved by stirring at 160 °C for 15 minutes. The PS standards were injected into the system without further dilution to create a 3rd-order MW calibration curve with apparent units adjusted to homo-polyethylene (PE) using known Mark-Houwink coefficients for PS and PE. Octene incorporation was determined by use of a linear calibration developed by analyzing copolymers of known compositions.

Results and Discussion

Experimental Incorporation Ratios

The calculation of $\Delta\Delta G^{\ddagger}$ of co-monomer incorporation offers a challenge to computational techniques. The experimental incorporation ratios obtained from batch reactor experiments for octene incorporation with ethene are converted to free energies $\Delta\Delta G^{\ddagger}$, which are in the range of 0–2 kcal/mol (Table 4.1). At these energy scales, sub–kcal/mol resolution of the free energies is necessary to distinguish $\Delta\Delta G^{\ddagger}$ between catalyst systems. The CGC catalysts employed are structurally similar and differ only by modifications of the cyclopentadienyl substitution, explaining the small observed differences in $\Delta\Delta G^{\ddagger}$. Complicating the calculation of anharmonic

Table 4.1: The proportion of octene incorporation p_c and incorporation ratio r for octene incorporation with ethene is shown for the CGC catalysts CGC-A and CGC-C. The corresponding insertion TS free energy difference $\Delta\Delta G^{\ddagger}$ is derived from the experimental incorporation ratio r (see Supporting Information for derivation). Small energy scales are seen in $\Delta\Delta G^{\ddagger}$, which imposes strict accuracy requirements on the free energy calculation. The experimental temperatures is 393 K, which is also the temperature used for the free energy calculation.

System	p_c (avg.)	r_c	$\Delta\Delta G^{\ddagger}$
CGC-A	0.26	0.17	1.4
CGC-C	0.13	0.083	2.0

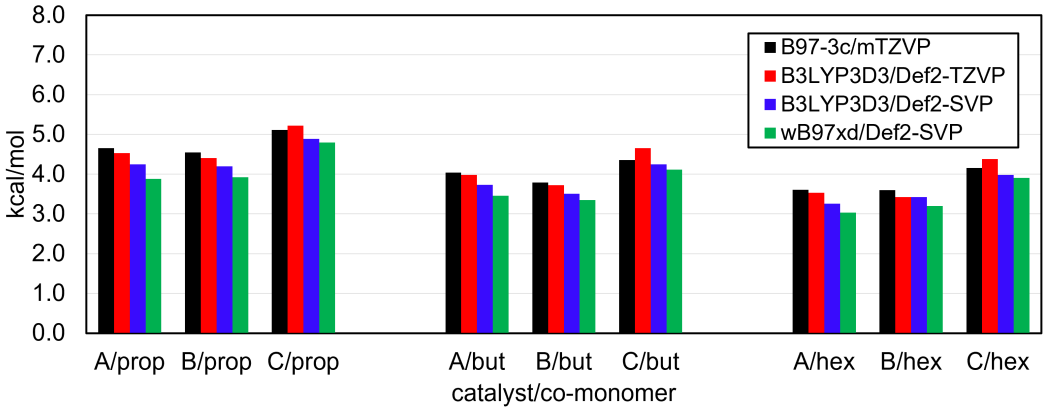

Figure 4.3: The insertion transition state energy difference ($\Delta\Delta G^{\ddagger}$) was computed using the harmonic approximation with the implicit solvation correction added, and is equivalent to adding the energies from monomer interconversion and the barrier height differences between the co-monomer and ethene. The spread of values across methods is small, and a change in DFT method (functional or basis set) gives a consistent answer across methods.

free energy contributions is the necessity of computing four independent free energies which comprise $\Delta\Delta G^{\ddagger}$, necessitating low systematic and statistical error in the free energy calculation. As shown in Figure 4.3, employing single-point DFT calculations leads to a consistent overestimation of $\Delta\Delta G^{\ddagger}$.

Benchmarking Computational Protocol

In this section, we confirm the validity of the structures used for the harmonic calculations, present the reaction minimum energy pathways obtained from the zero-temperature string (ZTS) method, and validate the data obtained from molecular dynamics sampling along the minimum energy pathways.

Conformational Consistency

Two orientations of the olefin monomer are explored for a fixed stereoconfiguration of the ligand, in which the olefin side-chain is pointed either towards or away from the cyclopentadienyl ring. The two orientations of the olefin are nearly isoenergetic, leading to the value of $\Delta\Delta G^{\ddagger}$ differing by less than 1 kcal/mol between the two conformers (see Supporting Information, Table 1). For computational efficiency in the MD runs and free energy calculations, a single conformer was selected in which the alkyl substitution on propene, butene, or hexene is pointed away from the cyclopentadienyl ring on the catalyst.

Consistency of conformation is demonstrated across the dimensions of catalyst and the monomer. In Figure 4.4, the structures were overlapped for structures with bound monomers ethene, propene, butene, and hexene for a fixed choice of catalyst. The monomer has consistent orientation of binding to the catalyst, and functional groups are in a conformation consistent with the other systems. The same analysis was performed for a fixed choice of monomer (see Supporting Information), and the structures involving catalyst CGC-A, CGC-B, and CGC-C were overlapped. As in the comparison of catalysts, the overlap of structures for a fixed choice of monomer further demonstrate conformational consistency.

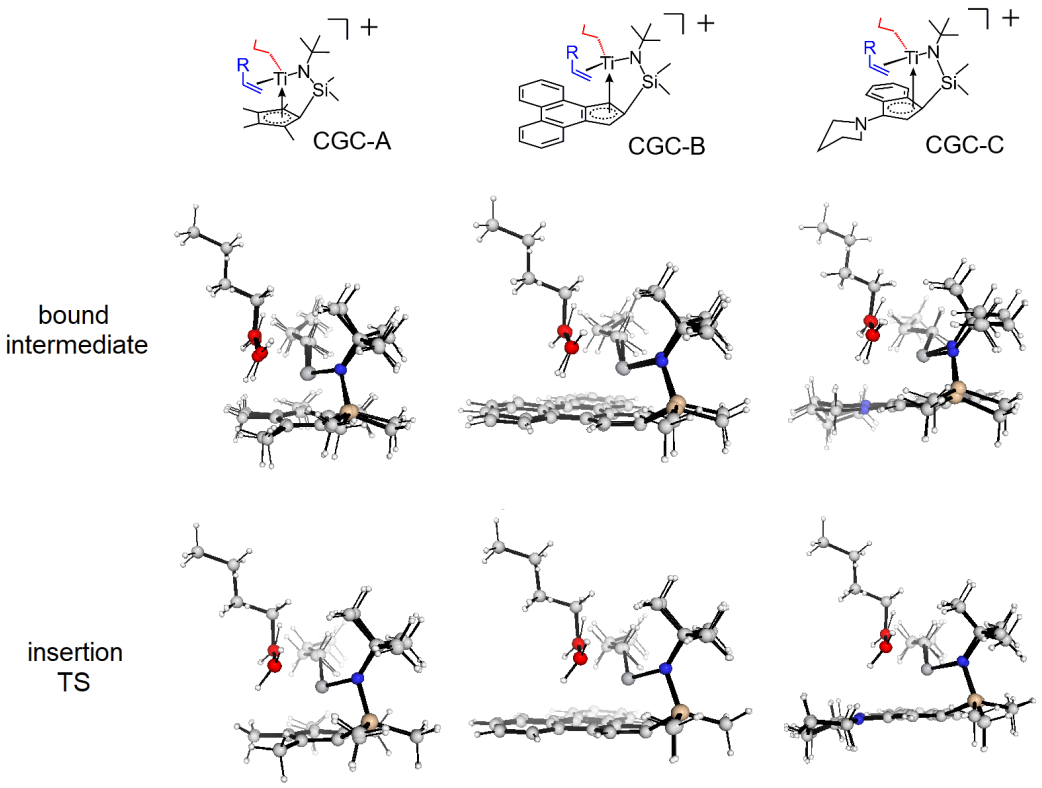

Figure 4.4: Structural overlap of the bound intermediates and insertion transition states. For a given CGC catalyst system, the structures bound with ethene, propene, butene, and hexene are overlayed for comparison, and the two alkene carbon atoms on the monomer are highlighted red for clarity. The orientation of the monomer, along with conformationally flexible side-chains such as the *n*-propyl group (positioned in the center back in each overlay), is consistent across all systems.

Zero-Temperature String Optimization

The insertion barrier is discretized into 8 structures, and the structures are optimized by ZTS method to obtain a minimum energy pathway for a given catalyst/monomer system. In Figure 4.5, the structures along the minimum energy pathways are plotted as points in collective variable space ($CN1$, $CN2$), and the corresponding potential surface of the insertion barrier is plotted as a function of the insertion collective variable $CN2$. The variable $CN2$ is considered the dominant collective variable for the insertion step, as noted by the small scales associated with $CN1$ (which captures degree of monomer–Ti binding). As expected from structural overlap comparisons, the minimum energy pathways across catalyst systems and monomers are consistent, with only significant variation seen in the minimum

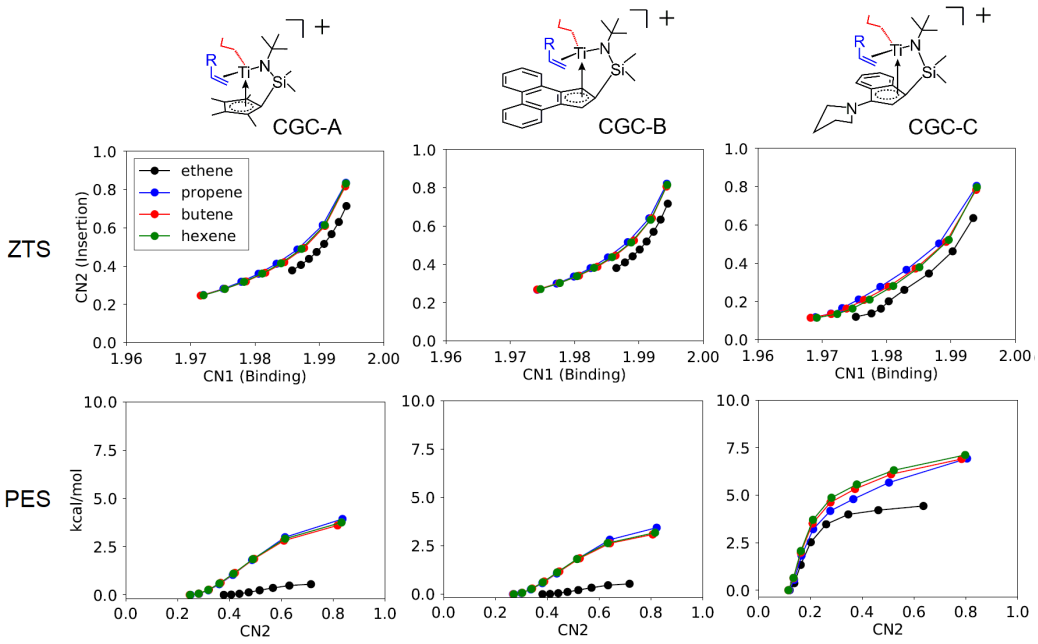

Figure 4.5: Minimum energy pathway results (computed by ZTS method) are shown for each catalyst/monomer system, along with the corresponding potential energy surface (PES) along the string. Note the much reduced scales of the CN1 (x-axis) dimension, indicating that the collective variable CN2 is the dominant axis of the insertion string. Ethene has a lower potential barrier in comparison to the mono-substituted olefins, and CGC-C insertion barriers are higher than those of CGC-A and CGC-B.

energy pathways (and corresponding potential energy surfaces) of the ethene-bound and CGC-C structures. As seen in the potential energy profiles, ethene insertion is significantly more facile due to the lack of sterically encumbering monosubstitution, while CGC-C exhibits hindered insertion across monomers which correlates with conformational accommodation of the ligand scaffold to the insertion of monomer.

Free Energy Calculation

The insertion barrier free energy is computed along the minimum energy pathway following literature protocol [48]. A structure with position coordinates $x(t)$ gives a specific value of the collective variable $\theta_j(x(t))$. For the molecular dynamics, restraints are placed for each j^{th} coordination number at $CN = z_j$, and have harmonic spring constants of k (units kcal/mol, since CN is unitless). Over the course of a trajectory, the average displacement $z_j - \theta_j(x(t))$ for each collective variable θ_j will

settle into the ensemble average of the displacement. With enough sampling time and large restraint spring constant k, scaling the time–average displacement by the value of the restraint spring constant gives an estimation of the free energy gradient at the restraint values ($CN1$, $CN2$), which converges to the true free energy gradient. The corresponding free energy profile is obtained by integration of the free energy gradients over the minimum energy pathway in collective variable space.

$$\frac{\delta F_k(z)}{\delta z_j} = k \int (z_j - \theta_j(x))\rho_{k,z}(x)dx \tag{4.3}$$

$$= \lim_{T\to\infty} \frac{k}{T} \int_0^T (z_j - \theta_j(x(t)))dt \tag{4.4}$$

For each structure along the minimum energy pathway, a molecular dynamics trajectory is run with harmonic springs associated with the $CN1$ and $CN2$ collective variables. For a given trajectory and catalyst/monomer system, a histogram of the collective variable $CN2$ (insertion) is taken (Figure 4.6). The trajectories range from the bound intermediate on the left to the insertion TS on the right. Distributions of the trajectories are normal and smoothly overlap the span of $CN2$ values between the bound intermediate and insertion transition state, which support their use for the insertion barrier free energy calculation. However, the highly Gaussian nature of these distributions suggests that fewer sampling windows can employed with a weaker harmonic restraint.

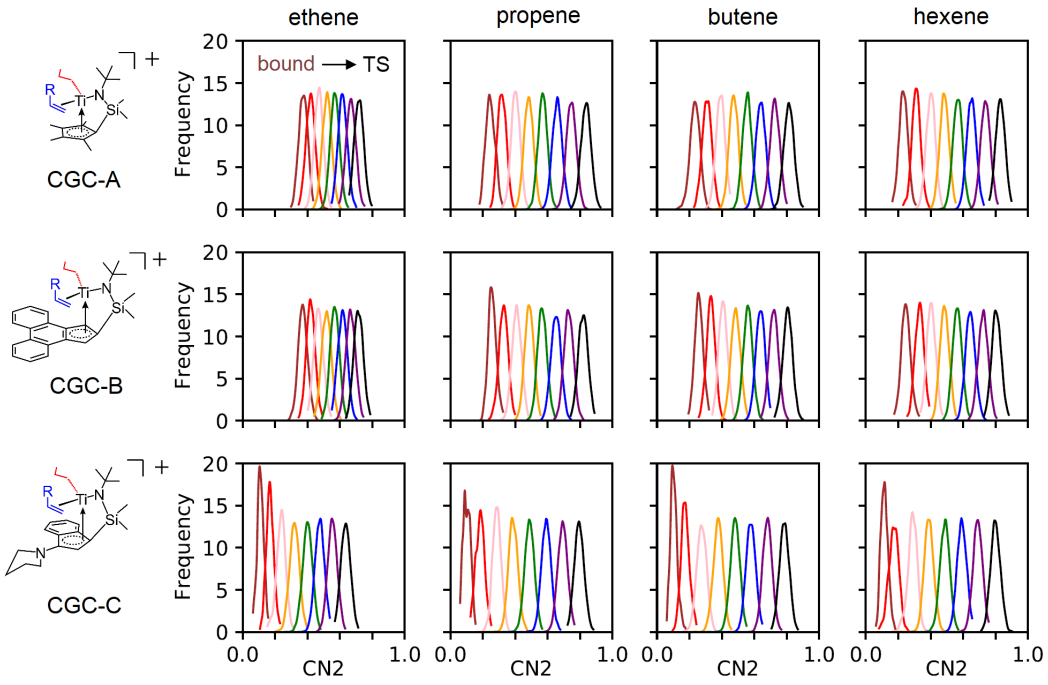

Figure 4.6: For each catalyst/monomer system, histograms are plotted for each solution-phase trajectory window with respect to the CN2 insertion collective variable. The normal distribution of the trajectory histograms supports the quality of the computed trajectories.

Using Equation 4, the gradient of the free energy with respect to ($CN1$, $CN2$) was obtained from each trajectory. The free energy gradients along $CN2$ are plotted in Figure 4.7 with the corresponding free energy obtained by numerical integration of the gradients along the minimum energy pathway. Stochasticity associated from thermal conformational sampling manifests as local jumps in the free energy gradient, but overall the gradients have consistently shaped topologies. The trends seen in the free energy profiles parallel those of the potential energy profiles: ethene-bound pathways have smaller barriers than those involving the mono-substituted monomers, and insertion barriers involving CGC-C are noticeably higher than for the other CGC catalysts. However, note that the insertion barrier heights need to be taken into account with the monomer binding energies for the prediction of incorporation ratios.

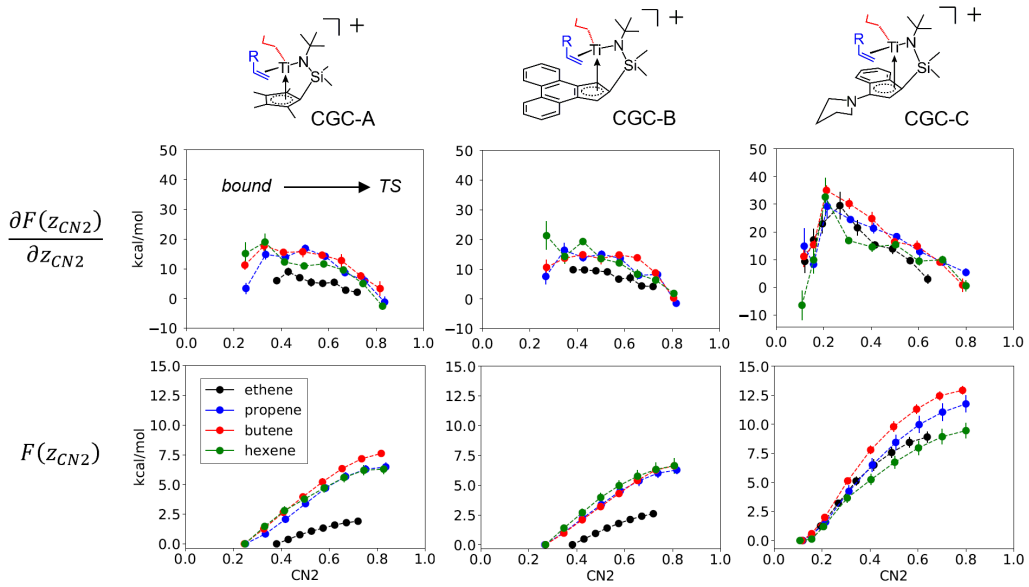

Figure 4.7: The solution-phase free energy gradients $\partial F(z_{CN2})/\partial z_{CN2}$ derived from each trajectory window and the corresponding free energy $F(z_{CN2})$ are plotted as a function of the CN2 collective variable.

Catalytic and Computational Insights

In this section, the chemical implications for the inclusion of thermal conformational sampling and solvation contributions are elucidated. The magnitude of anharmonic contributions from conformational sampling and explicit solvation are highlighted to emphasize the necessity of including small corrections that are large enough to affect the catalyst rank ordering of the CGC-A and CGC-C systems. First, we show that the anharmonic corrections stemming from conformational sampling can be large in comparison to the harmonic thermal correction. Next, we illustrate the necessity of employing QM/MM MD to model solvation effects, as implicit solvation techniques fail to model reactivity differences across catalyst systems. Finally, the solvation corrections on both the monomer interconversion equilibrium and migratory insertion steps are large in energy scale relative to the experimental $\Delta\Delta G^{\ddagger}$, supporting the utility of modelling solvation effects in co-monomer incorporation catalysis.

Non-Harmonic Conformational Effects

Insertion BHDs obtained by both anharmonic MD and harmonic frequency analysis are compared to assess the scale of conformational anharmonicity in the olefin

insertion barrier, relative to the harmonic correction of the electronic barrier. The harmonic correction is defined as the difference between the Gibbs free energy and the electronic energy (Equation 5), and the anharmonic correction is taken to be the difference of the free energies obtained from MD of the isolated catalyst and the harmonic approximation (Equation 6).

$$\Delta\Delta G^{\ddagger}_{\text{harmonic corr.}} = \Delta\Delta G^{\ddagger}_{\text{harmonic}} - \Delta\Delta E^{\ddagger} \tag{4.5}$$

$$\Delta\Delta G^{\ddagger}_{\text{anharmonic corr.}} = \Delta\Delta G^{\ddagger}_{\text{isolated catalyst MD}} - \Delta\Delta G^{\ddagger}_{\text{harmonic}} \tag{4.6}$$

Both corrections are plotted for each catalyst/monomer pair in Figure 4.8. Harmonic corrections are on the order of about 1-3 kcal/mol, and have consistent rank ordering across systems (the zero-point energy contribution to the insertion BHD harmonic correction is shown in the Supporting Information). The corrections from anharmonic MD of the isolated catalyst are smaller in scale (0-2 kcal/mol), yet are significant for sub-kcal/mol energy resolutions required to predict co-monomer incorporation ratios. Molecular dynamics allows for the accounting of the conformational entropy of the bound intermediate, which can be represented by an ensemble of ground-state conformer microstates. By including the conformational entropy associated with thermal conformer sampling, the anharmonic free energy corrections tend to be negative, as seen in Figure 4.8. As expected for larger, more flexible systems, the BHDs corresponding to catalyst CGC-C with butene and hexene co-monomers show greater corrections to the free energy stemming from conformational sampling of the conformationally flexible structures.

Explicit and Implicit Solvation

Sampling solution-phase trajectories offers an additional free energy correction beyond isolated catalyst conformational sampling, denoted here as the explicit solvation correction. As defined in Equation 7, explicit solvation effects can be considered as the correction corresponding to the solvation bias on the thermal conformational sampling of the catalyst. The results from explicit solvation are contrasted to those obtained from the implicit solvation correction (via SMD model[56]), defined in Equation 8 as the electronic energy correction associated with including a continuum solvation model.

$$\Delta\Delta G^{\ddagger}_{\text{explicit solv. corr.}} = \Delta\Delta G^{\ddagger}_{\text{QM/MM MD}} - \Delta\Delta G^{\ddagger}_{\text{isolated catalyst MD}} \tag{4.7}$$

$$\Delta\Delta E^{\ddagger}_{\text{implicit solv. corr.}} = \Delta\Delta E^{\ddagger}_{\text{implicit solv.}} - \Delta\Delta E^{\ddagger} \tag{4.8}$$

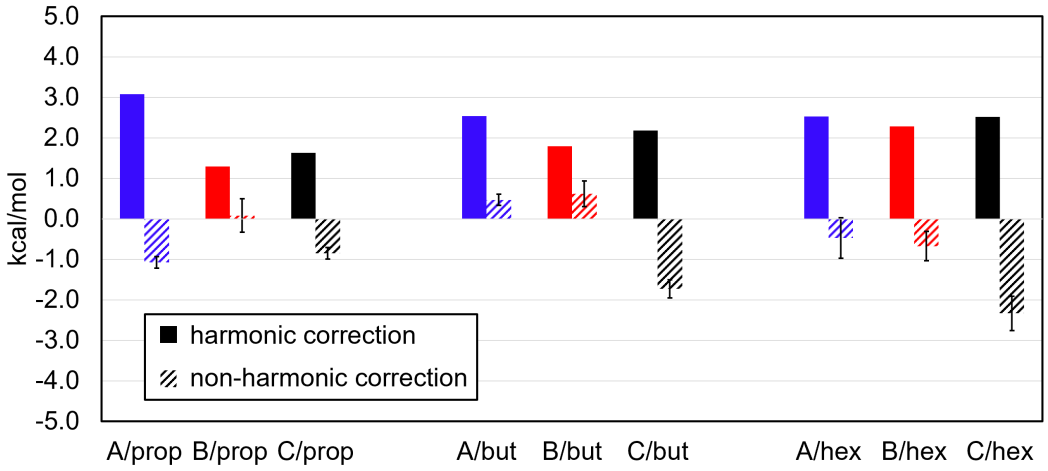

Figure 4.8: The harmonic correction and anharmonic correction on insertion BHDs are compared for each of the catalyst/monomer systems. The harmonic correction consists of the thermal contribution to the free energy difference from the ideal gas approximation (Equation 5), and the anharmonic correction reflects the contribution of conformational sampling of the isolated catalyst to the free energy difference (Equation 6). Anharmonic contributions from conformational sampling are on the kcal/mol scale and typically negative. The conformationally flexible CGC-C system with bound propene and hexene show significantly greater anharmonicity.

In Figure 4.9(a), the isolated catalyst anharmonic correction is compared to the explicit solvation correction, which was obtained by taking the difference of the solution-phase and isolated catalyst MD-obtained insertion BHDs. The points tend to be clustered along the diagonals, implying that the explicit solvation correction generally amplifies the anharmonicity seen with the isolated catalyst. In addition, both corrections tend to reduce the computed insertion BHD, as most of the points are located in the lower-left quadrant of the plot.

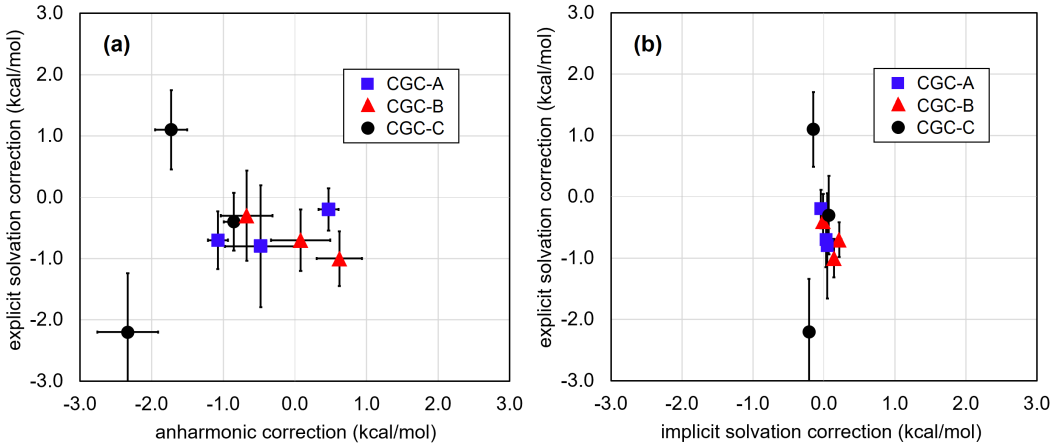

Figure 4.9: Free energy contributions from anharmonic and solvation effects. (a) The isolated catalyst anharmonic correction to the insertion barrier height differences (Equation 6) is compared to the correction from explicit solvation effects (Equation 7). Explicit solvation tends to amplify anharmonicity seen with the isolated catalyst. (b) The implicit solvation correction (Equation 8) is plotted with the explicit solvation correction for insertion BHDs (Equation 7). Implicit effects are much smaller relative to explicit effects obtained by solution-phase conformational sampling.

Solvation corrections from MD are compared to those obtained by implicit solvation. The implicit solvation correction quantifies the contribution of implicit solvation to electronic energies. Solvation effects from both explicit and implicit methods are compared in Figure 4.9(b). Here, implicit solvation corrections to insertion BHDs are negligible in comparison to the explicit solvation corrections. While in Figure 4.9(a) the explicit solvation correction appears amplified by conformational anharmonicity of the isolated catalyst, in Figure 4.9(b) a continuum solvation model does not capture the bias of solvation on conformational sampling. Thus, solution-phase thermal conformational sampling contributes a significant free energy contribution to co-monomer incorporation selectivities.

Solvation Effects on Elementary Steps

Solvation effects are now compared for the monomer interconversion free energy and the insertion free energy BHDs. In Figure 4.10, the mean of the absolute values of the solvation corrections is computed to assess the magnitude of the solvation corrections across the three catalysts and co-monomers. The solvation effect on insertion BHDs is negligible for continuum solvation models (black bars) due to

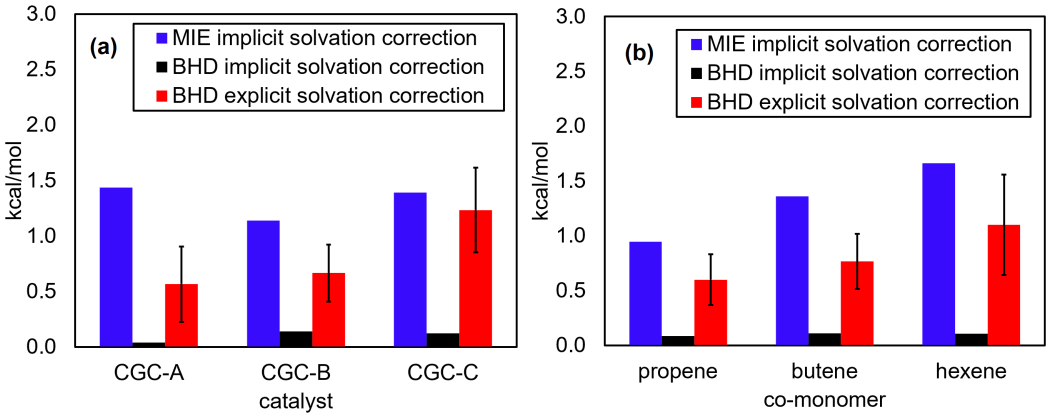

Figure 4.10: The mean of the absolute values of the solvation corrections are taken to assess the magnitude of the solvation corrections for the monomer interconversion energy (MIE) (ΔG_{ce}) and the insertion barrier height difference (BHD) ($\Delta G_c^{\ddagger} - \Delta G_e^{\ddagger}$). (a) The magnitude of the solvation corrections across CGC catalysts is compared. (b) The magnitude of the solvation corrections across co-monomers is compared. Both the MIE and BHD have significant solvation corrections, and the MIE is uniquely sensitive to implicit solvation.

the similarity of the catalyst structure throughout insertion. Explicit solvation (red bars) better characterizes the non-zero contribution of conformational sampling on the relative heights of the insertion barriers. There is a clear trend of conformational flexibility influencing solvation corrections, with larger monomers and CGC-C demonstrating greater solvation effects.

For the case of the monomer interconversion energy calculation, a continuum solvation model captures significant changes in solvent-solute electrostatic interactions (blue bars). Calculated implicit solvation corrections reflect the preference of the co-monomer to remain unbound in solution. Although not quantified in this study, an explicit solvation correction to the interconversion energy is expected to be non-zero. The upshot is the significant contribution of solvation effects to the monomer binding and insertion steps, and solvation corrections on the 0–2 kcal/mol scale are relevant to co-monomer incorporation prediction.

Towards Quantitative Predictivity

Predicting co–incorporation ratios requires the calculation of composite monomer binding and insertion reaction free energies at sub–kcal/mol resolution. Energy contributions captured by molecular dynamics sampling are not replicated by im-

proving the accuracy of the harmonic approximation to the incorporation free energies. Changing the DFT method to a larger basis set or hybrid functional, as seen in Figure 4.3, does not yield additional information about the reaction energetics, as the computed $\Delta\Delta G^{\ddagger}$ across methods is spread in a narrow range and have consistent trends. Refinements in energy accuracy are expected to come from a comprehensive treatment of the solution-phase thermal conformational anharmonicity for each of the elementary steps involved in co–incorporation (e.g., monomer interconversion).

The main issue at hand is the requirement of longer trajectories for full thermal conformational sampling, to reduce the errors associated from sampling finite trajectories. Tight error bars for $\Delta\Delta G^{\ddagger}$ derived from sampling data is necessary due to the error propagation of four independent free energy calculations: two binding energies and insertion barrier heights. Hence, very long sampling times are necessary, while preserving the quality of the underlying potential energy surface. Towards this, DFT-quality potential surfaces are needed at a lower computational cost to allow for complete conformational sampling.

Conclusion

The prediction of co-monomer incorporation selectivity is a challenging problem involving the calculation of four independent free energies. However, sampling molecular dynamics trajectories in solution-phase allows for a more accurate accounting of anharmonic thermal conformational contributions to the reaction free energies associated with incorporation selectivity. The anharmonic contribution contribution of the isolated catalyst to the insertion barrier free energy is further amplified in the solution-phase. Employing an implicit solvation model or a better DFT method does not account for these anharmonic contributions.

The crucial insight is the corrections from solution-phase anharmonic conformational sampling of the ethene and co-monomer insertion barriers are on the order of $\sim$ 1 kcal/mol, and approximately the same scale as $\Delta\Delta G^{\ddagger}$ from the experimental octene incorporation data. The relevance of the anharmonic free energy correction is the accurate rank ordering of catalysts that have similar free energy differences, which requires a precise calculation that incorporates key contributions from anharmonic solution-phase sampling. Hence, resolving the experimental free energy differences for the prediction of co-monomer incorporation statistics necessitates further solution-phase thermal sampling of the insertion barrier and the interconversion equilibrium. The small energy scales associated with co-monomer incorporation catalysis imposes a strict requirement of accurate free energy calculations that model not only electronic and harmonic thermal contributions but also anharmonic free energy contributions from solution-phase conformational sampling.

BIBLIOGRAPHY

(1) Sauter, D. W.; Taoufik, M.; Boisson, C. *Polymers* **2017**, *9*, 185.

(2) Kaminsky, W. *Macromolecular Chemistry and Physics* **2008**, *209*, 459–466.

(3) Hosoda, S. *Polymer Journal* **1988**, *20*, 383–397.

(4) Chen, C. *Nature Reviews Chemistry* **2018**, *2*, 6–14.

(5) Bursch, M.; Hansen, A.; Pracht, P.; Kohn, J. T.; Grimme, S. *Phys. Chem. Chem. Phys.* **2021**, *23*, 287–299.

(6) Skyner, R. E.; McDonagh, J. L.; Groom, C. R.; Mourik, T. v.; Mitchell, J. B. O. *Phys. Chem. Chem. Phys.* **2015**, *17*, 6174–6191.

(7) Houk, K. N.; Liu, F. *Acc. Chem. Res.* **2017**, *50*, 539–543.

(8) Pracht, P.; Grimme, S. *Chem. Sci.* **2021**, *12*, 6551–6568.

(9) Ribeiro, R. F.; Marenich, A. V.; Cramer, C. J.; Truhlar, D. G. *J. Phys. Chem. B* **2011**, *115*, 14556–14562.

(10) Zheng, J.; Yu, T.; Papajak, E.; Alecu, I. M.; Mielke, S. L.; Truhlar, D. G. *Phys. Chem. Chem. Phys.* **2011**, *13*, 10885–10907.

(11) Kolář, M.; Fanfrlík, J.; Lepšík, M.; Forti, F.; Luque, F. J.; Hobza, P. *J. Phys. Chem. B* **2013**, *117*, 5950–5962.

(12) Bursch, M.; Hansen, A.; Pracht, P.; Kohn, J. T.; Grimme, S. *Phys. Chem. Chem. Phys.* **2021**, *23*, 287–299.

(13) Grimme, S.; Bohle, F.; Hansen, A.; Pracht, P.; Spicher, S.; Stahn, M. *J. Phys. Chem. A* **2021**, *125*, DOI: 10.1021/acs.jpca.1c00971.

(14) Bochmann, M. *Organometallics* **2010**, *29*, 4711–4740.

(15) Karl, J.; Dahlmann, M.; Erker, G.; Bergander, K. *J. Am. Chem. Soc.* **1998**, *120*, 5643–5652.

(16) Dahlmann, M.; Erker, G.; Bergander, K. *J. Am. Chem. Soc.* **2000**, *122*, 7986–7998.

(17) Zaccaria, F.; Ehm, C.; Budzelaar, P. H. M.; Busico, V. *ACS Catal.* **2017**, *7*, 1512–1519.

(18) Laine, A.; Coussens, B. B.; Hirvi, J. T.; Berthoud, A.; Friederichs, N.; Severn, J. R.; Linnolahti, M. *Organometallics* **2015**, *34*, 2415–2421.

(19) Ehm, C.; Budzelaar, P. H. M.; Busico, V. *European Journal of Inorganic Chemistry* **2017**, *2017*, 3343–3349.

(20) Brintzinger, H. H.; Fischer, D.; Mülhaupt, R.; Rieger, B.; Waymouth, R. M. *Angewandte Chemie International Edition in English* **1995**, *34*, 1143–1170.

(21) Flisak, Z.; Ziegler, T. *Proceedings of the National Academy of Sciences* **2006**, *103*, 15338–15342.

(22) Chan, M. S. W.; Vanka, K.; Pye, C. C.; Ziegler, T. *Organometallics* **1999**, *18*, 4624–4636.

(23) Vanka, K.; Chan, M. S. W.; Pye, C. C.; Ziegler, T. *Organometallics* **2000**, *19*, 1841–1849.

(24) Ustynyuk, L. Y.; Fushman, E. A.; Lalayan, S. S.; Nifantév, I. E. *Journal of Organometallic Chemistry* **2012**, *700*, 166–179.

(25) Xu, Z.; Vanka, K.; Ziegler, T. *Organometallics* **2004**, *23*, 104–116.

(26) Tobisch, S.; Ziegler, T. *J. Am. Chem. Soc.* **2004**, *126*, 9059–9071.

(27) Laine, A.; Linnolahti, M.; Pakkanen, T. A.; Severn, J. R.; Kokko, E.; Pakkanen, A. *Organometallics* **2011**, *30*, 1350–1358.

(28) Rowley, C. N.; Woo, T. K. *Organometallics* **2011**, *30*, 2071–2074.

(29) Woo, T. K.; Margl, P. M.; Blöchl, P. E.; Ziegler, T. *J. Phys. Chem. B* **1997**, *101*, 7877–7880.

(30) Yang, S.-Y.; Ziegler, T. *Organometallics* **2006**, *25*, 887–900.

(31) Senn, H. M.; Thiel, W. *Angewandte Chemie International Edition* **2009**, *48*, 1198–1229.

(32) Hu, H.; Lu, Z.; Yang, W. *J. Chem. Theory Comput.* **2007**, *3*, 390–406.

(33) Njegic, B.; Gordon, M. S. *J. Chem. Phys.* **2006**, *125*, 224102.

(34) Schmalz, F.; Kopp, W. A.; Kröger, L. C.; Leonhard, K. *ACS Omega* **2020**, *5*, 2242–2253.

(35) Klosin, J.; Fontaine, P. P.; Figueroa, R. *Acc. Chem. Res.* **2015**, *48*, 2004–2016.

(36) Braunschweig, H.; Breitling, F. M. *Coordination Chemistry Reviews* **2006**, *250*, 2691–2720.

(37) Klosin, J.; Fontaine, P. P.; Figueroa, R. *Acc. Chem. Res.* **2015**, *48*, 2004–2016.

(38) Shapiro, P. J.; Bunel, E.; Schaefer, W. P.; Bercaw, J. E. *Organometallics* **1990**, *9*, 867–869.

(39) Arriola, D. J.; Bokota, M.; Campbell, R. E.; Klosin, J.; LaPointe, R. E.; Redwine, O. D.; Shankar, R. B.; Timmers, F. J.; Abboud, K. A. *J. Am. Chem. Soc.* **2007**, *129*, 7065–7076.

(40) Klosin, J.; Kruper, W. J.; Nickias, P. N.; Roof, G. R.; De Waele, P.; Abboud, K. A. *Organometallics* **2001**, *20*, 2663–2665.

(41) Seeman, J. I. *J. Chem. Educ.* **1986**, *63*, 42.

(42) Manby, F. et al. **2019**, Publisher: ChemRxiv, DOI: 10.26434/chemrxiv.7762646.v2.

(43) Brandenburg, J. G.; Bannwarth, C.; Hansen, A.; Grimme, S. *J. Chem. Phys.* **2018**, *148*, 064104.

(44) Neese, F. *Wiley Interdiscip. Rev.: Comput. Mol. Sci.* **2012**, *2*, 73–78.

(45) Fukui, K. *Accounts of Chemical Research* **1981**, *14*, 363–368.

(46) E, W.; Ren, W.; Vanden-Eijnden, E. *Phys. Rev. B* **2002**, *66*, 052301.

(47) E, W.; Ren, W.; Vanden-Eijnden, E. *J. Chem. Phys.* **2007**, *126*, 164103.

(48) Maragliano, L.; Fischer, A.; Vanden-Eijnden, E.; Ciccotti, G. *J. Chem. Phys.* **2006**, *125*, 024106.

(49) Motta, A.; Fragalà, I. L.; Marks, T. J. *J. Chem. Theory Comput.* **2013**, *9*, 3491–3497.

(50) Sprik, M. *Faraday Discuss.* **1998**, *110*, 437–445.

(51) Roy, S.; Baer, M. D.; Mundy, C. J.; Schenter, G. K. *J. Phys. Chem. C* **2016**, *120*, 7597–7605.

(52) Cao, L.; Ryde, U. *Front Chem* **2018**, *6*, 89.

(53) Swope, W. C.; Andersen, H. C.; Berens, P. H.; Wilson, K. R. *J. Chem. Phys.* **1982**, *76*, 637–649.

(54) Andersen, H. C. *J. Chem. Phys.* **1980**, *72*, 2384–2393.

(55) Chao, K. C.; Seader, J. D. *AIChE Journal* **1961**, *7*, 598–605.

(56) Marenich, A. V.; Cramer, C. J.; Truhlar, D. G. *J. Phys. Chem. B* **2009**, *113*, 6378–6396.

Chapter 5

PHOSPHINE-PHENOXIDE NICKEL CATALYSTS FOR ETHYLENE/ACRYLATE COPOLYMERIZATION: OLEFIN COORDINATION AND COMPLEX ISOMERISATION STUDIES RELEVANT TO THE MECHANISM OF CATALYSIS

ABSTRACT

The insertion copolymerization of ethylene and acrylate remains a challenge in polymer synthesis due to decreased activities upon incorporation of polar monomer. Toward gaining mechanistic insight, two elusive four-membered chelated intermediates generated after acrylate insertion were prepared (**1-CCO** and **2-CCO**) and their ligand coordination and substitution behavior were studied. Specifically, an ethylene-coordinated species was characterized by NMR spectroscopy upon exposing **2-CCO** to ethylene at low temperatures, a rare observation for neutral late-transition metal polymerization catalysts. Thermodynamics of chelate-opening and monomer coordination from **2-CCO** were determined at –90 °C (ΔG of 0.4 kcal/mol for ethylene and 1.9 kcal/mol for 1-hexene). The Gibbs energy barrier of ligand exchange from pyridine to ethylene, a prerequisite for ethylene insertion in catalysis, was determined to be 3.3 kcal/mol. Ligand binding studies reveal that, compared to NiMe and Ni(CH_2SiMe_3) complexes, acrylate inserted species **1L-CCO** and **2L-CCO** produce compressed thermodynamic binding scales for both electronically and sterically differentiating ligands, potentially related to their more electron deficient nickel centers as suggested by computational studies. Triethylphosphine complexes **1P, 2P** and **2P-Me** were observed as both cis- and trans-isomers in solution. $^{31}P\{^{1}H\}$ EXSY NMR studies of **2P** reveal conversion between the cis- and trans-isomers that does not involve exchange with free PEt_3, supporting a mechanism of intramolecular isomerization. **2-CCO**, a neutral Ni(II) precatalyst that does not display an auxiliary ligand, serves as a highly active catalyst for copolymerization.

Introduction

The copolymerization of non-polar and polar monomers has garnered continued interest due to growing demand of diverse plastics in a plethora of industrial sectors [1–6]. Compared to the industrially employed radical process, coordination copolymerization has the potential to offer a precise control of copolymer microstructure and only requires mild conditions, and thus is considered as an economical and environmentally friendly alternative [7–9]. Several transition metal catalyst systems have been developed, with a focus on palladium and nickel complexes due to the low oxophilicity of these metal centers[10–19]. Among all reported systems, neutral nickel catalysts supported by bulky, asymmetric ligands stand out due to their high activity, low oxophillicity, and thermal stability, as well as the relatively low cost of the metal [20–25].

Despite promise for catalysis, mechanistic details of this family of neutral Ni copolymerization catalysts are less explored [26]. Mechanistic studies have largely been restricted by the scarcity of isolable intermediates relevant to catalysis. For example, the success of isolating products of monomer insertion with diimine palladium and nickel complexes allows in-depth studies of olefin coordination, migratory insertion, and isomerization relevant to the copolymerization of ethylene and polar monomers including methyl acrylate [12, 27], vinyl acetate [28], and vinylalkoxysilanes [29–31]. Chain-walking with these symmetrical catalysts leads to the formation of highly branched copolymers [7, 27, 32, 33] deviating from the more widely used long chain polyolefins. In contrast, neutral, asymmetric group [10] catalysts produce long chain copolymers with few branches [14, 20], but gaining similar experimental insight of olefin coordination with these catalysts has been hampered by the presence of a strongly coordinating ligands L (e.g. pyridine or PR_3) that complete the square planar coordination sphere of the metal and must be substituted by olefin [26, 34, 35].

We recently reported the nickel phosphine phenoxide complexes **1** and **2** (Figure 5.1a, b) that serve as thermally robust, highly active catalysts for the ethylene/acrylate copolymereization [24]. Potentially owing to the steric protection ortho to the phenoxide, acrylate inserted species from **1** and **2** were isolable, allowing the determination of kinetic details of chain propagation (Figure 5.1c). These indicate that the migratory insertion of olefins is relatively slow compared to ligand exchange. Overall, the ethylene enchainment after acrylate is the rate-determining step for copolymerization and the acrylate-inserted species is the resting state of catalysis.

Investigations of olefin coordination has been impeded by the presence of pyridine in the coordination sphere and the thermodynamic preference for heterocycle binding. Notably, an auxiliary donor-free acrylate-inserted species, **2-CCO**, was prepared and isolated (Figure 5.1a). Herein, we report the observation of olefin-coordinated adducts using **2-CCO**, a rare demonstration for neutral Ni(II) precatalysts. We also report relative binding affinities for olefins and other donors relevant to copolymerization catalysis. In addition, facile access to **2-CCO** allowed for the determination of thermodynamics of chelate opening by monomer coordination. Using **2**, we also report quantitative data relevant to mechanism of cis/trans isomerization. Notably, complex **2-CCO** is also an efficient catalyst in both ethylene homopolymerization and copolymerization with tert-butyl acrylate (^{t}BA), represent the first example of ancillary ligand L free neutral nickel polymerization catalysts.

Results and Discussion

Preparation and Characterization of Ni(CCO) Complexes

Compound **2lut-Me** was accessed by treating **PONap-H** with one equiv. of $NiMe_2$(TMEDA) in the presence of excess of lutidine (Figure 5.2a). Addition of excess ^{t}BA to an in situ generated solution of **2lut-Me** led to the isolation of **2-CCO** (Figure 5.2a), as previously reported [24]. Compound **2-CCO** represents the first spectroscopically and crystallographically characterized example of the auxiliary ligand free, four-membered chelate generated after acrylate insertion. Solution-state NMR characterization indicates the existence of two conformers that exchange on the NMR time scale. Specifically, two sets of sharp peaks were observed in the ^{1}H and ^{31}P{^{1}H} NMR spectra at temperatures ranging from 0 °C to –60 °C. The ratio of two conformers varies under different temperatures. Coalescence of the peaks corresponding to the two isomers was observed at 20 °C.

Akin to the synthesis and isolation of **2-CCO**, reaction of **POP-H** and one equiv. of $NiMe_2$(TMEDA) in the presence of excess of lutidine allowed for the generation of **1lut-Me** (Figure 5.2b). After removal of lutidine under vacuum, addition of excess ^{t}BA results in a color change from yellow to red over the course of 0.5 h. ^{31}P{^{1}H} NMR spectra revealed the consumption of **1lut-Me** and the appearance of a new species after removal of volatiles. The absence of lutidine resonances indicates the loss of this ligand and potential generation of acrylate inserted species that chelate to Ni. Indeed, the ^{1}H NMR spectra feature resonances similar to those observed for **2-CCO**. The room temperature ^{31}P{^{1}H} NMR spectrum displays two

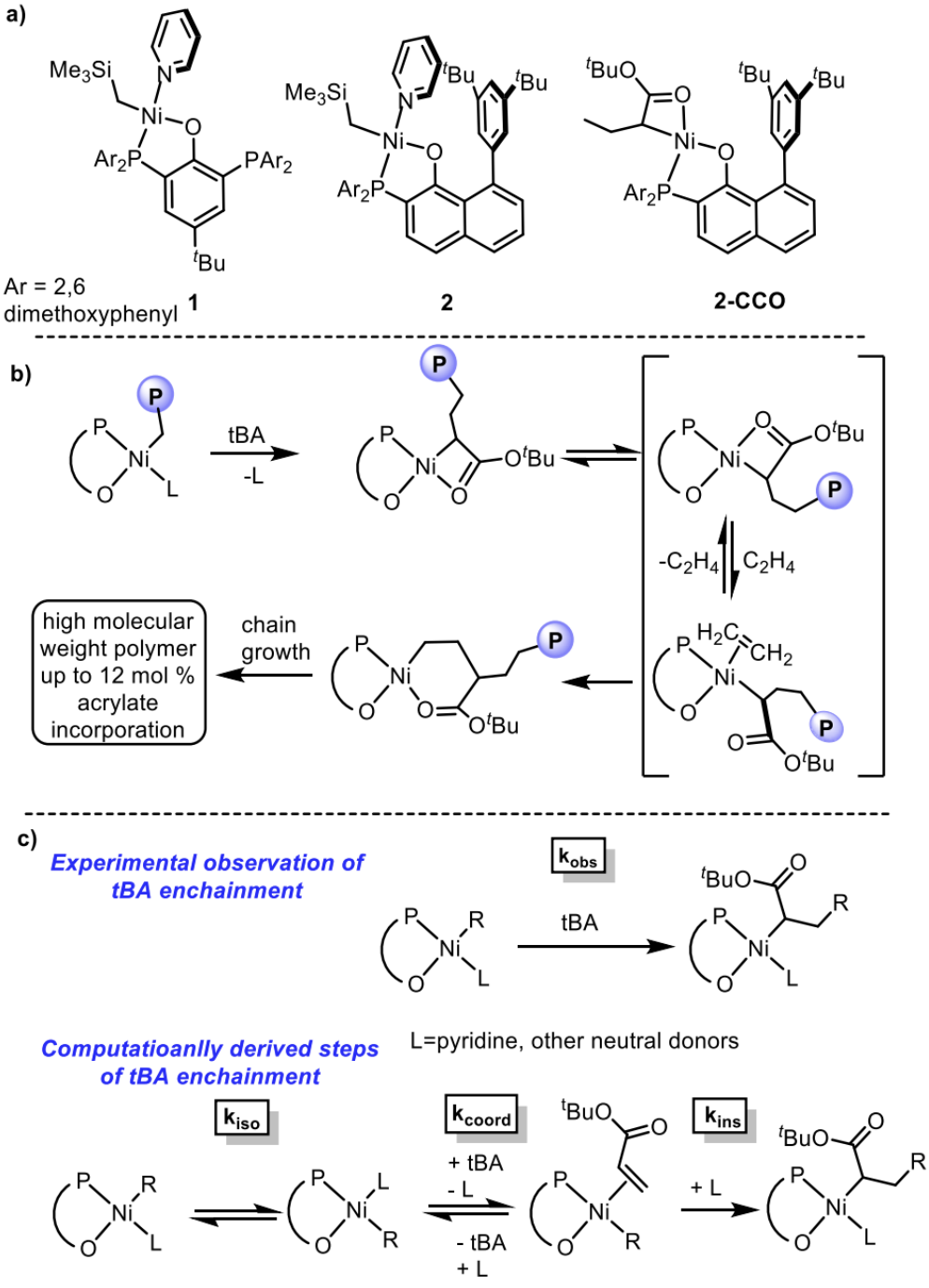

Figure 5.1: Nickel complexes and mechanistic pathways explored. (a) Nickel complex **1**, **2**, **2-CCO**. (b) Mechanism of chain growth by Ni-phosphine phenoxide catalysts. (c) Experimental and computational steps for acrylate enchainment.

sets of broad resonances corresponding to bound phosphine environments. Variable temperature NMR spectroscopy was performed and the observed coalescence of the two species at 50 °C is consistent with a fluctional process between two conformers. Further interrogation via ^{1}H-^{1}H COSY experiments provides evidence of the tentative assignment of this species as **1-CCO**, the POP variant of **2-CCO**. Both are four-membered chelates generated after 2,1-insertion of ^{t}BA.

While crystallographic characterization of **1-CCO** has not been successful thus far, the solid-state structure of the PEt_3 adduct **1P-CCO** was obtained upon the addition of excess PEt_3 to **1-CCO** (Figure 5.2c). Single crystals of **1P-CCO** were grown via vapor diffusion of hexanes into the toluene solution of **1-CCO** with PEt_3 at -40 °C (Figure 5.2c). The solidstate structure reveals that the ^{t}BA indeed inserts in a 2,1-fashion into the Ni-CH_3 bond and is consistent with the assignment of **2-CCO** as the auxiliary donor-free compound generated after 2,1-insertion of ^{t}BA.

As representative models for the proposed resting state in catalysis of ethylene/acrylate copolymerization, facile access to acrylate-inserted species, **1-CCO** and **2-CCO** provide a unique opportunity to investigate details relevant to the proposed rate-determining step. The mechanistic studies described below aim to gain insights related to the elementary steps of monomer enchainment, including chelate opening/olefin coordination and cis/trans isomerization. The auxiliary ligand-free nickel acrylate insertion complexes are integral to this study as they preclude additional ligands that obfuscate olefin coordination behavior and provide the possibility of quantitative determination of thermodynamics of chelate opening and binding affinities of olefins.

Investigation of Olefin Coordinated Complexes

Given the strain in the metallacycle of **1-CCO** and **2-CCO** and the lack of a strong fourth ligand, we targeted olefin coordination studies. Indeed, upon addition of 4 atmospheres of ethylene to a frozen solution of **2-CCO** in d^8-toluene, a new ^{31}P{^{1}H} NMR resonance at –19.3 ppm was observed at temperatures ranging from –90 to –70 °C, which was tentatively assigned to the ethylene adduct, **2et-CCO** (Scheme 1). Presence of a large excess of ethylene and the broadened resonances of two conformers of **2-CCO** at –90 °C precluded ^{1}H NMR assignment of the proposed 2etCCO. 36 The identity of **2et-CCO** was supported via ^{13}C{^{1}H} NMR, with the coordinated ethylene resonances appearing as broad multiplets at 104.5 and 102.5 ppm. These shifts are within the range of cationic Pd(II) ethylene adducts

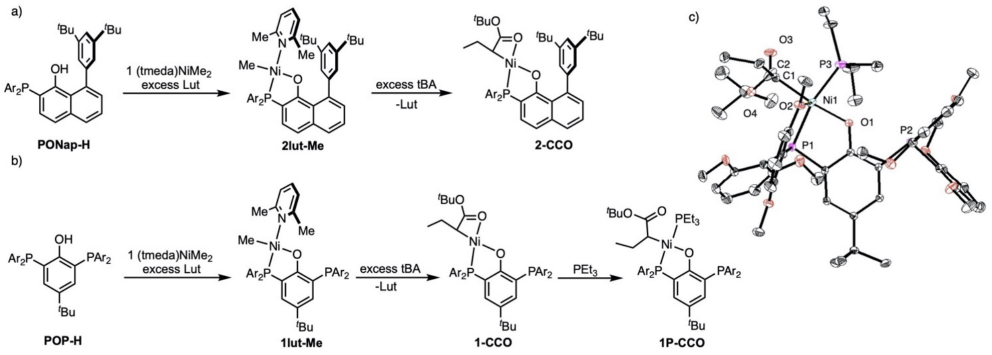

Figure 5.2: Preparation of nickel chelated-alkyl ether complexes (a and b) and ORTEP Depiction of **1P-CCO** (c, H-atoms excluded for clarity).

[12, 36, 37]. The disappearance of resonances at temperatures above –70 °C and concomitant broadening of the remaining resonances along with reappearance of **2et-CCO** upon recooling to –90 °C, can be reasoned as a dynamic process with ethylene coordination and dissociation coupled with potential chelate dissociation and reassociation, respectively. The behaviour is consistent with the reversible formation of an ethylene adduct, and impeded isolation of **2et-CCO**.

In addition to the resonance corresponding to **2et-CCO** in $^{31}P\{^{1}H\}$ NMR, a new resonance also appears at approximately –7.8 ppm. This resonance may represent the formation of a separate isomer of an ethylene coordinated species, or a species which is the result of further reactivity of **2et-CCO**. To further confirm the assignment of the –19.4 ppm as the ethylene-coordinated species and expand the reactivity to other olefins of interest, **2-CCO** was exposed to 200 equivalents of 1-hexene at low temperatures. The resultant $^{31}P\{^{1}H\}$ NMR shows the partial formation of the analogous species, **2hex-CCO**, which displays a $^{31}P\{^{1}H\}$ resonance at approximately –20.6 ppm, yet a peak comparable to the unknown species observed at –7.8 ppm is not observed. This scenario further supports that the unknown species may be an isomer of **2et-CCO** generated after further reactivity with ethylene.

To further support our assignment of **2et-CCO** and gain more insight into the unknown species, ^{13}C-labelled ethylene was employed. Addition of four atmospheres of ^{13}C-ethylene resulted in a slightly shifted resonance in $^{31}P\{^{1}H\}$ NMR at –19.6 ppm corresponding to **2et*-CCO**. The $^{13}C\{^{1}H\}$ NMR of the equilibrium mixture of **2-CCO** and **2et*-CCO** displayed a broad, high-intensity multiplet at approximately

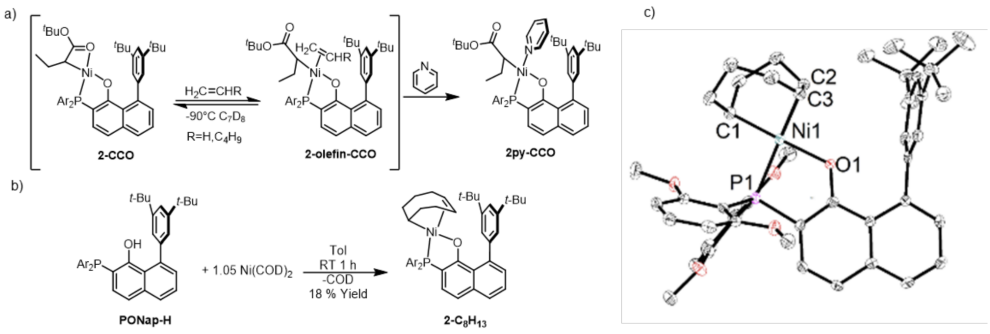

Figure 5.3: Reactivity and synthesis of olefin-coordinated complexes. (a) Equilibrium between **2-CCO** and olefin-coordinated variants $2C_nH_{2n}$-CCO as well as reaction with pyridine to form **2py-CCO**. (b) Formation of 2-C_8H_{13}. (c) ORTEP Depiction of 2-C_8H_{13} (bottom). H-atoms are excluded for clarity.

99.0 and 95.5 ppm. The 6 ppm chemical shift for **2et*-CCO** in comparison to **2et-CCO** may be the result of a low-lying paramagnetic state, potentially a tetrahedral Ni(II) species [38, 39]. The ^{13}C olefin-based resonance disappears when the solution is warmed to temperatures above -70 °C, consistent with the behaviour observed in the ^{31}P{^{1}H} NMR spectra of **2et-CCO**. Lastly, further evidence of the assignment of the olefin adduct, **2et-CCO**, is provided by vacuum transferring pyridine to the frozen mixture of **2-CCO** and **2et-CCO** in toluene, which results in the complete conversion to the previously characterized, pyridine bound species **2py-CCO** (Figure 5.3a). These experiments, collectively, discount the potential assignment of the unknown species as an ethylene insertion compound.

Despite our best efforts, crystallographic characterization of **2et-CCO** was unattainable. Toward obtaining structural confirmation on an olefin adduct that could benchmark the chemical shifts observed in ^{31}P{^{1}H} and ^{13}C{^{1}H} NMR and attempt to locate the resonances of the bound olefin in ^{1}H NMR, we sought to employ a more stable chelated olefin. Previously reported Ni-phosphino phenoxide catalysts were generated from biscyclooctadiene Ni(0) (Ni(COD)$_2$) as a precursor to generate the related cyclooct-4-enyl Ni complexes. Addition of Ni(COD)$_2$ to one equivalent of the **PONap-H** ligand at room temperature resulted in the formation of a cyclooct-4-enyl complex (**2-C_8H_{13}**) (Figure 5.3b).

Single-crystal XRD characterization revealed that 2-C_8H_{13} (Figure 5.3c) features the olefin within the metallacycle coordinated to the Ni center trans to the phosphine

donor. Importantly, the $^{31}P\{^{1}H\}$ NMR spectrum of **2-C_8H_{13}** displays a singlet at –18.00 ppm, a resonance consistent with the aforementioned olefin adducts of **2**. Similarly, $^{13}C\{^{1}H\}$ NMR of solution of **2-C_8H_{13}** displayed resonances corresponding to the bound olefin at 102.2 and 105.0 ppm with 2 JCP coupling constants of 14.7 and 2.6 Hz. Both chemical shifts are in the vicinity of the olefin coordinated resonances observed in solution for **2et-CCO** and **2et*-CCO**. The ^{1}H NMR spectrum of **2-C_8H_{13}** features two multiplets corresponding to the coordinated olefin at 4.95 and 5.23 ppm. $^{13}C\{^{1}H\}x^{1}H$ HSQC confirms that these resonances are associated with the olefinic protons These proton resonances are consistent with the expected olefinic resonances bound to Ni(II) [40, 41]. To serve as a direct comparison, cooling a d^8-toluene solution of **2-C_8H_{13}** to -90 °C was performed and corresponding NMR spectra were collected. $^{31}P\{^{1}H\}$ NMR at -90 °C displayed significant broadening compared to the room-temperature spectra which may indicate an exchange process potentially between enyl and allyl isomers, or different conformers. The ^{1}H NMR spectrum also observed broadening at -90 °C, including the olefinic resonances that bear $W_{1/2}$ of approximately 60 Hz. Significant broadening of olefinic resonances at -90 °C provides potential reasoning to the challenges in assigning the coordinated ethylene resonance by ^{1}H NMR spectroscopy. Collectively, these experiments provide compelling evidence of the assignment of the ethylene coordinated species, **2et-CCO**, from the exposure of 4 atmospheres of ethylene to complex **2-CCO**.

Despite the lack of auxiliary donor, addition of 4 atmospheres of ethylene to complex **1-CCO** did not result in predominant formation of an ethylene coordination species similar to **2et-CCO** under a variety of temperature ranges. This suggests that **1et-CCO** may be a comparatively higher energy intermediate or **1-CCO** is a more stable species compared to **2-CCO**.

Methyl acrylate and ^{t}BA were also added to **1-CCO** and **2-CCO** targeting acrylate coordinated species. Even with a large excess of acrylate, no evidence of coordination was observed. This behavior indicates that coordination of acrylate is substantially disfavoured in comparison to chelate formation, an observation consistent with the copolymer microstructure lacking subsequent insertion of acrylates.

a)

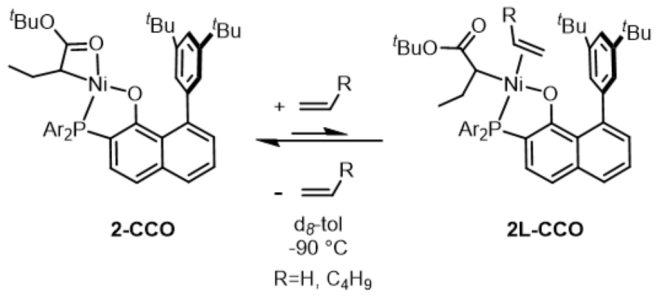

Product	T (K)	K_{eq} (1/mol)	ΔG (kcal/mol)
2et-CCO	183	3.0×10^{-1}	0.4
2hex-CCO	183	5.5×10^{-3}	1.9

b)

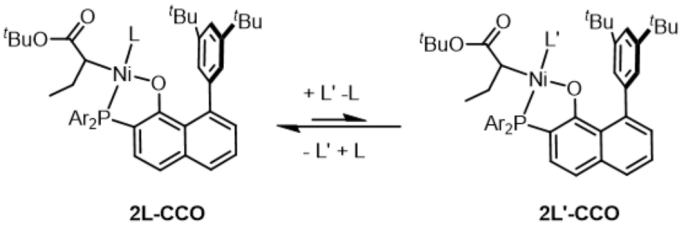

L	L'	T (K)	K_{eq} (1/mol)	ΔG (kcal/mol)
Py	Lut	183	4.8×10^{-3}	1.9
Lut	C_2H_4	183	2.3×10^{-2}	1.4
Py	C_2H_4	183	1.1×10^{-4}	3.3
Lut	tBA	-	n.o	n.o

Figure 5.4: Experimental thermodynamic data for nickel complex reactivity. (a) Thermodynamic values of ring opening and monomer coordination. (b) Thermodynamic values of ligand exchange between ethylene and pyridines.

Thermodynamics of Chelate Opening

Intrigued by the observation of olefin coordinated species, we sought to gain quantitative measurements of the relative binding of olefins to neutral Ni(II) catalysts. As an isolable model for the resting state of catalysis, complex **2-CCO** was explored for reversible chelate opening through dissociation of the alkyl ester group and monomer coordination. Addition of ethylene led to an equilibrium mixture of **2-CCO** and **2et-CCO** at low temperatures. For comparison, the thermodynamics of chelate opening and 1-hexene coordination to access **2hex-CCO** was also studied.

Analysis of thermodynamic data (Figure 5.4) at low temperature indicates that the equilibrium lies on the side of the chelate. The equilibrium mixture of **2-CCO** and

2et-CCO at -90°C shows an equilibrium constant of 0.3 and ΔG of 0.4 kcal/mol, close to thermoneutral, consistent with the ability of these catalysts to perform efficient copolymerization. Coordination of 1-hexene requires a large excess of olefin to observe an equilibrium mixture of **2-CCO** and **2hex-CCO**. The measured thermodynamic binding constant of 5.5 x 10^{-3} and ΔG of 1.9 kcal/mol is significantly less favorable to olefin coordination than for ethylene, a consequence of the bulkier α-olefin.

Neutral Ni pre-catalysts employed in copolymerization catalysis typically feature a ligand L (e.g. pyridine) that must be substituted with olefin for propagation to occur [42]. Toward gaining quantitative data regarding the ligand substitution pre-equilibrium (Figure 5.1c), competitive binding of olefins vs different ancillary ligands, such as pyridine and lutidine, at neutral Ni(II) catalysts was explored.

Given the elusiveness of **2et-CCO** at temperatures above -70 °C, competitive binding experiments were conducted at -90 °C (Figure 5.4b). Pyridine and ethylene proved to have binding affinities that were not conducive to direct comparison. Therefore, 2,6-lutidine was used as a weaker binding ligand for comparison. A solution of complex **3** and an excess of 2,6-lutidine in d^8-toluene in a JYoung tube was frozen and exposed to four atmospheres of ethylene. The solution was subsequently thawed and vigorously shaken, and NMR experiments were conducted at -90 °C. To ensure thermodynamic equilibrium was established the solution was warmed to -10 °C for one hour and re-cooled to -90 °C and the $^{31}P\{^1H\}$ NMR spectrum was recollected. This process was repeated until the relative intensities of **2et-CCO** and **2lut-CCO** were unchanged. The resulting integrals were used to calculate the equilibrium constant for ligand substitution, KC_2H_4/lut, as 2.3 x 10^{-2} and ΔG of 1.4 kcal/mol. Separately, known amounts of pyridine and 2,6-lutidine were added to a sample of **2-CCO** in d^8-toluene and the solution was cooled to -90 °C. A similar procedure was employed to ensure the thermodynamic equilibrium was established and the resulting integrals were used to calculate the Klut/py of 2,6-lutidine binding from the pyridine-bound species (4.8 x 10^{-3}) and a ΔG of 1.9 kcal/mol. With these K_{eq} values determined, the binding affinity of ethylene from **2py-CCO** produces a K_{eq} of 1.1 x 10^{-4} and a ΔG of 3.3 kcal/mol. Acrylate coordination via olefin or carbonyl group oxygen coordination was not observed (vide supra) precluding experimental determination of equilibrium constants involving the polar olefin. This aspect was investigated computationally (vide infra).

To address the impact of the ancillary phosphinephenoxide ligand on the binding affinity of the labile ligands (L, Figure 5.1), a pyridine partition experiment between **1-CCO** and **2-CCO** was performed. Equimolar amounts of **1py-CCO** and **2-CCO** (Figure 5.5a) were mixed and the concentration of **1py-CCO**, **2-CCO**, **1-CCO**, and **2py-CCO** were determined by ^{31}P NMR spectroscopy. The distribution shows approximately 80% of the pyridine stays bound on **1py-CCO** with approximately 20% of **2py-CCO** formation, corresponding to a K1 of 8.0 x 10^{-2} and ΔG of 1.5 kcal/mol. This scenario indicates a higher binding affinity of pyridine to **1-CCO** than **2-CCO**, potentially owing to the more rigid bulk proximal to the neutral L donor in **2L** relative to **1L** impacting the planar pyridine ligand which extends further toward the aryl substituent in **2-CCO** than the chelate.

The above results allow direct comparison of the thermodynamic scales between **1L** and **2L** (Figure 5.5b) at room temperature. The experimentally determined donor binding at room temperature and computationally determined ones (indicated in blue), ethylene and ^{t}BA, show that for both ancillary ligands olefin binding is orders of magnitude disfavored relative to pyridines. The difference between ethylene and acrylate is, however, less pronounced with the **POP-H** compared to **PONap-H** ligand (1 vs 2) consistent with POP supporting a catalyst that incorporates more polar monomer [24].

Experimental Ligand Binding Studies of 1-2 with Various Ancillary Ligands.

Given that monomer enchainment after acrylate insertion is the propagation determining step in copolymerization, thermodynamic binding studies with a variety of electronically and sterically differentiating ligands was studied to gain insights relevant to monomer coordination. To further explore differences in L donor binding affinity to Ni species relevant to olefin polymerization, in addition to **2-CCO** and **1-CCO**, 1, 2, and **2lut-Me** were investigated as catalyst states prior to initiation and as models for the catalyst state after ethylene insertion. A series of pyridines with different electronic and steric properties were investigated. Ligands of more conical shape such as PEt_3 and $(O)PEt_3$, were also studied. These ligand binding competition studies afforded thermodynamic binding scales for the several nickel complexes; the logarithm of the K values relative to pyridine (KL/py) are shown in Figure 5.6. Notably, a compression in relative binding energies was observed between **1L-CCO** (4.0 pKa units) and **2L-CCO** (4.4) compared to **1L** (5.6), **2L** (5.8) and **2L-Me** (6.4). The difference in the spread of equilibrium constants appears for

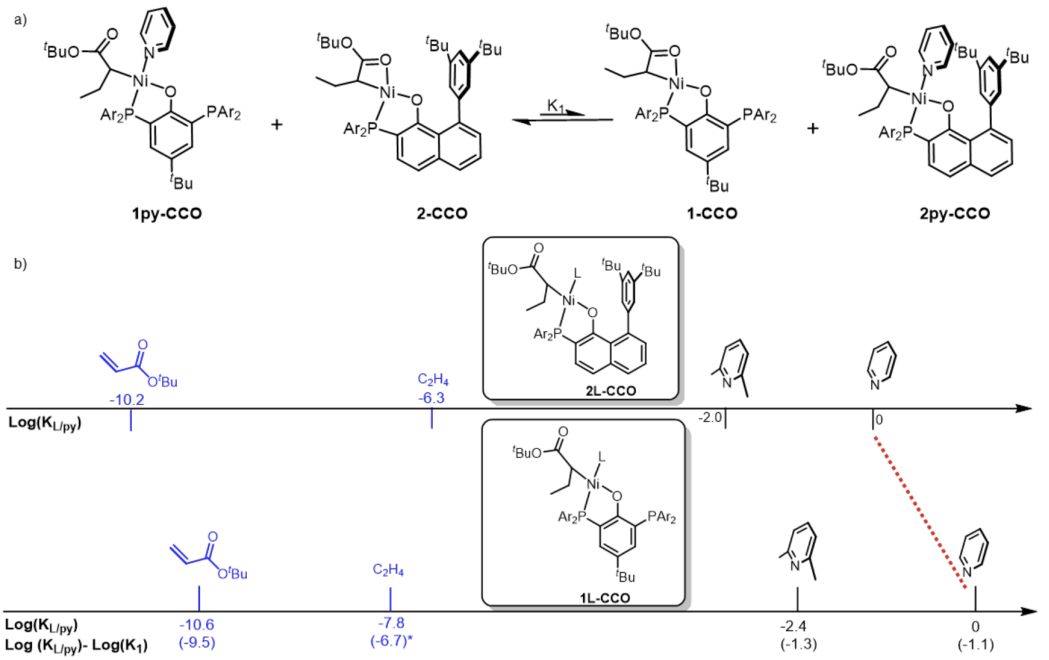

Figure 5.5: Ligand crossover study and relative binding affinities. (a) Crossover experiment with **1py-CCO** and **2-CCO**. (b) Thermodynamic scale for binding affinities of pyridine and olefinic donors to **1L-CCO** and **2L-CCO** (blue denotes computational determination). Dotted red line denotes adjustment based on the crossover experiment.

both sterically and electronically differentiated ligands, as observed with 2,6-lutidine and pentafluoropyridine. For example, the log(KLut/Py) values for **1L-CCO** and **2L-CCO** are -2.4 and -2.0, compared to those of **1L**, **2L** and **2L-Me**, which are -3.9, -4.4 and -3.4, respectively. The log(KPy-F5/Py) value for **2L-CCO** is -2.7 whereas a significantly decreased relative binding affinity is observed for **2L** and **2L-Me** at -5.1 and -5.8, respectively. The origin of the compressed scale for ligand binding affinity to **1L-CCO**, **2L-CCO** is intriguing. Given the similarity in binding constants between **1L-CCO** and **2L-CCO** and their differences in the ancillary ligand architecture, the phenomenon observed is more likely due to the differences between the alkyl ligands on nickel (C-bonded ester enolate vs vs methyl/CH_2SiMe_3) instead of originated from the phosphine-phenoxide ligands.

Relatedly, ethylene and CO binding affinity studies to cationic Pd(II) catalysts for ethylene/CO copolymerization revealed that Pd-acetyl and Pd-acyl groups resulted in a relatively compressed binding affinity of C_2H_4 to CO compared to the Pd-

CH3 analogue [37]. This result is consistent with our observation of the C-bonded enolate in **1L-CCO** and **2L-CCO** featuring a compressed scale for binding affinities; whether this is the result of the electron-withdrawing nature of the enolate moiety in **1L-CCO/2L-CCO** or the larger steric profile of the ester, is unclear.

Targeting the effect of P,O-ligands, we then compare the binding affinity for ancillary ligands L with nickel complexes featuring the same alkyl but supported by different phosphine phenoxides. For ligands L featuring a large distal but distal steric profile such as $P(O)Et_3$ and 4-tertbutylpyridine (^{t}Bupy), a much smaller log(KL/Py) was observed with **2L/2L-Me** than with **1L/1L-Me**. Specifically, ^{t}Bupy is a weaker ligand than pyridine for **2L** and **2L-Me**, but a stronger one for **1L**. The above scenarios are potentially due to the steric repulsion between the rigid substituent 3,5-ditertbutylphenyl group on the P,O-ligand and the large substituents on L (ethyl for $P(O)Et_3$ or ^{t}Bu for ^{t}Bupy) that are far reaching. Note that during ^{t}BA coordination during catalysis, the ^{t}Bu substituent on ^{t}BA, which is two atoms away from the olefin moiety, may also be hindered by the phenoxide substituent and thus lead to higher barrier for ^{t}BA coordination, and subsequently, lower ^{t}BA incorporation. Indeed, ethylene/^{t}BA copolymers produced by **2** feature much lower ^{t}BA incorporation than that produced by **1**.

To gain structural insight into ligand binding trends, single crystal X-ray diffraction studies were performed with **1L**, **1L-Me**, and **1L-CCO** featuring different ligands L (Figure 5.7). Among all seven complexes, **1P-CCO** features the shortest Ni-O distance, suggesting the strongest interaction between nickel and the axial methoxy group. For example, comparing **1P-CCO** and **1P**, differing only in the alkyl group coordinated to Ni, the Ni-O distance elongates from 2.701(2) Å to 2.967(3) Å, despite **1P-CCO** displaying a larger alkyl group. This is consistent with a more Lewis acidic nickel center in **1P-CCO** compared to **1L** and **1L-Me**, an aspect also supported by Mulliken population analysis. The increased polarisation of the Ni-C bond may be a contributor to the higher energy of ethylene insertion after acrylate insertion compared to consecutive ethylene insertions [43]. Furthermore, the more Lewis acidic metal center is expected to have a stronger interaction with the carbonyl group, stabilize the chelate, and slow down propagation, consistent with the experimental observation that ethylene enchainment from the chelate is the propagation determining step.

Analysis of the impact of the sterics of the pyridine ligand comparing **2lut-Me**, **1py-Me** and 1 shows almost identical Ni-N distances, but an increasing Ni-O distance (from 2.837(3) Å in **2lut-Me** to 3.086(3) Å in **1**) an indication of the ability of the substituents reaching out of the plane defined by the Ni coordination sphere to constrain axial coordination.

Overall, the donor coordination studies of **1L**, **1L-CCO**, **2L**, **2L-Me**, and **2L-CCO** provide insights on the relative binding affinities of a series of neutral donors to catalytically relevant Ni species. The compression of relative binding constants in acrylate-inserted species is proposed to be a manifestation of the different electronic properties of the alkyl groups at Ni. Additionally, the rigidity of the phosphine phenoxide ligand was found to hinder binding of ligands with a large volume. Because these experiments allowed a single olefinic ligand comparison (for **2et-CCO**), we sought to employ DFT calculations to benchmark the experimental measurements and to extend the scales to olefins employed in copolymerization catalysis.

DFT Calculation of Ligand Binding Affinity of 2 with Various Polar Olefins

The compression in relative binding energy scales for different catalyst systems is explored computationally, to gauge the electronic effect of catalyst R-group substitutions and test whether experimental binding energy trends extend to ligands explored computationally but not yet experimentally. The NiPONap catalyst systems **2L** (R = silane), **2L-Me** (R = Me), and **2L-CCO** (R = ester) are explored. The binding equilibria Kbind between the pyridine-bound catalyst and the monomer-bound catalyst is quantified experimentally and is used as a benchmark for the computational method. The binding energy ΔG_{bind} is related to the binding equilibrium constants K_{eq} obtained experimentally: $\Delta G_{bind} = RTlnK_{bind}$.

In Figure 5.9, the experimental binding equilibria for a set of representative ligands is converted to Gibbs free energies for the three catalyst systems **2L**, **2L-Me**, and **2L-CCO**, based on the data in Figure 5.6. A consistent trend is seen where the electron-deficient R = ester substitution on **2L-CCO** results in lower experimental binding energies, suggesting more facile binding to the electron-deficient metal center. Some variation is seen in the rank ordering of the other two R-groups which can be due to the additional effect of sterics on the binding energies. We want to see whether the effect of lower relative binding energies for electron-withdrawing substituents, as in the case of **2L-CCO**, extends to a broader set of ligands which include polar

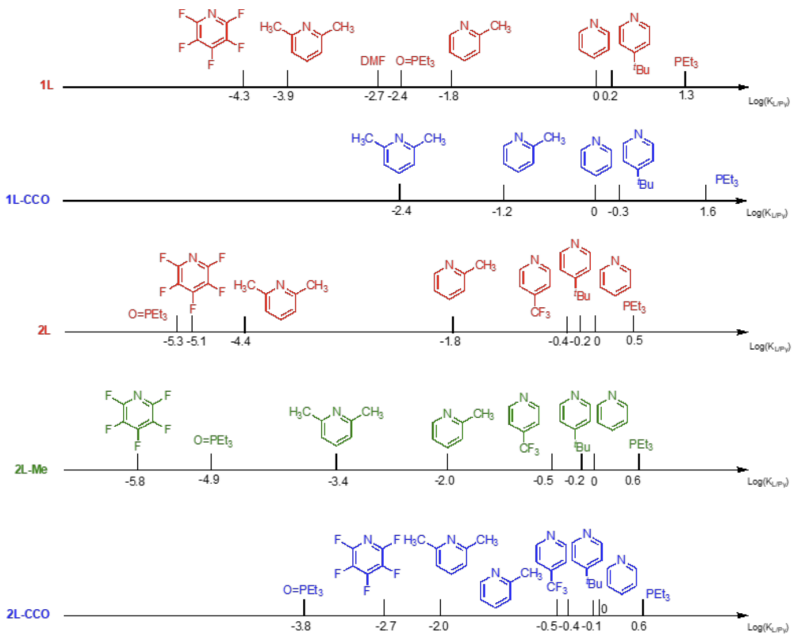

L	**1L** (1/mol)	**1L-CCO** (1/mol)	**2** (1/mol)	**2L-Me** (1/mol)	**2L-CCO** (1/mol)
PEt_3	1.3	1.6	0.5	0.6	0.6
4-^{t}Bu-Py	0.2	0.3	-0.2	-0.2	0.1
Py	0	0	0	0	0
2-Pic	-1.8	-1.2	-1.8	-2.0	-0.5
2,6-Lut	-3.9	-2.4	-4.4	-3.4	-2.0
Py-F_5	-4.3	N.D.	-5.1	-5.8	-2.7

Figure 5.6: Thermodynamic scales for binding affinities of neutral donors to **1L**, **1L-CCO**, **2L**, **2L-Me**, **2L-CCO** (top) and the table of selected values (bottom). Relative binding affinities determined by competition reactions with varying donors through either $^{31}P\{^1H\}$ NMR or ^1H NMR spectroscopy.

monomers relevant to co-polymerization. The quantification of polar monomer binding equilibria is experimentally difficult, and so we aim to use computation to elucidate the binding trends for these difficult substrates.

In Figure 5.10, we compute relative binding energies for the three catalyst systems for an extended set of ligands that includes pyridines, non-polar monomers (e.g., ethene, hexene), and polar monomers.For a given ligand, the relative binding energy for **2L-CCO** is shown on the x-axis and the relative binding energy for either **2L** or **2L-Me** is shown on the y-axis. There is a consistent electronic trend in the binding energies of substrates based on the identity of the R-group substitution on the catalyst, as shown by the observation that all the points in Figure 5.10 lie above

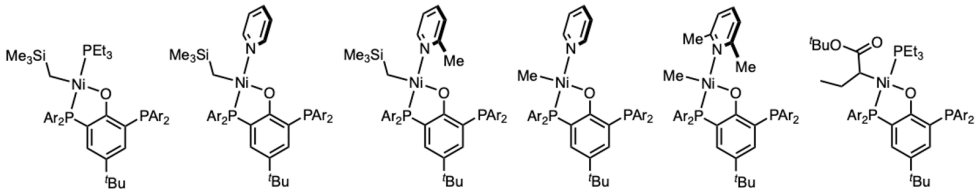

L	1P	1py	1pico	1py-Me	1lut-Me	1P-CCO
Ni-P	2.190(1)	2.134(1)	2.131(1)	2.132(1)	2.131(2)	2.211(1)
Ni-O	1.914(3)	1.926(2)	1.910(1)	1.915(2)	1.913(3)	1.922(1)
Ni-C	1.976(4)	1.950(4)	1.953(1)	1.927(3)	1.934(5)	1.983(3)
Ni-L	2.215(1)	1.938(3)	1.945(1)	1.934(2)	1.956(4)	2.230(1)
Ni-O'*	2.967(3)	2.837(3)	2.909(1)	2.927(2)	3.086(3)	2.701(2)

Figure 5.7: Selected bond lengths in Å of **1L-R** complexes (see SI for their solid-state structures).

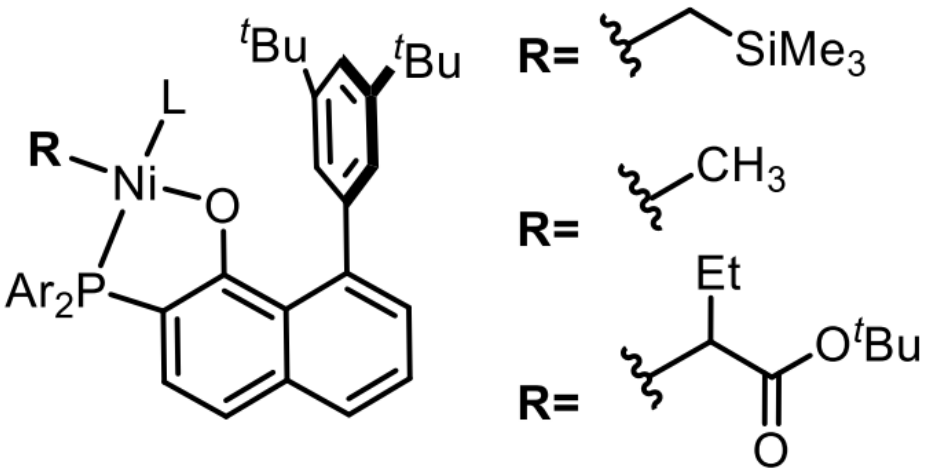

Figure 5.8: Ligand PONap-based catalyst systems explored computationally, with three R-group substitutions considered: **2L** (R = silane), **2L-Me** (R = Me), and **2L-CCO** (R = ester).

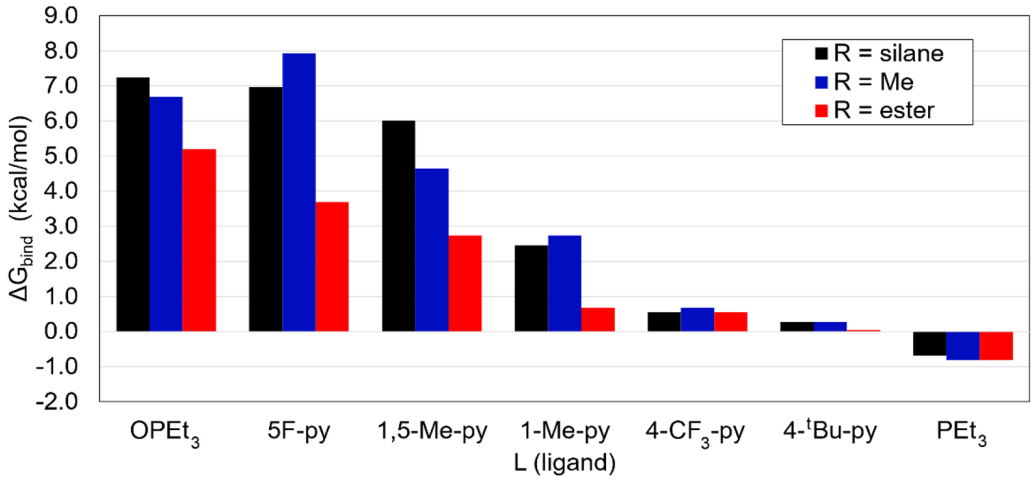

Figure 5.9: The experimental binding energies (relative to the pyridine-bound catalyst) for a representative set of monomers is converted to Gibbs free energies of binding using Equation (1). A systematic decrease in binding energies for **2L-CCO** (R = ester) is observed.

the y = x line. In other words, there is an increase in the binding energies for **2L** and **2L-Me** catalyst systems, compared to the analogous **2L-CCO** system of the same ligand. This is illustrated by a regression analysis of the binding energies in the figure. Variation of the points away from the regression line is considered to reflect the substrate-dependent effects of sterics on the relative binding energies.

The R-group dependence in binding energies is rationalized by the electronic effect of the R-group on binding. A more electrophilic metal center due to withdrawal of electron density by the electrophilic ester R-group on **2L-CCO** allows for more facile binding of ligand donors to the catalyst Ni metal center. To demonstrate the electrophilicity of the Ni center of **2L-CCO** in comparison to the other catalyst systems, in Figure 5.11, we calculate the NBO natural charge as a measure of electrophilicity of the Ni metal center for each monomer-bound catalyst system, and compared across the R-group on the catalyst. We see that the **2L-CCO** catalyst has a consistently more electrophilic metal center, as evidenced by larger computed natural charges at Ni. Although **2L-Me** has a less electrophilic center than **2L** as computed by NBO analysis, larger relative binding energies are sometimes seen for **2L-Me** in Figure 5.10. This suggests that the effect of sterics may play a role in catalyst-dependent binding energy trends as well. Even with the increased sterics

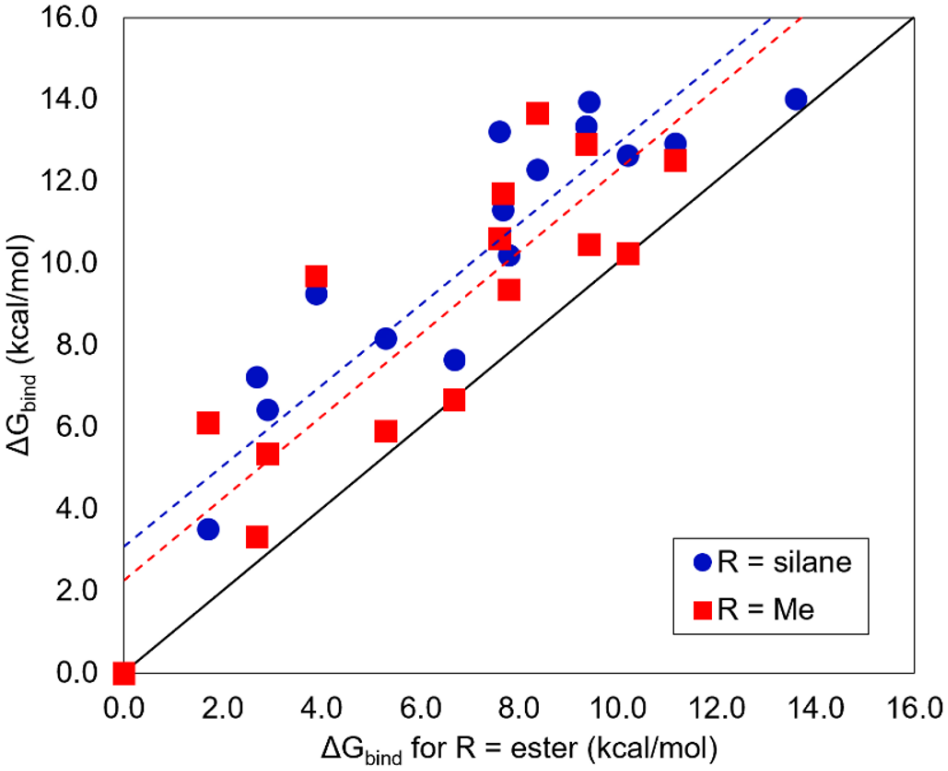

Figure 5.10: The calculated binding energies (relative to the pyridine-bound structure) are shown for each monomer (each point is a unique monomer) and catalyst (distinguished by marker color and shape). For a given ligand, the relative binding energy of the **2L-CCO** catalyst (R = ester) is shown on the x-axis and compared the analogous monomer bound structure for the **2L** (R = silane) and **2L-Me** (R = methyl) catalyst systems (blue circle and red square, respectively). Given that the regression lines for the **2L** (R = silane) and **2L-Me** (R = methyl) catalyst systems are above the y = x line, there is a consistent overall increase in binding energies for the R = Me and R = silane systems. The lines of regression for the catalyst systems 2L (R = silane) and 2L-Me (R = Me) are y = 0.98x + 3.07 kcal/mol ($R^2 = 0.82$) and y = 1.00x + 2.25 kcal/mol ($R^2 = 0.79$), respectively.

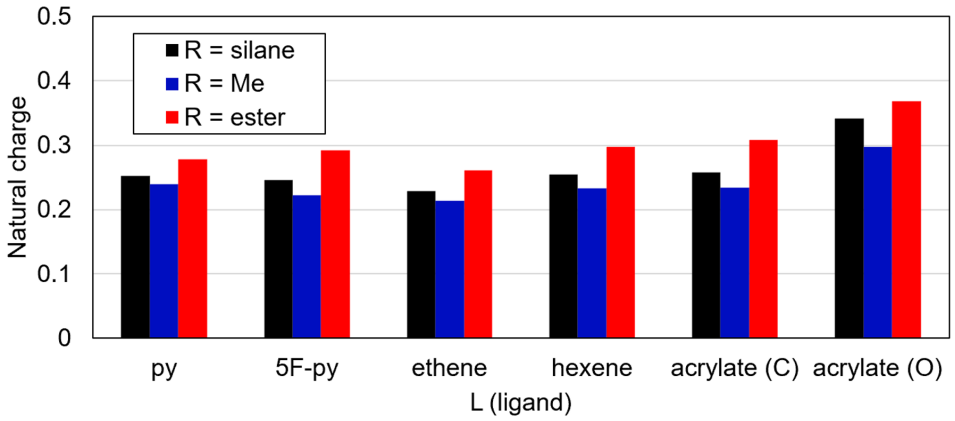

Figure 5.11: The natural charge of the Ni metal center on the monomer-bound catalyst is obtained from natural bond orbital (NBO) analysis and shown for a representative group of ligands. A larger natural charge indicates a more electrophilic metal center. We see a consistently larger Ni natural charge for the **2L-CCO** (R = ester) catalyst in compari-son to the **2L-Me** (R = Me) and **2L** (R = silane) systems, which help rationalize the ease of monomer binding to the **2L-CCO** catalyst system.

of the ester substitution on **2L-CCO**, the electronic effect dominates due to the electrophilic substitution on the Ni metal center, resulting in lower binding energies occuring consistently for the **2L-CCO** catalyst system in comparison to the other catalyst systems explored. We conclude that in our computational model the trend of lower binding energies for the **2L-CCO** (R = ester) catalyst observed experimentally (Figure 5.6) extends to the relative binding energies for polar monomers whose binding equilibria have not been experimentally characterized but explored computationally. Consistent with experiment, we observed a compression in binding energy scale for multiple classes of ligands binding to **2L-CCO**, in preference to the less electrophilic catalysts **2L** (R = silane) and **2L-Me** (R = Me). The implication is that the improvement in monomer coordination can be achieved by the installation of electron-withdrawing groups at the catalyst Ni metal center.

Cis/Trans Isomerization

The binding experiments described above provide insight regarding ligand coordination to analogues of catalysts after ethylene and ^{t}BA insertion; however, these studies are limited to examples where the ligand coordinates trans to the phosphine donor. Multiple computational studies of the mechanism of polymerization with

asymmetric bidentate ligands invoked cis/trans isomerization prior to olefin migratory insertion [14, 24, 44]. An example of Niphosphine phenoxide complexes favoring the cis isomer displays crown ethers to support Lewis acids appended to the ligand framework [38]. The presence of the cis isomer in this system is reasoned to be due to p-interaction effects from the pendant Lewis acid. Beyond these reports, experimental information about the mechanism of isomerization with catalytically relevant species is lacking. Given the computational evidence suggesting a cis/trans isomerization for the current catalysts [24], further insight on the mechanism of cis/trans isomerization was sought.

The observation of both cis and trans isomers in some of the ligand binding studies prompted us to prepare and isolate **2P**, **2P-Me**, and **2P-CCO** for further investigation. A substantial amount of the cis isomer (24% and 28%) was observed in both **2P** and **2P-Me** as supported by a set of two doublets with coupling constants of approximately 20 Hz in the ^{31}P NMR spectra, assigned to the two phosphine ligands. For comparison, the trans isomers show a coupling constant of 330 Hz. Complex **2P-CCO** shows no detectable amount of the cis isomer. Given that olefin enchainment after acrylate insertion is rate limiting, the absence of the cis isomer indicates that a preequilibrium between the trans and cis isomers is substantially shifted toward trans, overall, energetically disfavoring isomerization and slowing propagation. With access to a mixture of cis and trans isomers for **2P** and **2P-Me**, experimental studies were focused on the mechanism of isomerization.

Potential mechanistic pathways of the isomerization process are outlined in Figure 5.12 with Ni(PEt_3)(CH_2SiMe_3) as an example. Computational studies support an intramolecular mechanism involving coordination of a pendant ether group to generate a five-coordinate intermediate that undergoes a Berry pseudorotation, followed by ether dissociation (a) [45, 46]. An alternative associative mechanism involves intermolecular binding of a fifth ligand, PEt_3, followed by pseudorotation, and phosphine loss (b) [47, 48]; a dissociative mechanism involves loss of PEt_3 followed cis/trans isomerization of the three-coordinate species, and reassociation of phosphine (c) [49, 50].

The observation of both cis and trans isomers with **2P** and **2P-Me**, allows studies of the ligand exchange dynamics using ^{31}P{^{1}H} 2D NOESY (EXSY) experiments [51, 52]. EXSY studies with **2P** showed cross peaks corresponding to magnetization transfer between the cis and trans isomers at room temperature. When the EXSY experiment was performed in the presence of excess (10, 40 equivalents) of free

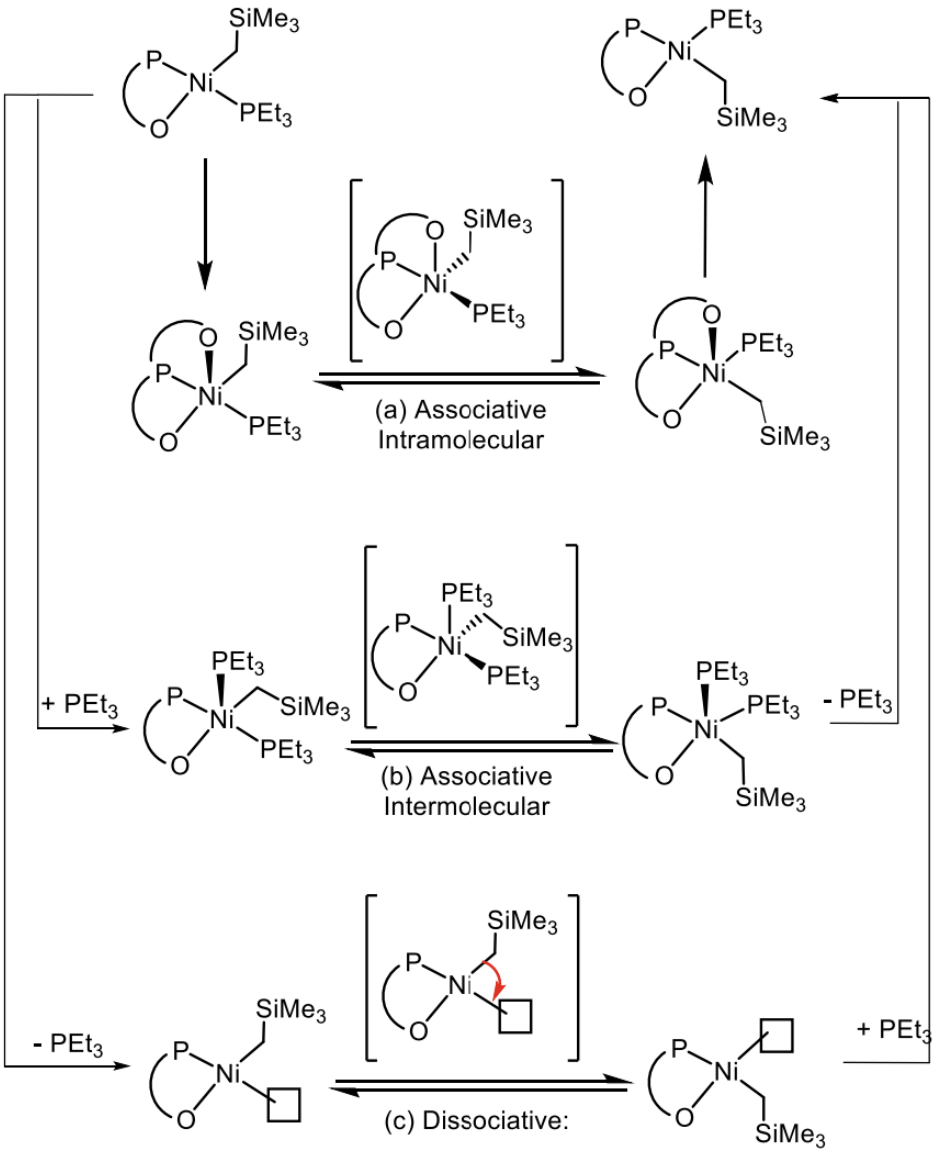

Figure 5.12: Potential mechanisms of cis/trans isomerization.

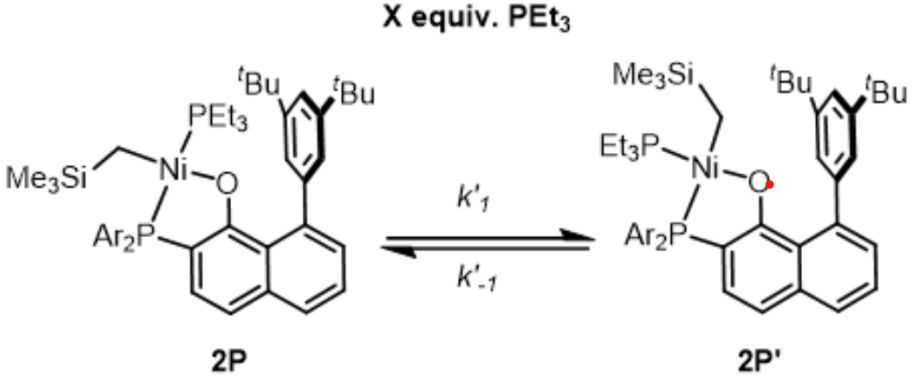

X	k'_1	k'_{-1}
0	0.6 s^{-1}	1.8 s^{-1}
10	0.9 s^{-1}	2.0 s^{-1}
40	0.9 s^{-1}	1.9 s^{-1}

Figure 5.13: Rates of magnetization transfer with varying equivalents of PEt_3.

PEt_3 and at higher temperatures, no cross peaks between free PEt_3 and the Ni species are observed. Using EXSYCalc, the magnetization transfer rates were determined through the exchange matrix with values ranging from 0.64 to 0.94 s^{-1} for the formation of the cis isomer and 1.82 to 1.98 s^{-1} for the formation of the trans isomer over the phosphine concentrations tested (Figure 5.13). The lack of substantial change of magnetization transfer rate with varying amounts of PEt_3 supports an intramolecular mechanism, such as (a), for isomer conversion [47]. An intermolecular mechanism (b or c) is inconsistent with the EXSY results. Notably, these results indicate that ligand substitution is slower than cis/trans isomerization under these conditions. **1P** also showed a small amount of cis isomer (4%). Though magnetization transfer is not detectable under temperatures ranging from 25-65 °C through the EXSY experiments, significant broadening of the resonances in $^{31}P\{^1H\}$ NMR spectra are observed as the temperature increases. Although a dynamic process may be occurring at high temperatures, the interconversion of the isomers with **1P** is slower than for **2P**.

Our studies, though not employing olefins, provide experimental support for the computational finding that the present phosphine phenoxide Ni catalysts undergo cis/trans isomerization via an intramolecular mechanism.

Using 3 as Auxiliary Donor Free Precatalysts for Polyolefin Synthesis

Our studies show that the competition for metal binding between the auxiliary ligands present in the precatalyst, pyridine or phosphine, and olefin monomers favors significantly the former. Therefore, we explored the impact of removing the auxiliary ligands (e.g. pyridine) on nickel catalyzed copolymerization of ethylene and polar monomers. Stable, coordinatively saturated metallocycle precatalysts prevent the use of the auxiliary ligand and has shown promising results in palladium catalyzed ethylene polymerization [17]. Examples of the nickel analogue are lacking; however, the effect of weaker ancillary ligands have been explored in Ni-phenoxyimine catalysts and weaker donor coordination leads to higher activity in ethylene polymerization and supresses β-H elimination [42]. Intermediates generated after monomer insertion are typically considered reactive and potentially not suitable as precatalysts. Given that **2-CCO** is the first structurally characterized, thermally robust four-membered chelate complex generated after ^{t}BA insertion, we explored its application as precatalyst in ethylene/^{t}BA copolymerization.

Both the nickel complex featuring a weak auxiliary ligand (lutidine, **2lut-Me**) and auxiliary donor-free nickel complexes (**2-CCO**) are highly active in ethylene/^{t}BA copolymerization (Table 1, Entry 1 4), and produce polymers with moderate molecular weight and ^{t}BA incorporation. Compared to 2 (Table 1, Entry 5), both are slightly less active overall, which is in contrast with previously reported effects of ligand L in ethylene polymerization. Notably, corresponding ethylene uptake curves revealed that **2lut-Me** and **2-CCO** consume ethylene much faster than 2 in the first 5 min of ethylene/^{t}BA copolymerization. However, a significant decrease of ethylene consumption rate was observed at longer time, which may relate to their decreased stability (Figure 5.14). Overall, our observation ind icates that the absence of strong auxiliary ligand L indeed accelerates the rate of monomer insertion, but it may also lead to a lower thermal stability. Given that high temperatures are preferred in industrial conditions, both aspects need to be taken into account in catalyst design.

#[a]	Catalyst	[^{t}BA] M	temp. (°C)	Act. (kg/ (mol · h))	$M_w/10^3$	PDI	^{t}BA %mol	T_m (°C)
1	**2lut-Me**	0.025	70	333	16.7	2.2	0.4	128
2	**2lut-Me**	0.05	70	157	15.3	2.4	0.8	124
3	**2-CCO**	0.025	70	303	18.0	2.3	0.4	128
4	**2-CCO**	0.05	70	139	17.3	2.6	0.8	124
5[b]	**2**	0.05	70	206	16.5	2.3	0.8	121

Table 5.1: Ethylene homopolymerization and ethylene/^{t}BA copolymerization. [a]Unless specified, V(total)=5 mL, [Ni]=0.25 µmol, ethylene pressure=400 psi, toluene solvent, t=1h, each entry represents multiply replicated runs. [b]Data has been reported in Ref 23.

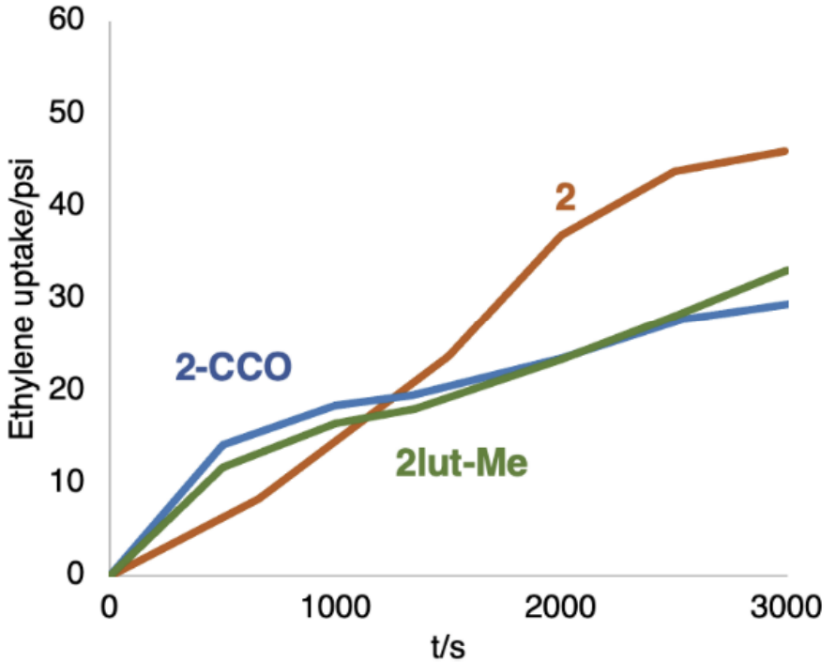

Figure 5.14: Ethylene uptake curves of **2**, **2lut-Me**, and **2-CCO**.

Conclusions

Auxiliary donor-free acrylate insertion compounds **1-CCO** and **2-CCO** were accessed through the insertion of ^{t}BA into Ni-Me bonds with the respective lutidine-bound precursors. Lack of a strong auxiliary donor in **2-CCO** allowed for the observation of olefin coordination complexes. Although equilibrium mixtures of **2-CCO** and olefin-bound species precluded isolation, the independently prepared

COD-inserted complex **2-C_8H_{13}** was isolated and characterized structurally and by spectroscopy and supports the assignment of the olefin coordinated species. These data show that ethylene, but not acrylate, is capable of opening the chelate generated after acrylate insertion. Ligand binding studies have provided quantitative thermodynamic data regarding the impact of precatalyst structure on binding of donors such as olefins, pyridines, and phosphines.

A relatively compressed binding scale was observed with the acrylate inserted species (**1-CCO** and **2-CCO**) compared to the Ni-CH_2SiMe_3 and Ni-CH_3 complexes (**1**, **2** and **2lut-Me**), which correlates with an increased Lewis acidity of Ni in the enolate complexes, as determined from computational studies. This behavior has an impact on catalytic performance by stabilizing the chelate and contributing to making the subsequent insertion rate limiting. Addressing the impact of the supporting phosphine phenoxide, large donors were shown to have a higher binding affinity to complex **1-CCO** than **2-CCO**, likely due to the rigid steric-profile proximal to the phenoxide in **2-CCO**.

Complex **2P** provides a rare example of precatalyst that produces both cis and trans isomers in solution. $^{31}P\{^1H\}$ NMR EXSY experiments reveal an intramolecular mechanism of exchange between the cis and trans isomers and rule out involvement of free PEt_3. This mechanism is consistent with the mechanism of isomerization in ethylene/acrylate copolymerization found by computation.

Lastly, both **2-CCO** and **2lut-Me** serve as a competent single-component catalyst in ethylene/acrylate copolymerization. Analysis of their copolymerization behavior indicates that employing weak ancillary ligand L leads to both higher insertion rate and lower thermal stability, both of which should be taken into account in catalyst design.

References

(1) Chen, C. *Nature Reviews Chemistry* **2018**, *2*, 6–14.

(2) Nakamura, A.; Ito, S.; Nozaki, K. *Chem. Rev.* **2009**, *109*, 5215–5244.

(3) Carrow, B. P.; Nozaki, K. *Macromolecules* **2014**, *47*, 2541–2555.

(4) Chen, E. Y.-X. *Chem. Rev.* **2009**, *109*, 5157–5214.

(5) Luckham, S. L. J.; Nozaki, K. *Acc. Chem. Res.* **2021**, *54*, 344–355.

(6) Baur, M.; Lin, F.; Morgen, T. O.; Odenwald, L.; Mecking, S. *Science* **2021**, *374*, 604–607.

(7) Guan, Z.; Cotts, P. M.; McCord, E. F.; McLain, S. J. *Science* **1999**, *283*, 2059–2062.

(8) Arriola, D. J.; Carnahan, E. M.; Hustad, P. D.; Kuhlman, R. L.; Wenzel, T. T. *Science* **2006**, *312*, 714–719.

(9) Makio, H.; Terao, H.; Iwashita, A.; Fujita, T. *Chem. Rev.* **2011**, *111*, 2363–2449.

(10) Weng, W.; Shen, Z.; Jordan, R. F. *J. Am. Chem. Soc.* **2007**, *129*, 15450–15451.

(11) Guironnet, D.; Roesle, P.; Rünzi, T.; Göttker-Schnetmann, I.; Mecking, S. *J. Am. Chem. Soc.* **2009**, *131*, 422–423.

(12) Johnson, L. K.; Mecking, S.; Brookhart, M. *J. Am. Chem. Soc.* **1996**, *118*, 267–268.

(13) Drent, E.; Dijk, R. v.; Ginkel, R. v.; Oort, B. v.; Pugh, R. I. *Chem. Commun.* **2002**, 744–745.

(14) Nakamura, A.; Anselment, T. M. J.; Claverie, J.; Goodall, B.; Jordan, R. F.; Mecking, S.; Rieger, B.; Sen, A.; van Leeuwen, P. W. N. M.; Nozaki, K. *Acc. Chem. Res.* **2013**, *46*, 1438–1449.

(15) Tao, W.-j.; Nakano, R.; Ito, S.; Nozaki, K. *Angewandte Chemie* **2016**, *128*, 2885–2889.

(16) Tao, W.; Akita, S.; Nakano, R.; Ito, S.; Hoshimoto, Y.; Ogoshi, S.; Nozaki, K. *Chem. Commun.* **2017**, *53*, 2630–2633.

(17) Carrow, B. P.; Nozaki, K. *J. Am. Chem. Soc.* **2012**, *134*, 8802–8805.

(18) Dai, S.; Chen, C. *Angewandte Chemie* **2016**, *128*, 13475–13479.

(19) Long, B. K.; Eagan, J. M.; Mulzer, M.; Coates, G. W. *Angewandte Chemie International Edition* **2016**, *55*, 7106–7110.

(20) Xin, B. S.; Sato, N.; Tanna, A.; Oishi, Y.; Konishi, Y.; Shimizu, F. *J. Am. Chem. Soc.* **2017**, *139*, 3611–3614.

(21) Zhang, Y.; Mu, H.; Pan, L.; Wang, X.; Li, Y. *ACS Catal.* **2018**, *8*, 5963–5976.

(22) Chen, M.; Chen, C. *ACS Catal.* **2017**, *7*, 1308–1312.

(23) Tan, C.; Chen, C. *Angewandte Chemie* **2019**, *131*, 7268–7276.

(24) Xiong, S.; Shoshani, M. M.; Zhang, X.; Spinney, H. A.; Nett, A. J.; Henderson, B. S.; Miller, T. F.; Agapie, T. *J. Am. Chem. Soc.* **2021**, *143*, 6516–6527.

(25) Wang, X.-l.; Zhang, Y.-p.; Wang, F.; Pan, L.; Wang, B.; Li, Y.-s. *ACS Catal.* **2021**, *11*, 2902–2911.

(26) Berkefeld, A.; Drexler, M.; Möller, H. M.; Mecking, S. *J. Am. Chem. Soc.* **2009**, *131*, 12613–12622.

(27) Allen, K. E.; Campos, J.; Daugulis, O.; Brookhart, M. *ACS Catal.* **2015**, *5*, 456–464.

(28) Williams, B. S.; Leatherman, M. D.; White, P. S.; Brookhart, M. *J. Am. Chem. Soc.* **2005**, *127*, 5132–5146.

(29) Chen, C.; Luo, S.; Jordan, R. F. *J. Am. Chem. Soc.* **2010**, *132*, 5273–5284.

(30) Chen, Z.; Liu, W.; Daugulis, O.; Brookhart, M. *J. Am. Chem. Soc.* **2016**, *138*, 16120–16129.

(31) Chen, Z.; Leatherman, M. D.; Daugulis, O.; Brookhart, M. *J. Am. Chem. Soc.* **2017**, *139*, 16013–16022.

(32) Guo, L.; Dai, S.; Sui, X.; Chen, C. *ACS Catal.* **2016**, *6*, 428–441.

(33) Dai, S.; Sui, X.; Chen, C. *Angewandte Chemie International Edition* **2015**, *54*, 9948–9953.

(34) Berkefeld, A.; Mecking, S. *J. Am. Chem. Soc.* **2009**, *131*, 1565–1574.

(35) Jenkins, J. C.; Brookhart, M. *J. Am. Chem. Soc.* **2004**, *126*, 5827–5842.

(36) Mecking, S.; Johnson, L. K.; Wang, L.; Brookhart, M. *Journal of the American Chemical Society* **1998**, *120*, 888–899.

(37) Rix, F. C.; Brookhart, M.; White, P. S. *J. Am. Chem. Soc.* **1996**, *118*, 4746–4764.

(38) Chandran, D.; Lee, K. M.; Chang, H. C.; Song, G. Y.; Lee, J.-E.; Suh, H.; Kim, I. *Journal of Organometallic Chemistry* **2012**, *718*, 8–13.

(39) C. Chapleski, R.; L. Kern, J.; Curtis Anderson, W.; K. Long, B.; Roy, S. *Catalysis Science & Technology* **2020**, *10*, 2029–2039.

(40) Svejda, S. A.; Johnson, L. K.; Brookhart, M. *J. Am. Chem. Soc.* **1999**, *121*, 10634–10635.

(41) Leatherman, M. D.; Svejda, S. A.; Johnson, L. K.; Brookhart, M. *J. Am. Chem. Soc.* **2003**, *125*, 3068–3081.

(42) Kenyon, P.; Falivene, L.; Caporaso, L.; Mecking, S. *ACS Catal.* **2019**, *9*, 11552–11556.

(43) Thompson, M. E.; Baxter, S. M.; Bulls, A. R.; Burger, B. J.; Nolan, M. C.; Santarsiero, B. D.; Schaefer, W. P.; Bercaw, J. E. *J. Am. Chem. Soc.* **1987**, *109*, 203–219.

(44) Noda, S.; Nakamura, A.; Kochi, T.; Chung, L. W.; Morokuma, K.; Nozaki, K. *J. Am. Chem. Soc.* **2009**, *131*, 14088–14100.

(45) Zhou, X.; Yu, D.; Rong, C.; Lu, T.; Liu, S. *Chemical Physics Letters* **2017**, *684*, 97–102.

(46) Casares, J. A.; Espinet, P. *Inorg. Chem.* **1997**, *36*, 5428–5431.

(47) Macchioni, A.; Bellachioma, G.; Cardaci, G.; Travaglia, M.; Zuccaccia, C.; Milani, B.; Corso, G.; Zangrando, E.; Mestroni, G.; Carfagna, C.; Formica, M. *Organometallics* **1999**, *18*, 3061–3069.

(48) Redfield, D. A.; Nelson, J. H.; Henry, R. A.; Moore, D. W.; Jonassen, H. B. *J. Am. Chem. Soc.* **1974**, *96*, 6298–6309.

(49) Casado, A. L.; Casares, J. A.; Espinet, P. *Inorg. Chem.* **1998**, *37*, 4154–4156.

(50) Romeo, R.; D'Amico, G.; Sicilia, E.; Russo, N.; Rizzato, S. *J. Am. Chem. Soc.* **2007**, *129*, 5744–5755.

(51) Bircher, H.; Bender, B. R.; von Philipsborn, W. *Magnetic Resonance in Chemistry* **1993**, *31*, 293–298.

(52) Londaitsbehere, A.; Herrera, M.; Salgado, A.; Mosquera, M. E. G.; Cuenca, T.; Cano, J. *Organometallics* **2017**, *36*, 3904–3911.